# Secondary Air Interaction with Main Flow in Axial Turbines

by

Metodi B. Zlatinov

B.S.E. Mechanical and Aerospace Engineering
Princeton University (2009)

Submitted to the Department of Aeronautics and Astronautics
in partial fulfillment of the requirements for the degree of

Master of Science in Aeronautics and Astronautics

at the

MASSACHUSETTS INSTITUTE OF TECHNOLOGY

June 2011



Author .....
Department of Aeronautics and Astronautics
May 19, 2011

Certified by .....
Choon S. Tan
Senior Research Engineer of Aeronautics and Astronautics
Thesis Supervisor

Accepted by .....
Eytan H. Modiano
Associate Professor of Aeronautics and Astronautics
Chair, Graduate Program Committee

**Secondary Air Interaction with Main Flow in Axial Turbines**

by

Metodi B. Zlatinov

Submitted to the Department of Aeronautics and Astronautics
on May 19, 2011, in partial fulfillment of the
requirements for the degree of
Master of Science in Aeronautics and Astronautics

## Abstract

Secondary air, known as purge air, is injected through seals in the hub and shroud of axial turbines to prevent hot gas ingestion into the endwall cavities. An investigation into the interaction of purge flow with turbine main flow has been undertaken, to determine where losses are generated, how they are generated, and what are the most effective ways for reducing them. The effect of purge flow design on the system's susceptibility to ingestion was also studied. Tools developed for accomplishing these objectives include: a consistent framework for isolating entropy generated due to viscous effects, a procedure for factoring out individual loss categories, and a linear model for secondary air flow response to the main flow pressure field. These tools, applied to steady computations, elucidate four routes through which change in loss generation is brought about by purge air injection: a shear layer between purge and main streams, modification of the secondary flow through the blade passage, an increase in degree of reaction, and the potential for reducing tip clearance flow (for the case of purge flow injected from the shroud). It was further determined that purge air mass flow and swirl velocity are effective parameters for mitigating loss, with a potential for 70% reduction in purge flow losses. By contrast, purge slot axial inclination and gap width do not affect the loss characteristics of purge flow by more than 6%. The benefit of pre-swirling purge flow can be negated by decreased sealing effectiveness, if ingestion is driven by the pressure non-uniformity associated with the rotor upstream influence. However for a representative vane-rotor stage, in which the vane-induced circumferential pressure non-uniformity dominates in the intra vane-rotor gap, pre-swirling purge flow can be beneficial to deterring hot gas ingestion. Finally a framework has been formulated for assessing the time-averaged impact of unsteady vane-rotor interaction on purge flow-induced loss generation. Preliminary results suggest that flow unsteadiness can result in substantially higher losses associated with purge flow injection.

Thesis Supervisor: Choon S. Tan
Title: Senior Research Engineer of Aeronautics and Astronautics

# Acknowledgments

The work presented in this thesis took shape over the course of two exciting years, and through the synergistic efforts of a myriad of people. Here, I would like to express my gratitude to those colleagues, teachers, friends, and family who have also taught me much that cannot be included in the following chapters.

Let me begin by thanking my research adviser, Dr. Choon Tan. His tactful guidance has helped me overcome the numerous challenges that inevitably threaten to discourage a graduate student at every turn. Every time I have walked across the hall, in a mild state of panic, to convince him that the latest impasse is a definitive one, he has cheerfully suggested otherwise. And though I was often incredulous, with admirable patience, he has let me go off and convince myself in my own way. His vote of confidence has given me the opportunity to explore ideas, take responsibility for my work, and internalize knowledge that would have otherwise simply brushed me by.

I am indebted to many colleagues at Siemens Energy, starting with Dr. Matt Montgomery and Dr. Tito Islam, who coordinated the collaboration between MIT and Siemens. Dr. Montgomery's experience in the field, and his remarkable ability to paraphrase a not-so-eloquent graduate student's words into something coherent, have been invaluable assets to our team. I am very grateful to Dr. Barry Brown, who designed the turbine stage for this project, and to Melissa Harris, who got the project off the ground. The computational results Melissa provided me with put me months ahead in my work. Manoj Singh was also a wonderful help, taking over from Melissa and providing many additional results. I thank Dr. Dave Little and Dr. Dave Canon for participating in many discussions, providing valuable insight into industry practices. In addition, Dr. Little's thought-provoking comments always challenged me to be thorough in my work. Dr. Todd Ebert has also been extremely kind and willing to help, going out of his way to provide me with detailed replies to numerous question. And of course, I am thankful to Siemens CKI, an MITEI Sustaining Member, for funding this work, as well as Eni S.p.A., for supporting me

with a generous fellowship for the first nine months at MIT.

A very special thanks goes out to Professor Nick Cumpsty, for the illuminating discussions that helped guide our research. I was always impressed by the insightful comments he would give, after being briefed on half a year's worth of progress in a mere one hour. My fellow lab-mates have also been a great support and source of knowledge, especially Jeff Defoe, who helped me get CFX up and running on our computer cluster.

Lastly, and most importantly, I thank my family - my sister, who's example I have followed since I was old enough to know right from wrong; my mother, who has guided and encouraged me with a patient, devoted, and invisible hand; and my caring and kind wife-to-be, Ashley, who brings balance and harmony to my days.

# Contents

# List of Figures

# List of Tables

# List of Symbols

## Dimensional Quantities

| | |
|---|---|
| $A$ | Dynamic amplification factor |
| $\mathcal{A}$ | Area |
| $c_x$ | Axial chord |
| $c$ | Damping coefficient |
| $d_g$ | Purge gap width |
| $F$ | Force |
| $f$ | Frequency |
| $h$ | Specific enthalpy |
| $k_{eff}$ | Effective thermal conductivity |
| $k$ | Spring constant |
| $\lambda$ | Blade pitch |
| $\dot{m}$ | Mass flow rate |
| $\mu_{eff}$ | Effective viscosity |
| $\Omega$ | Angular speed of rotating component |
| $\omega$ | Angular frequency |
| $P$ | Pressure |
| $q_{in}$ | Heat transfer per unit area into control volume |
| $r_{hub}$ | Hub radius |
| $s$ | Specific entropy |

$\dot{S}'''_{gen}$ Entropy generation rate per unit volume

$T$ Temperature

$\tau_{ij}$ Shear stress tensor

$U$ Disk rim speed, $U = \Omega r_{hub}$

$V$ Velocity in stationary frame

$\mathcal{V}$ Volume

$W$ Velocity in rotating frame

$w$ Specific work

$x$ Axial direction (except in chapter 7, where it refers to the meridional direction)

## Subscripts and Superscripts

$aa$ Area-averaged quantity

$a, b$ Primary and secondary streams

$in$ Inlet plane

$LE$ Rotor leading edge

$ma$ Mass-averaged quantity

$R$ Rotor blade

$s, c, r$ Streamwise, cross-flow and radial directions

$TE$ Rotor trailing edge

$ta$ Time-averaged quantity

$tot$ Sum of all streams

$t1, t2$ Stagnation quantity at inflow and outflow

$t2s$ Stagnation quantity after ideal expansion

$therm$ Due to thermal mixing

$V$ Nozzle guide vane

$visc$ Due to viscous effects

| | |
|---|---|
| $wa$ | Work-averaged quantity |
| $x, \theta, r$ | Axial, circumferential and radial directions |

## Non-Dimensional Quantities

| | |
|---|---|
| $AR$ | Aspect Ratio |
| $\eta$ | Efficiency |
| $gf$ | Gap fraction, $\frac{d_g}{(r_{tip}-r_{hub})}$ |
| $\Lambda$ | degree of reaction, $\frac{\Delta h_{rotor}}{\Delta h_{stage}}$ |
| $mf$ | Mass fraction, $\frac{\dot{m}_b}{\dot{m}_a}$ |
| $M$ | Mach number |
| $\pi$ | Stage pressure ratio |
| $\Psi$ | Stage Loading, $\frac{\Delta h_t}{(\Omega r_{midspan})^2}$ |
| $\Phi$ | Flow Coefficient, $\frac{V_x}{\Omega r_{midspan}}$ |
| $\phi$ | Injection angle (except in chapter 7, where it refers to phase angle) |
| $sf$ | Swirl fraction, $\frac{V_{\theta,b}}{\Omega r_{hub}}$ |
| $\sigma$ | Solidity, (chord length/pitch) |
| $\xi$ | Damping ratio |

# Chapter 1

# Introduction

In the past decade, industrial gas turbines have by far become the most popular type of plant for power generation, due to their compactness, low emissions and potential for power-heat cogeneration. In the effort to increase energy conversion efficiency, engineers have raised turbine inlet temperatures to well above the melting point of advance alloys. Turbine blades are generally protected by expensive thermal barrier coatings and various forms of internal and film cooling. However, in order to prevent hot gases from being ingested into the unprotected cavities outside the design flowpath[1], cool air bled from the compressor is used to purge the gaps at the endwalls, as illustrated in Fig. 1-1.

These secondary air streams, referred to as sealing flows or purge flows, interact with the mainstream flow to generate losses. As materials limitations make it increasingly difficult to improve gas turbine performance by further raising turbine inlet temperature and compressor pressure ratio, designers have turned their attention to cooling and purge flow losses. While it has been demonstrated that certain injection schemes can lead to a reduction in purge flow-related losses, the flow processes that underlie the observed improvements are not well understood. The overall goal of this research is to delineate the various loss mechanisms associated with purge flow injection and trace them back to the specific purge flow characteristics.

[1]Hot gases can gain access to such cavities through clearances between rotating and stationary components, as well as through gaps in the endwalls that are used for platform cooling

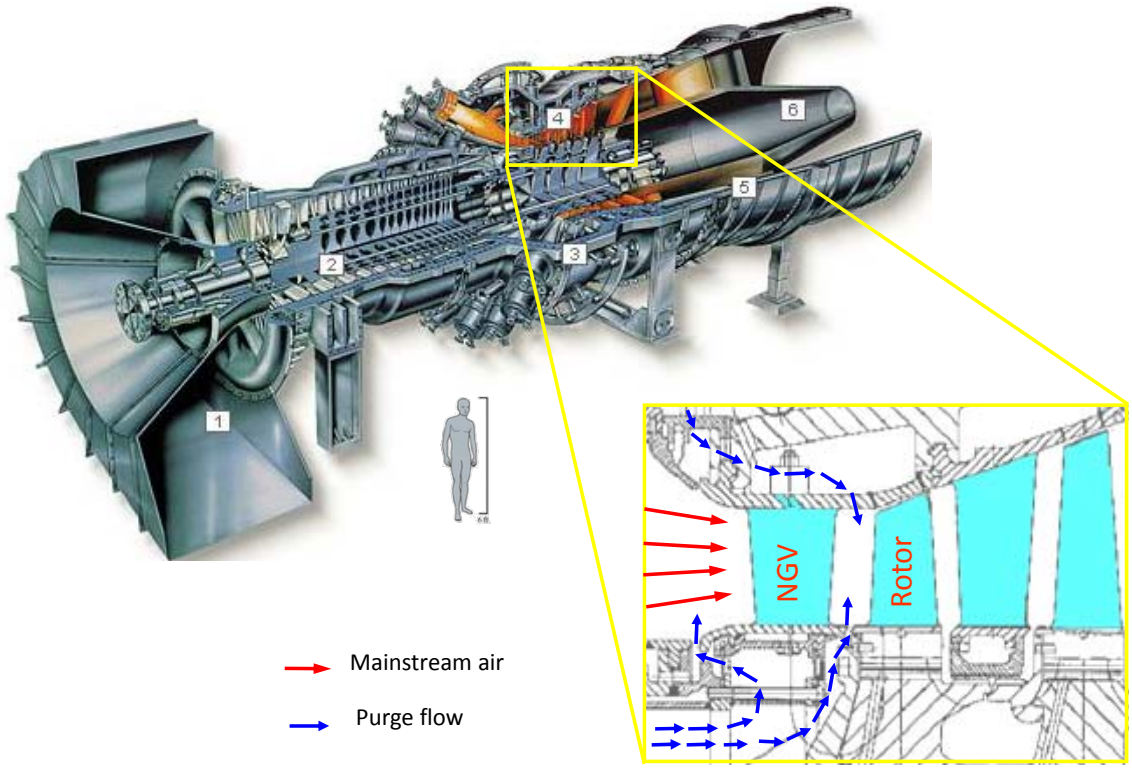


Figure 1-1: SCHEMATIC OF MAINSTREAM AND PURGE FLOWS IN THE FIRST STAGE AN AXIAL TURBINE

## 1.1 Literature Review

The existing literature on this subject has been helpful in guiding the research leading to the results in this work. Pau et. al. [2] found that injecting purge flow leads to an increase in efficiency, mainly due to the modification of the shock system downstream of the stator. However, most studies show efficiency penalties associated with purge flow injection. Kost and Nicklas [3] noted the potential for increasing the horseshoe vortex if the purge slot traverses the saddle point. Reid et. al. [1] conducted measurements and calculations, suggesting two loss mechanisms associated with purge flow interacting with the mainstream flow: one due to the mixing of the sealant flow with the mainstream flow and the other due to the change in the flow through a downstream blade row. However these two mechanisms were not rigorously isolated and quantified in terms of purge flow parameters. Ong et. al. [4] uses an analytical mixing model to isolate the loss due to mixing of the purge and mainstream flows,

and links the additional losses to a change in flow angles. More recently, Popovic and Hodson [5] have identified three regimes for loss depending on purge mass flow rate and sealing effectiveness. Some new vortical structures have been observed [6] to emerge from a purge slot on a linear cascade, and have been suggested as a cause of enhanced losses. In terms of design improvements, a number of publications [1][7][5] have pointed to the potential for reducing losses through swirling of purge flow prior to injection. McLean et. al. [8] studied three types of injection configurations, and actually observed an increase in efficiency from one of them.

Clearly, a substantial amount of research has been done on secondary air losses. However, a lack of clarity in the causal relationship between these losses and their drivers still prevents a systematic approach to the design of purge flow injection systems.

## 1.2 Objectives of Present Work

The ultimate goal of this work is to provide the fundamental understanding necessary to improve turbine performance, through intentional design of the purge flow system. To achieve this goal, the following specific objectives were pursued:

1. Identify where and how additional losses are generated due to purge flow injection
2. Quantify these losses in terms of purge flow design parameters
3. Establish scaling rules and propose design guidelines based on the acquired knowledge
4. Identify if and how the proposed design modifications affect the susceptibility of the system to ingest mainstream gases, and reevaluate design guidelines

Computational tools were used, in conjunction with various post-processing techniques for establishing traceability of purge flow losses to responsible flow features. Analytical models were formulated when necessary. For the present, experimental validation relies on the published literature.

## 1.3 Contributions and Findings

The key findings of this work include new insight into mechanisms for loss generation and ingestion, as well as clear guidelines for design improvement. These are summarized below:

1. For purge flow injected at the hub, every 1% purge flow increases stage losses by roughly 8%. This penatly is associated with three effects: a shear layer between purge and mainstream flows (which accounts for 1/2 of the penalty), interaction of purge flow with secondary flows through the blade passage, and increased tip-clearance flow and blade wetted losses due to an increased degree of reaction.

2. Purge flow injected from the shroud upstream of an unshrouded rotor introduces the beneficial effect of tip-clearance flow suppression. Consequently, shroud-injected purge flow does not result in significant losses.

3. Aside from the change in reaction, all of the above effects are driven by circumferential (swirl) velocity mismatch between purge and mainstream flows. Swirling purge flow prior to injection can potentially reduce losses of hub-injected purge flow by 2/3. Swirling shroud-injected purge flow does not result in significant additional benefit, as there is a tradeoff between purge flow losses and tip clearance flow suppression.

4. Gap width and injection angle are not effective design parameters for mitigating loss. Their combined effect can reduce purge flow losses by 5-6% only.

5. In the presence of a circumferential pressure non-uniformity associated with the rotor upstream influence, pre-swirling purge flow has the effect of reducing sealing effectiveness. The increased requirement for purge flow essentially offsets the benefit of pre-swirling. However, a linear analysis of the phenomenon demonstrates that, if it is the stationary vane that dominates the pressure non-uniformity in the NGV-rotor gap, pre-swirling of purge flow is beneficial both with regard to loss and ingestion.

6. Preliminary results indicated that flow unsteadiness has a significant impact on the losses associated with purge-mainstream flow interaction.

Aspects of the approach and tools used to accomplish the research objectives also constitute original contributions. In particular, multiple levels of modeling were used to systematically delineate between different loss mechanisms. A way for isolating viscous losses was developed, using appropriate averaging of flow quantities. Volumetric entropy generation rate was used, in conjunction with a rigorous definition of secondary flow, to relate loss generation to responsible flow features. To the author's knowledge, the linear analysis, developed for identifying the conditions under which ingestion is likely to occur, is also new. Finally, a framework has been formulated for loss accounting in unsteady, non-uniform flow situations.

## 1.4 Organization

The chapters in this thesis are organized as follows: First, the framework of research approach is presented, providing a high level overview of how the research objectives will be addressed. A separate chapter is then devoted to defining loss in the context of turbomachinery, and its relation to entropy. Some challenges in using entropy as a measure of loss are also addressed. Chapters 4 - 7 contain the key results. Losses in the baseline case with no purge flow are presented first. The effects of purge flow injection on stage losses are treated in two chapters: the first identifying the various effects, and the second quantifying these to arrive at practical design guidelines. Chapter 7 reevaluates these guidelines, considering the issue of purge flow sealing effectiveness and ingestion susceptibility. Chapter 8 develops loss accounting procedures for unsteady flow and presents some preliminary unsteady results. All findings are summarized in the Conclusion, and future work in the areas of unsteady computations and experimental assessment are suggested.

# Chapter 2

# Research Approach

In order to establish causality between flow features related to purge flow and their effect on loss, it was necessary to develop a systematic research approach. The key features of this approach include: multiple levels of modeling, systematic variation of a range of design parameters, use of both computational and analytical tools, and entropy as a measure of loss. This chapter will devote a section to each of these features, describing the details and the utility of each.

## 2.1 Multiple Levels of Modeling

To allow for a systematic delineation of the loss mechanisms associated with purge flow injection, three models of purge flow interacting with mainstream flow are conceived. The first model, illustrated in Fig. 2-1(a), consists of purge flow injection into a simple axisymmetric throughflow (an abstraction of a turbine in the form of an annular duct with no blades). The second model, depicted in Fig. 2-1(b), consists of a full three dimensional blade passage, with a mixing plane interface between nozzle guide vane (NGV) and rotor domains. This model adds the additional complexity of circumferential non-uniformity due to the presence of rotor blades, but does not include unsteady NGV-rotor interaction due to the mixing plane downstream of the NGV. The final model does away with the mixing plane approximation, allowing for unsteady effects to be investigated for their time-averaged impact on turbine perfor-

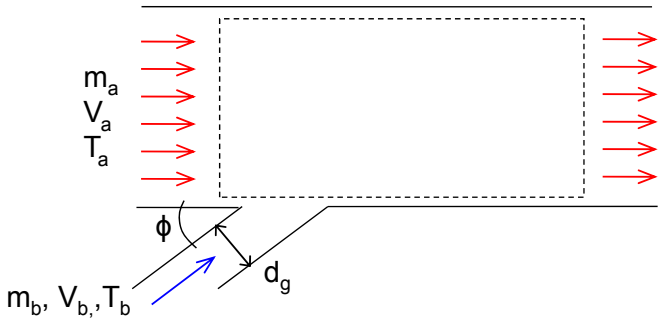


(a) Axisymmetric model

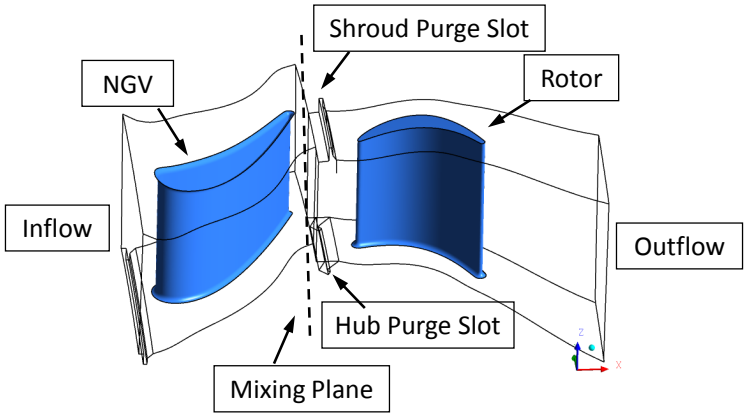


(b) Three dimensional blade passage with mixing plane

Figure 2-1: AXISYMMETRIC AND THREE DIMENSIONAL MODELS

mance. The characteristics of the representative first stage high pressure unshrouded turbine used for this investigation are listed in Table 2.1.

Comparing the axisymmetric model to the steady three dimensional model allows for loss mechanisms present in the former to be factored out, revealing additional loss mechanisms present in the latter. Unsteady effects can also be isolated by comparing steady and unsteady models. This thesis will focus on the first two models (axisymmetric and steady three dimensional). Chapter 8 develops post processing techniques for unsteady flow and presents some preliminary unsteady results, paving the way for future work in that direction.

Table 2.1: CHARACTERISTICS OF A REPRESENTATIVE TURBINE STAGE

| Quantity | Value | Quantity | Value |
|---|---|---|---|
| $\Omega$ | 2749 [rad/s] | U | 300 [m/s] |
| $AR_R$ | 1.11 | $\pi$ | 0.546 |
| $M_{R,in}$ | 0.785 | $\Lambda$ | 0.412 |
| $\Psi$ | 2.17 | $\Phi$ | 0.65 |
| $T_b/T_a$ | 0.6 | $\sigma_R$ | 1.37 |

## 2.2 Purge Flow Design Parameters

Four purge flow parameters were investigated for their effect on loss in both axisymmetric and three dimensional models. These parameters are: the purge air mass flow rate ($\dot{m}_b$), circumferential (swirl) velocity of purge flow prior to injection ($V_{\theta,b}$), purge flow injection angle ($\phi$) and purge gap width ($d_g$). The last two parameters are geometric in nature, and are best defined by Fig. 2-2, which shows the meridional views of two purge slot geometries: one with $\phi = 30°$ and one with $\phi = 90°$

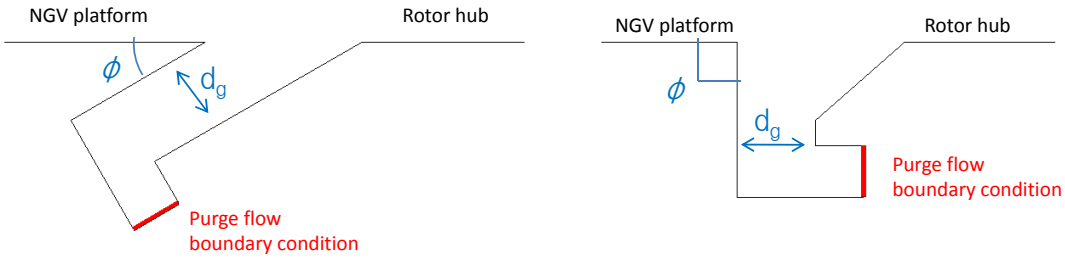


(a) gf=5%, 30° (b) gf=5%, 90°

Figure 2-2: PURGE SLOT GEOMETRIES

Two additional features of the purge slot geometries in Fig. 2-2 are an "elbow" near the purge flow inlet boundary and a chamfer for the case of $\phi = 90°$. The elbow is put in place to prevent numerical difficulties associated with fluid being expelled from what is specified computationally as an inlet boundary condition. This difficulty arises from the "disk-pumping" effect in rotor-stator systems - the natural tendency for fluid to be "pumped" up the rotating wall and down the stationary wall[9]. The

45° chamfer in Fig. 2-2(b) is added to all purge slot geometries with $\phi > 45°$ in order to minimize separation bubbles at sharp corners.

In order to generalize the results in this thesis, the four purge flow parameters were cast in non-dimensional terms, corresponding to purge flow mass fraction ($mf$), swirl fraction of the rim speed ($sf$), injection angle ($\phi$) and gap fraction of the annulus height ($gf$). The definitions of these non-dimensional parameters are summarized in Table 2.2, along with the range of values studied, and the physical purge flow characteristics these parameters control (scope). The design space for which this investigation was performed was chosen to be a superset of parameter values found in industry.

Table 2.2: DEFINITION OF PURGE FLOW DESIGN PARAMETERS

| Parameter | Definition | Range | Scope |
|---|---|---|---|
| $mf$ | $\frac{\dot{m}_b}{\dot{m}_a}$ | $0\% - 1.5\%$ | x-momentum<br>r-momentum<br>$\theta$-momentum<br>kinetic energy |
| $sf$ | $\frac{V_{\theta,b}}{\Omega r_{hub}}$ | $0\% - 100\%$ | $\theta$-momentum<br>kinetic energy |
| $\phi$ | see Fig. 2-2 | $30° - 90°$ | x-momentum<br>r-momentum |
| $gf$ | $\frac{d_g}{(r_{tip} - r_{hub})}$ | $5\% - 8.3\%$ | x-momentum<br>r-momentum<br>kinetic energy |

## 2.3 Computational and Analytical Tools

The main computational tool for investigation was the Ansys 12.0 CFX RANS solver. The three dimensional blade passage was modeled with structured grids generated with the default topology of Numeca's Autogird - O4H, which is illustrated in Fig. 2-3(a). Grid-convergence studies showed that increasing the number of nodes used for

modeling the three dimensional blade passage from 0.93 to 2.2 million results in only 3% change in the total losses and less than 1% change in net purge flow effects. Most of the results presented are from the finer mesh, while the coarse mesh was used for more expedient parametric studies. In all computations the $k-\omega$ Shear Stress Transport turbulence model was used with wall functions ($y+ \approx 12$). A typical turbulence intensity of 10% was imposed at the NGV inlet boundary and 5% at the purge slot inlet boundary[1]. Representative stagnation pressure and temperature profiles were used at the NGV inlet boundary. It was found that using different specific heats for mainstream and purge flow does not have a significant impact on the results, so combustion gas properties were used for all streams ($\gamma = c_p/c_v = 1.3027$).

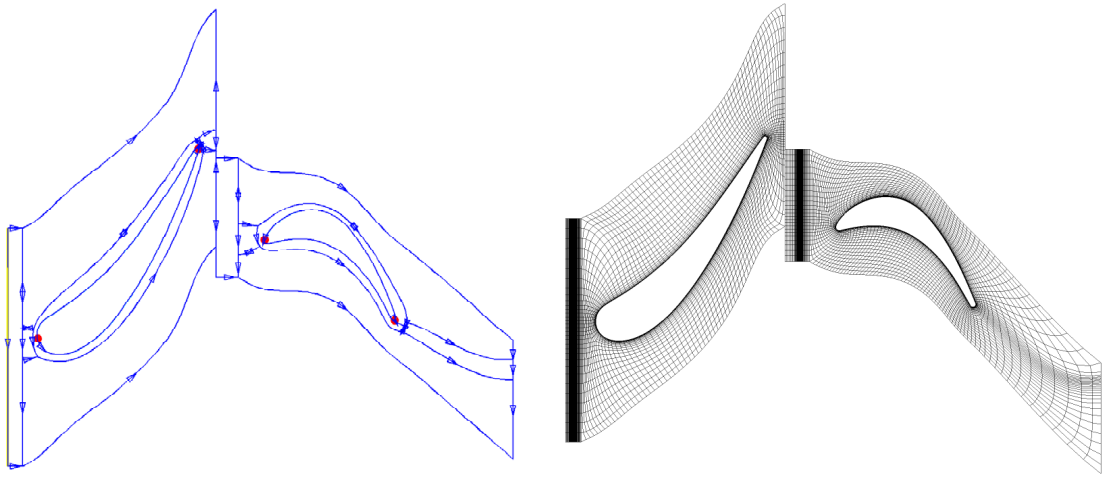

(a) Blade-to-blade view of O4H Topology (b) 0.9M node mesh at 50% span

Figure 2-3: MESH TOPOLOGY

The computational model of the axisymmetric configuration in Fig. 2-1(a) used a grid resolution comparable to the finer three dimensional grid. The annulus height of the axisymmetric domain is set to the annulus height at the inlet of the rotor. The inlet boundary condition is based on the computed flow downstream of the NGV mixing plane, and the hub walls downstream of the purge slot are rotating, as in the three dimensional case.

The axisymmetric configuration also lends itself to a control volume mixed-out

[1]These are reasonable values, based on the reccomendation of Dr. Tito Islam of Siemens Energy

analysis, based on that outlined by Young and Wilcock[10]. The mixed-out analysis yields an explicit expression (which will be presented in detail in chapter 5) for the total loss of mechanical power incurred upon complete mixing of two streams at constant area. The expression gives a direct measure of how purge flow loss scales in the axisymmetric configuration. Furthermore, the quantities in this expression can be expressed in terms of the non-dimensional purge flow parameters under investigation, allowing for a expedient parametric study of their effects.

## 2.4 Using Entropy as a Measure of Loss

In much of the literature, turbine losses are quantified in terms of stagnation pressure loss, non-dimensionalized according to various conventions [11]. This practice comes from viewing turbine blade rows as nozzles (in the relative frame, the rotor can also be viewed as a row of nozzles), with the purpose of accelerating working fluid with a minimal drop in stagnation pressure (relative stagnation pressure in the case of the rotor). This view of turbine blade rows allows for loss characteristics to be studied experimentally through cascade tests, where stagnation pressure measurements are readily obtainable.

However, viewing a turbine as a components in a powerplant, with the ultimate purpose of extracting mechanical work, it can be shown that the lost opportunity to extract work is fundamentally a function of the entropy generated due to irreversible processes. It will also be shown in this section that the quantity 'entropy generation rate per unit volume' can be a powerful tool for tracing loss generation to responsible flow features. These advantages motivate the use of entropy, over the more conventional loss coefficients based on stagnation pressure drop, as the consistent measure of lost work. The remainder of this chapter will present the relationship of entropy generation to lost work, and the concept of volumetric entropy generation rate.

### 2.4.1 Entropy generation and lost work

Let us first briefly review the relationship between entropy generation and lost work for a general thermodynamic process, before applying the concepts to the situation of a turbine expansion.

The first and second laws of thermodynamics are given for a differential process by Eqn (2.1) and Eqn (2.2).

$$\delta w = \delta q - dh \tag{2.1}$$

$$ds = \frac{\delta q}{T} + ds_{irrev} \tag{2.2}$$

Combining the two to eliminate the heat transfer term yields an expression for the work extracted for a reversible ($ds_{irrev} = 0$) and non-reversible process, given by Eqn. (2.3) and Eqn. (2.4) respectively.

$$\delta w_{rev} = -dh + Tds \tag{2.3}$$

$$\delta w = -dh + Tds - Tds_{irrev} \tag{2.4}$$

The difference between the two processes gives the lost opportunity to do work, which is given by Eqn. (2.5). Therefore, entropy generation due to irreversible processes is a measure of lost opportunity to do work.

$$\delta w_{loss} = \delta w_{rev} - \delta w = Tds_{irrev} \tag{2.5}$$

For an expansion through a turbine, one can go through the process outlined in Fig. 2-4 to derive an effective temperature at which entropy is generated, $\widetilde{T}_{t2}$. This temperature is an average of $T_{t2}$ and $T_{t2s}$[2].

### 2.4.2 Volumetric entropy generation rate

As mentioned earlier, another advantage of using entropy as a measure of loss is the ability to compute and visualize the quantity 'entropy generation rate per unit volume'. To clarify the meaning and utility of this concept, consider a differential

[2]In practice, $T_{t2}$ can be used instead of $\widetilde{T}_{t2}$, as these two temperatures usually differ by fractions of a percent

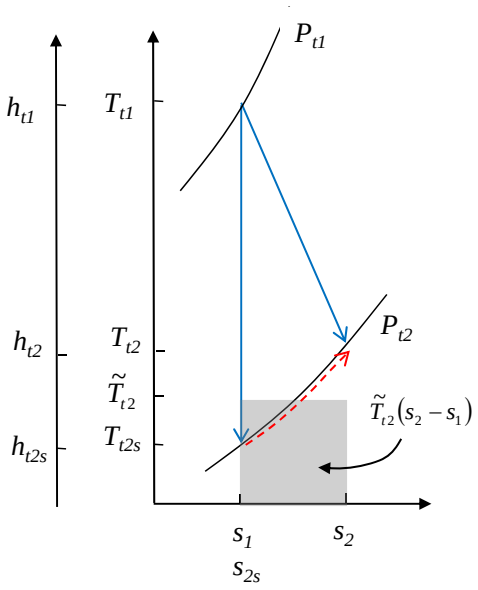


$$
\begin{aligned}
w_{loss} &= \left(h_{t1} - h_{t2s}\right) - \left(h_{t1} - h_{t2}\right) \\
&= h_{t2} - h_{t2s} \\
&= \int_{2s}^{2} dh_t \\
&= \int_{2s}^{2} T_t ds - \cancel{v dP_t}^{\,0} \\
&= \widetilde{T}_{t2}\left(s_2 - s_1\right)
\end{aligned}
$$

Figure 2-4: LOST WORK IN TURBINE EXPANSION.

control volume, such as a finite volume in a computational domain. For steady flow, the entropy inside this differential control volume can change due to convection, reversible heat transfer, and generation of entropy due to irreversible processes. We can therefore formulate a steady state conservation equation for entropy, consisting of convection, diffusion and source terms, as per Eqn. (2.6)

$$\iint_{\mathcal{A}} s\rho\vec{V} \cdot d\vec{\mathcal{A}} - \iint_{\mathcal{A}} \frac{q_{in}}{T} d\mathcal{A} = \iiint_{\mathcal{V}} \dot{S}'''_{gen} d\mathcal{V} \tag{2.6}$$

The volumetric source term on the right-hand-side of Eqn. (2.6), $\dot{S}'''_{gen}$, is the quantity 'entropy generation rate per unit volume', with units of $W/Km^2$. Insight into the spatial distribution of entropy sources can be gained from contour plots of $\dot{S}'''_{gen}$. As an example, Fig. 2-5 shows such contours on a number of axial cuts through the rotor[3], clearly indicating the high losses associated with tip clearance flow.

Here the concepts of volumetric entropy generation rate is only introduced as one of the tools for tracing entropy generation to the flow features responsible. The next

[3] $\dot{S}'''_{gen}$ is non-dimensionalized by multiplying with the reference temperature defined in Fig. 2-4 and the through flow time-scale, $\frac{c_x}{V_x}$, (giving lost work per unit volume) then dividing by axial dynamic head at the rotor inlet (energy per unit volume). Velocity and density are taken at the inlet to the rotor, for consistency between the three dimensional and axisymmetric cases

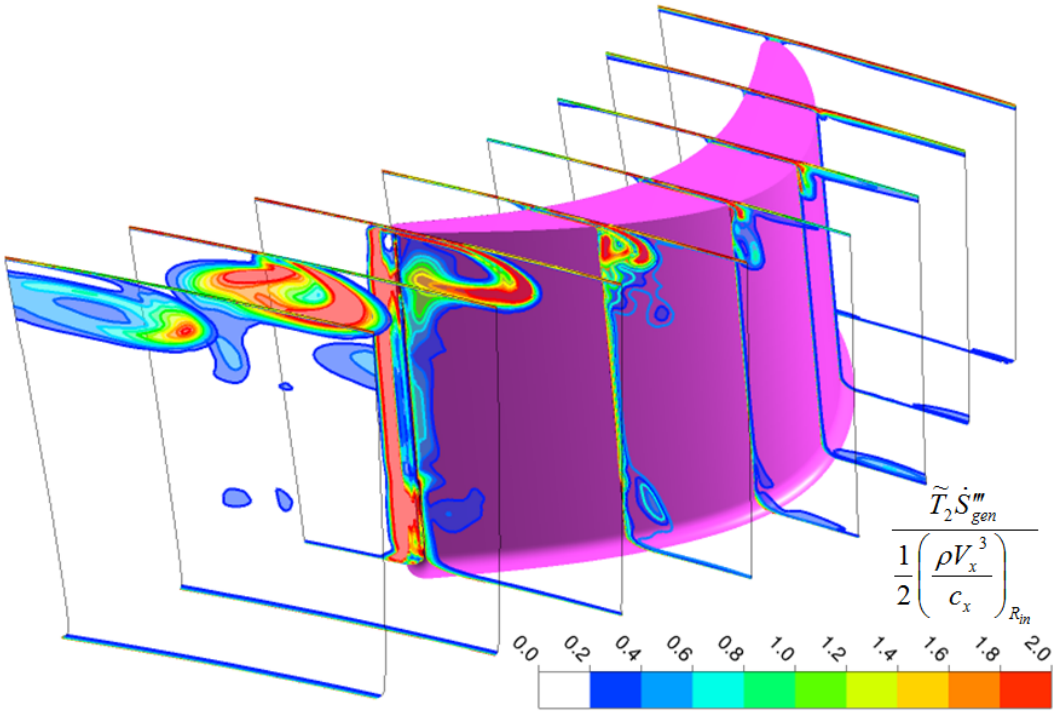


Figure 2-5: ENTROPY GENERATION RATE PER UNIT VOLUME AT AXIAL PLANES THROUGH ROTOR

chapter will provide a more in-depth discussion on various ways of calculating $\dot{S}'''_{gen}$, both directly and indirectly.

## 2.5 Summary of Research Approach

In summary, the key features of the research approach consist of

1. The purge flow injection process is modeled on three levels: as a secondary air stream injected into mainstream flow in (i) an axisymmetric duct, (ii) a three dimensional NGV-rotor passage, rendered steady through the use of a mixing plane, and (iii) a three dimensional NGV-rotor passage without a mixing plane. Each of these adds new effects to the picture, as the full complexity of a realistic turbine flow is approached. Note that the main conclusions of this thesis will be based on the first two configurations (axisymmetric and steady three dimensional), leaving a detailed assessment of unsteady effects for future work.

2. Four purge flow parameters are studied for their impact on loss. These are $mf$, $sf$, $\phi$ and $gf$.

3. The three dimensional blade passage is modeled computationally. The axisymmetric model is studied both computationally and analytically using a control volume mixed-out analysis.

4. Entropy is used as a measure of lost opportunity to do work. The main motivation for this is consistency with the interpretation of volumetric entropy generation rate as a loss source that is directly traceable to local flow features.

The next chapter will discuss the use of entropy in more detail.

# Chapter 3

# Loss Accounting with Entropy

In chapter 2 the argument was made for using entropy as a measure of loss. The motivation for this was two-fold: first, the function of a turbine as a power-generating device makes it useful to quantify losses in terms of the lost opportunity to do work; second, the concept of volumetric entropy generation rate allows for loss sources to be traced back to flow features. However, there are a number of important considerations that need to be clarified in order to ensure that this entropy-based approach is interpreted appropriately. This chapter will first illustrate the conceptual distinction and the necessity to delineate between viscous losses and losses due to irreversible mixing of hot and cold stream. A practical methodology for delineating between these two losses will then be developed. Finally, the numerical challenges associated with evaluating volumetric entropy generation rate from the computed flow field will be addressed.

## 3.1 Viscous Losses vs. Thermal Mixing Losses

Entropy is a measure of the lost opportunity to do work from a system perspective - it can easily be related to a percentage-point drop in cycle efficiency through an availability analysis. However, when assessing the performance of a specific component, such as a turbine, not all of the potential for work that is foregone within the spacial domain of that component is an indication of component deficiency. In particular, it

will be shown that only entropy generated due to viscous effects constitutes a debit in turbine performance. A novel approach for isolating these viscous effects from the total entropy generated will also be formulated.

### 3.1.1 Conceptual delineation of viscous and thermal mixing losses

Consider first the scenario of multiple streams (let us say two, for simplicity) of working fluid, with distinct inlet conditions, being expanded through an ideal turbine. In addition, let us constrain the expansion process, such that all streams are in isolation from one another, and are expanded to the same downstream stagnation pressure, $P_{t2}$. Such an expansion process is shown in Fig. 3-1 as the process $1 \rightarrow 2s$.

For steady, ideal flow, the downstream stagnation temperature of each stream can be calculated by Eqn. (3.1).

$$T_{t2si} = T_{t1i} \left( \frac{P_{t2}}{P_{t1i}} \right)^{\frac{\gamma-1}{\gamma}} \tag{3.1}$$

The expansion work extracted by the turbine is given by Eqn. (3.2).

$$w_{expand} = \sum_i \frac{\dot{m}_i}{m_{tot}} c_p \left( T_{t1i} - T_{t2si} \right) \tag{3.2}$$

After the expansion process, assuming the two streams are in mechanical equilibrium, the difference in stagnation temperatures would reflect a disparity in static temperature. The two streams can be brought to thermal equilibrium reversibly using a heat engine, such as a thermoelectric device, or a combination of compressors, heat exchangers and turbines, as discussed in [12]. This is shown in Fig. 3-1 as the process $2s \rightarrow 2s'$. The additional work output from this hypothetical heat engine is given by Eqn. (3.4), in which the temperature $T_{t2s'}$ is obtained by enforcing constant entropy flux.

$$T_{t2s'} = \prod_j \left( T_{t1j} \pi_j^{\frac{\gamma-1}{\gamma}} \right)^{\frac{\dot{m}_i}{\dot{m}_{tot}}} \tag{3.3}$$

$$w_{heat\ engine} = \sum_i \frac{\dot{m}_i}{m_{tot}} \left( T_{t2si} - T_{t2s'} \right) \tag{3.4}$$

The sum $w_{expand} + w_{heat\ engine}$ constitutes the total potential for work by the system. However, in a non-ideal expansion process, viscous effects will dissipate mechanical energy. This will be reflected as entropy generation $\Delta s_{visc}$ and a loss in expansion work given by Eqn. (3.5) (During the expansion process the two streams

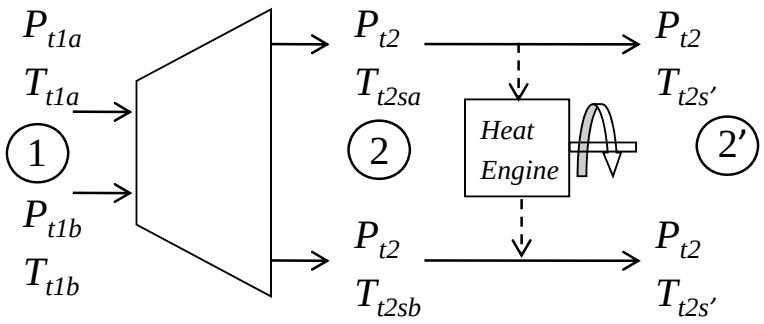


(a) Schmatic

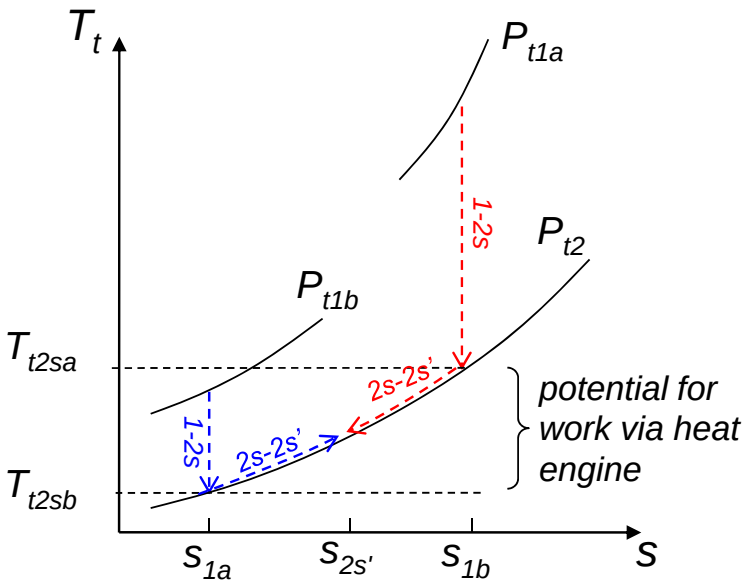


(b) T-s diagram

Figure 3-1: CONCEPTUAL EXPANSION PROCESS OF TWO STREAMS

were still in thermal isolation, so all of the entropy generated is due to viscous effects.)

$$\begin{aligned} w_{visc\ loss} &= \sum_i \frac{\dot{m}_i}{m_{tot}} c_p \left(T_{t2i} - T_{t2si}\right) \\ &= \widetilde{T}_{t2} \Delta s_{visc} \end{aligned} \tag{3.5}$$

In reality, there is no opportunity to insert a heat engine to extract additional work through the process $2s \rightarrow 2s'$. Therefore, all of the potential heat engine work is also a loss, this time due to irreversible thermal mixing rather than viscous effects.

$$w_{therm\ mix\ loss} = w_{heat\ engine} = \widetilde{T}_{t2} \Delta s_{therm} \tag{3.6}$$

The total entropy generated in a turbine expansion process therefore reflects the total lost opportunity to do work, due to both viscous and thermal mixing effects. To give the reader a sense of the relative magnitudes of these two loss categories - expansion of a single stream through a NGV-Rotor stage results primarily in viscous losses, with only 1.8% of the lost work being due to thermal mixing of the non-uniform inlet temperture. However, when purge flow with a temperature ratio of $T_b/T_a = 0.6$ is injected, the additional losses incurred due to thermal mixing are comperable to the additinal losses due to viscous effects. Thermal mixing losses can only be reduced by reducing the temperature difference between purge and mainstream flows, but that is usually not an option, since purge flow temperatrue is set by the location in the compressor from which the purge air is bled. Therefore, when purge flow injection is tailored to minimize viscous losses, thermal mixing losses dominate.

However it would not be meaningful to penalize the turbine design for failing to to do a heat engine's work. In the context of turbine performance, the ideal potential work should only include expansion work, $w_{expand}$. This leads to a turbine loss given by Eqn. (3.5) only, which reflects that only viscous losses leading to a stagnation pressure drop are relevant to turbine performance. Lost work due to thermal mixing is still a loss to the overall gas turbine cycle, but should be dealt with as a separate loss category. Moreover, the exact impact of thermal mixing is not defined unless

a full cycle analysis is conducted, as a number of authors have shown [13][14] that some of this thermal mixing loss will be compensated by a reduced exhaust loss. The remainder of this thesis will therefore focus only on viscous losses.

### 3.1.2 Practical delineation of viscous and thermal mixing losses

The previous section illustrated the significance of delineating between entropy generation due to viscous effects and that due to thermal mixing. However, unless the downstream state is uniform (fully mixed out), application of Eqn. (3.5) and Eqn. (3.6) requires tracking each individual fluid particle. Since we are interested in tracing the development of entropy generation, we need a practical way of dealing with non-uniform conditions at intermediate locations through the turbine stage. This section presents a practical method for delineating between viscous and thermal mixing losses, through the use of appropriate averaging of non-uniform flow.

Consider again the simple scenario of two streams of working fluid, with distinct inlet conditions, being expanded through a turbine to the same downstream stagnation pressure. One way of dealing with such an expansion is by tracing each individual fluid stream as it expands through the turbine, but a much more practical approach is illustrated in Fig. 3-2.

The first step is to replace the non-uniform inlet flow with an equivalent uniform flow that would produce the same work output if expanded through a turbine to an arbitrary downstream pressure, $P_{t2}$. To obtain an appropriate average stagnation pressure, which to assign to the substitute uniform flow, we refer to the conceptual process illustrated in Fig. 3-2. The higher pressure stream can be expanded isentropically to a pressure $P_{t1}^{wa}$ such that the work output from this process is just enough to compress the lower pressure stream to the same $P_{t1}^{wa}$. This process generates no net work, and is no more than an interpretation of the useful concept of "work-averaging" developed by Cumpsty and Horlock[15]. The expression for work-averaged pressure,

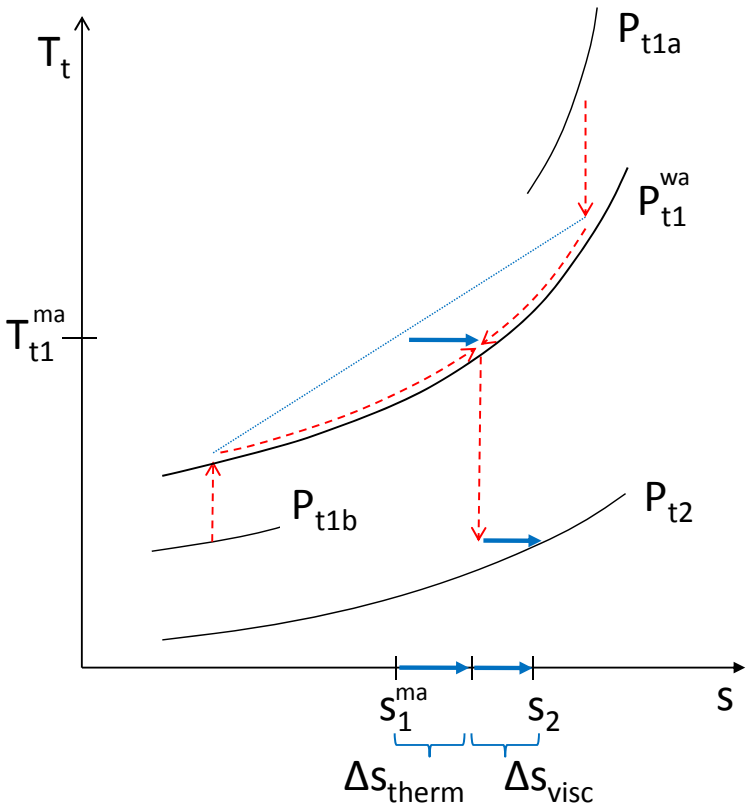


Figure 3-2: T-S DIAGRAM OF MULTI-STREAM EXPANSION ILLUSTRATING THE CONCEPT OF WORK-AVERAGED PRESSURE.

derived in [15], is therefore reproduced here in Eqn. (3.7)

$$P_t^{wa} = \left[ \frac{\int T_t d\dot{m}}{\int T_t / P_t^{\frac{\gamma-1}{\gamma}} d\dot{m}} \right]^{\frac{\gamma}{\gamma-1}} \tag{3.7}$$

Returning to the simple example of two discrete streams, mass-averaging of stagnation temperature allows us to fix the state of the substitute uniform flow, while enforcing energy conservation. (As discussed in [15], stagnation temperature is mass-averaged, because it is proportional to the convected quantity of stagnation enthalpy.) Note that mass-averaging of stagnation temperature amounts to thermal mixing at constant pressure. This process is irreversible and generates an amount of entropy $\Delta s_{therm}$, as indicated in Fig. 3-2. Therefore, by virtue of using mass-averaged stagnation temperature, one implicitly factors out the potential heat engine work. Expanding this hypothetical uniform flow, with inlet conditions $P_{t1}^{wa}$ and $T_{t1}^{ma}$, to any

downstream pressure, will yield the same work output as if the two original streams were expanded independently to that same downstream pressure. The ideal expansion work of these two streams is therefore readily given by Eqn. (3.8).

$$w_{expand} = c_p T_{t1}^{ma} \left[ 1 - \left( \frac{P_{t2}^{wa}}{P_{t1}^{wa}} \right)^{\frac{\gamma-1}{\gamma}} \right] \tag{3.8}$$

In an expansion process through a non-ideal turbine, entropy will be generated due to viscous effects ($\Delta s_{visc}$), with an attendant lost opportunity to do work given by Eqn. (3.9).

$$\begin{aligned} w_{visc\ loss} &= \widetilde{T}_{t2} \Delta s_{visc} = \widetilde{T}_{t2} \left( \Delta s - \Delta s_{therm} \right) = w_{expand} - w_{actual} \\ &= c_p \left[ T_{t2}^{ma} - T_{t1}^{ma} \left( \frac{P_{t2}^{wa}}{P_{t1}^{wa}} \right)^{\frac{\gamma-1}{\gamma}} \right] \end{aligned} \tag{3.9}$$

The thermal mixing loss can also be calculated by Eqn. (3.10), though it is of little practical value to a turbine designer.

$$w_{therm\ mix\ loss} = \widetilde{T}_{t2} \Delta s_{therm} = \widetilde{T}_{t2} \Delta s - w_{visc\ loss} \tag{3.10}$$

The method described above provides a rigorous way to accounting for viscous losses in turbomachinery, under steady flow conditions. To the author's knowledge, this is the first application of the averaging procedures developed by Cumpsty and Horlock [15] for this purpose.

The application of this method to unsteady flow situations entails additional modifications. However, since the current focus is on steady flow situations, this constraint does not affect the results that will be presented. Future work will likely require an assessment of unsteady effects, therefore Chapter 8 will return to the subject of loss accounting, with guidelines and considerations concerning loss accounting for unsteady flow.

## 3.2 Utility and Challenges of Volumetric Entropy Generation Rate

In the previous chapter, the notion of an entropy source term, $\dot{S}'''_{gen}$, was introduced. It can be shown [16] that this volumetric source term can be expressed as the sum of two components, which are given by equations (3.11) and (3.12) respectively

$$\dot{S}'''_{visc} = \frac{1}{T}\tau_{ij}\frac{\partial V_i}{\partial x_j} \tag{3.11}$$

$$\dot{S}'''_{therm} = \frac{k_{eff}}{T^2}\left(\frac{\partial T}{\partial x_j}\right)^2 \tag{3.12}$$

$\dot{S}'''_{visc}$ is the entropy generation rate per unit volume due to viscous effects, and $\dot{S}'''_{therm}$ is the entropy generation rate per unit volume due to thermal mixing. Contours of $\dot{S}'''_{visc}$ provide a useful tool for establishing traceability between turbine losses and flow features. Contours of $\dot{S}'''_{therm}$ indicate regions of thermal mixing, where the opportunity for doing work with a heat engine is being lost.

In theory, one could also integrate either $\dot{S}'''_{visc}$ or $\dot{S}'''_{therm}$ over the computational domain and directly delineate between viscous and thermal mixing losses, without having to resort to the method discussed in section 3.1.2 of this chapter. However, as will be shown in the following sections, there are numerical challenges associated with obtaining these entropy source terms. Therefore, given the computational resources available, volumetric entropy generation rate is confined to the status of a qualitative tool; any quantitative conclusions are based on Eqn. (3.9) and Eqn. (3.10).

### 3.2.1 Challenges in direct evaluation of $\dot{S}'''_{gen}$

Direct numerical evaluation of entropy generation rate via Eqn. (3.11) and Eqn. (3.12) is challenging due to the quadratic dependence on velocity and temperature gradients. To demonstrate this, we can compare two ways of computing the change in entropy between two axial cuts in the blade row shown in Fig. 3-3(a). In one instance, Eqn. (3.13) is used to calculate the difference in entropy flux through an outlet plane,

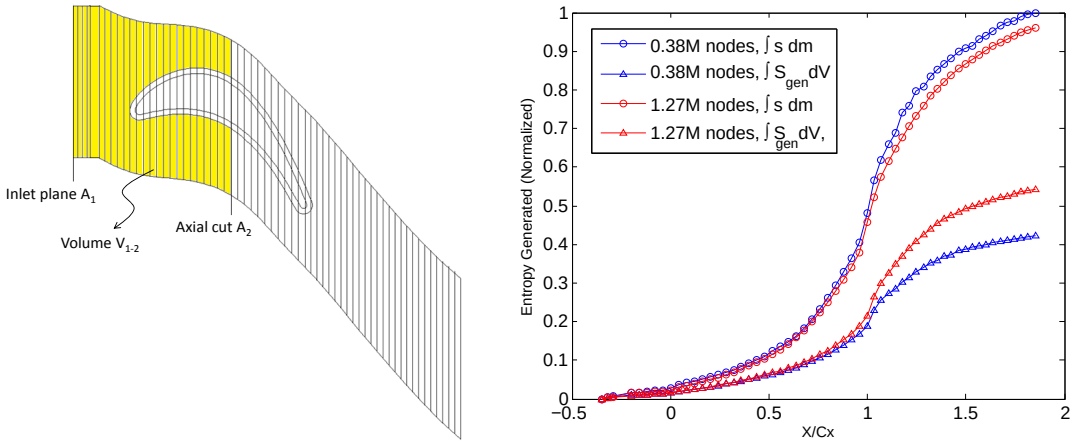


(a) Integration domains for computing accumulated entropy up to a given axial cut

(b) Accumulated entropy through rotor

Figure 3-3: ACCUMULATED ENTROPY THROUGH ROTOR WITH LOW AND HIGH GRID RESOLUTION, BASED ON ENTROPY FLUX THROUGH AXIAL CUTS AND VOLUME INTEGRAL OF $\dot{S}'''_{gen}$

$A_2$, and inlet plane, $A_1$.

$$\Delta s = \frac{1}{\dot{m}} \iint_{\mathcal{A}_1} \rho s \vec{V} \cdot d\vec{\mathcal{A}} - \iint_{\mathcal{A}_2} \rho s \vec{V} \cdot d\vec{\mathcal{A}} \tag{3.13}$$

Alternatively, integrating $\dot{S}'''_{gen}$ over the volume between those two planes, as in Eqn. (3.14), should give an equivalent result.

$$\Delta s = \frac{1}{\dot{m}} \iiint_{\mathcal{V}_{1-2}} \dot{S}'''_{gen} d\mathcal{V} \tag{3.14}$$

The accumulation of generated entropy through a rotor blade passage, as calculated using these two methods, is presented in Fig. 3-3(b) for grids of 0.38 and 1.27 million nodes respectively (0.93 million and 2.2 million nodes for full stage including NGV and purge cavities). The abscissa shows axial distance from the leading edge of the blade, and is normalized by the blade axial chord (such that the blade spans from 0 to 1). The ordinate is normalized by the highest entropy generated up to the outflow plane of the computational domain.

Tripling the number of nodes used for modeling the rotor passage has little effect on

the result obtained using the first method ( 3% change), indicating grid convergence. On the other hand, integrating $\dot{S}'''_{gen}$ estimates a change in enrtopy 58% lower for the coarse grid and 44% lower for the fine grid. It will be demonstrated in the next chapter that these discrepancies occur preciesly where there are high velocity gradients and relatively poor grid resolution. Further grid refinement studies on the axisymmetric configuration (Fig. 2-1(a)) demonstrated that the volume integral of $\dot{S}'''_{gen}$ does indeed converge to the physically correct value of dissipation, but only for extremely high grid densities that are unpractical in three dimensions (particularly due to the secondary flows and wakes that introduce regions of high gradients away from the relatively well resolved endwall region).

Nevertheless, though the volume integral of entropy generation rate underestimates losses, the axial distribution of accumulated loss, as calculated by the two methods, is in agreement. Therefore, the author has used contours of volumetric entropy generation rate, as calculated by Eqn. (3.11), as a qualitative tool for identifying local regions of high loss. Any quantitative conclusions are based on lost work obtained with Eqn. (3.9)

### 3.2.2 Challenges in indirect evaluation of $\dot{S}'''_{gen}$

An effort was made to obtain numerically accurate $\dot{S}'''_{gen}$ through application of Eqn. (2.6) locally on every individual finite volume, and backing out the volumetric source term using Eqn. (3.15).

$$\dot{S}'''_{gen\ indirect} = \frac{\iint_{\mathcal{A}} \rho s \vec{V} \cdot d\vec{\mathcal{A}} - \iint_{\mathcal{A}} \frac{q_{in}}{T} d\mathcal{A}}{\iiint_{\mathcal{V}} dV} \tag{3.15}$$

The motivation for doing this is to avoid the quadratic dependence on velocity and temperature gradients, thereby arriving at a better estimate of the entropy generation rate. However, as will be shown in the following text, this approach is plagued by a different kind of numerical challenge, and therefore could not achieve its purpose; for this reason, more details on the implementation of this indirect approach are relegated to Appendix A. Results will be presented here primarily as a consistency

check to Eqn. (3.11) and Eqn. (3.12), as well as to provide a stepping stone for further development of this approach in the future.

To illustrate that the method is implemented correctly, we can use the axisymmetric configuration shown in Fig. 3-4(a) with a very high mesh resolution (0.41

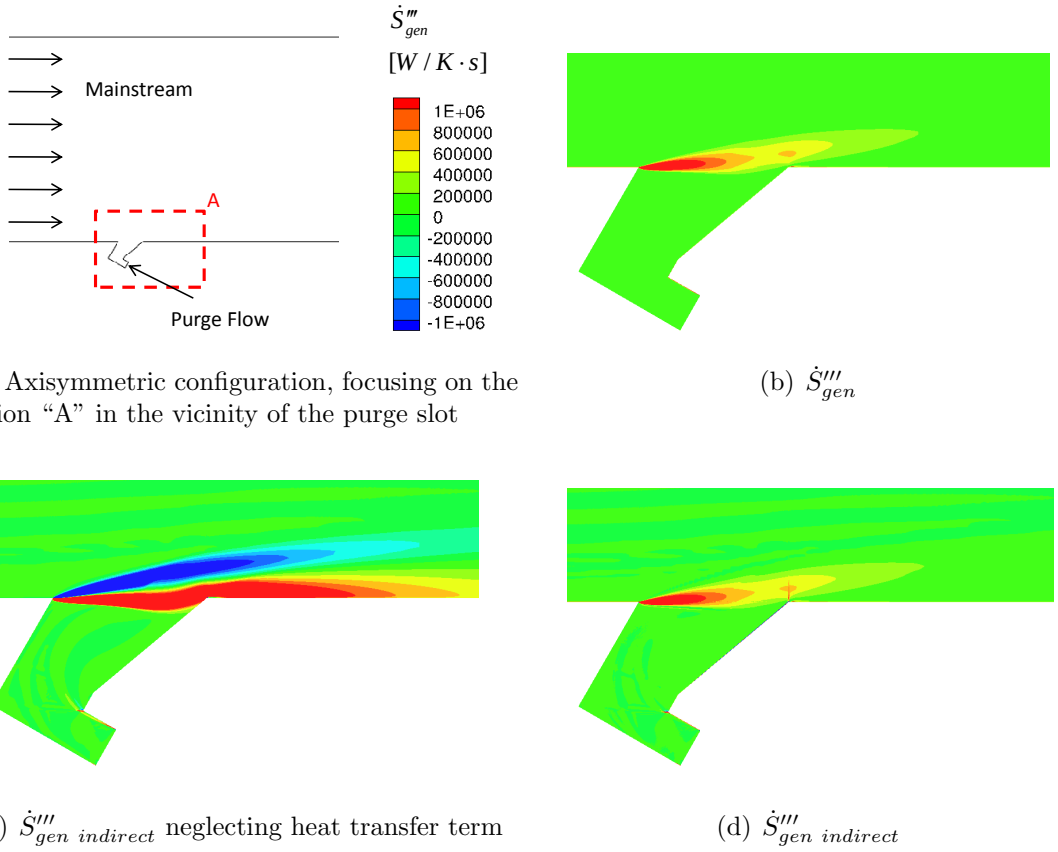


(a) Axisymmetric configuration, focusing on the region "A" in the vicinity of the purge slot

(b) $\dot{S}'''_{gen}$

(c) $\dot{S}'''_{gen\ indirect}$ neglecting heat transfer term

(d) $\dot{S}'''_{gen\ indirect}$

Figure 3-4: CONTOURS OF $\dot{S}'''_{gen}$ AND $\dot{S}'''_{gen\ indirect}$ NEAR PURGE SLOT OF AXISYMMETRIC MODEL

million nodes and y+≈0.8). Because the mesh is so fine, velocity and temperature gradients are computed accurately and Eqn. (3.11) and Eqn. (3.12) do not underestimate the entropy generated. Zooming into the region around the purge slot, (marked "A" in Fig. 3-4(a)) we can plot contours of $\dot{S}'''_{gen}$ that show entropy generated due to viscous shearing and thermal mixing at the interface between purge and mainstream flows (Fig. 3-4(b)). If we then use Eqn. (3.15) to calculate $\dot{S}'''_{gen\ indirect}$ but neglect the reversible heat transfer term, $\iint_{\mathcal{A}} \frac{q_{in}}{T} d\mathcal{A}$, we get the distinctly different contours in Fig. 3-4(c). However these contours make sense - they simply imply that the change

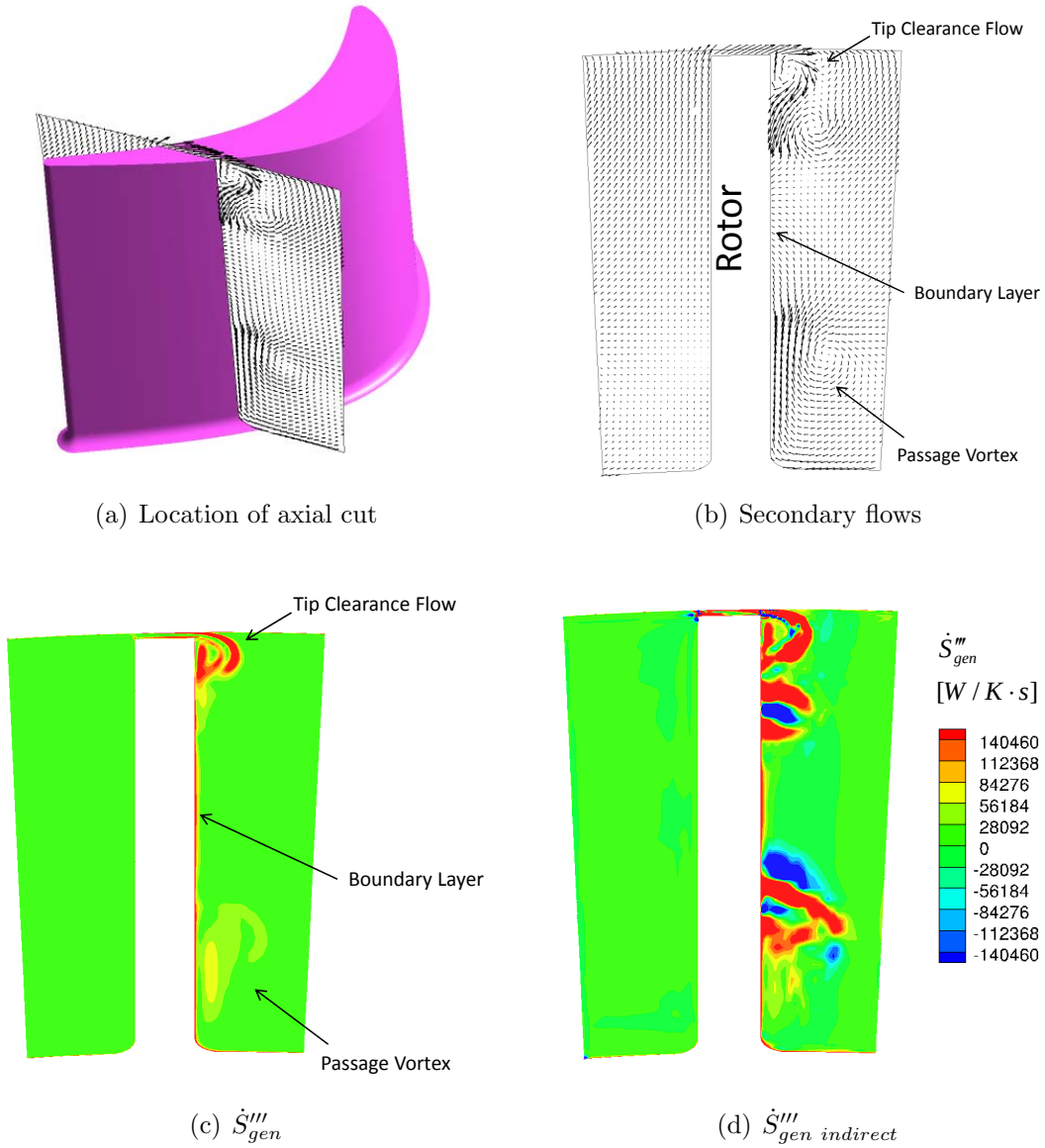


(a) Location of axial cut

(b) Secondary flows

(c) $\dot{S}'''_{gen}$

(d) $\dot{S}'''_{gen\ indirect}$

Figure 3-5: CONTOURS OF $\dot{S}'''_{gen}$ AND $\dot{S}'''_{gen\ indirect}$ IN REGIONS OF SECONDARY FLOW ON AN AXIAL CUT AT 80% AXIAL CHORD OF THE ROTOR

in entropy of the fluid elements in that region is dominated by reversible heat transfer. The entropy of purge flow near the hub is increasing as it is being heated by the substantially hotter mainstream flow, and cooling effect of purge flow on the mainstream is reflected in the negative change in entropy of the latter. If all the terms in Eqn. (3.15) are used, the expected contours for entropy generation rate are recovered in Fig. 3-4(d). Furthermore, volume integrals of $\dot{S}'''_{gen\ indirect}$ and $\dot{S}'''_{gen}$ give the same result.

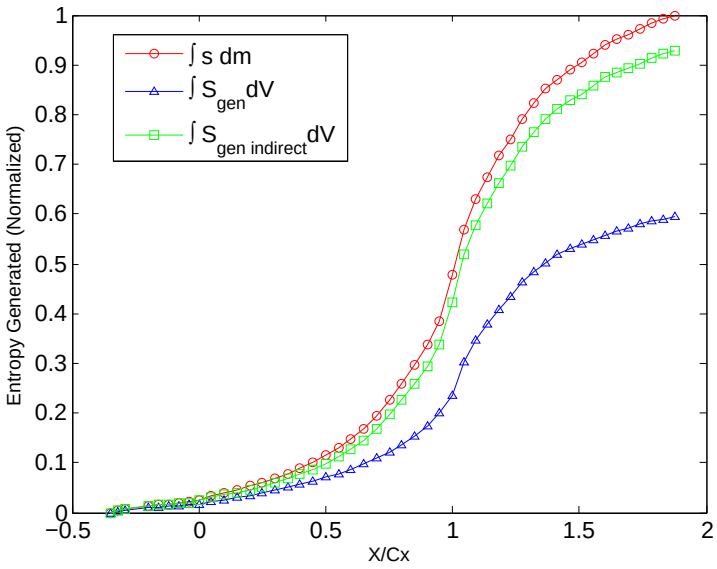


Figure 3-6: ACCUMULATED ENTROPY THROUGH THE ROTOR WITH HIGH GRID RESOLUTION, BASED ON ENTROPY FLUX THROUGH AXIAL CUTS, VOLUME INTEGRAL OF $\dot{S}'''_{gen}$ AND VOLUME INTEGRAL OF $\dot{S}'''_{gen\ indirect}$

However, if we apply Eqn. (3.15) to the fluid elements on a slice at 80% axial chord of the three dimensional rotor (Fig. 3-5(a)), where there are substantial secondary flows and velocity gradients away from the well resolved boundary layer region (Fig. 3-5(b)), the results are no longer satisfactory. Figure 3-5(c) shows contours of $\dot{S}'''_{gen}$, indicating high entropy-generating regions associated with tip clearance flow, hub passage vortex and blade surface boundary layer. We expect $\dot{S}'''_{gen\ indirect}$ to identify the same regions of high entropy generation rate, though with an increased intensity (recall that $\dot{S}'''_{gen}$ underestimated entropy generated by 44%, while $\dot{S}'''_{gen\ indirect}$ should give an accurate result). Figure 3-5(d) shows $\dot{S}'''_{gen\ indirect}$ on the same axial cut. It is evident that although there is a resemblance between the two contour plots, $\dot{S}'''_{gen\ indirect}$ suggests there are regions of negative entropy generation rate. This would defy the Second Law of Thermodynamics and is clearly not physical. However, as Fig. 3-6 shows, if $\dot{S}'''_{gen\ indirect}$ is integrated throughout the rotor passage, it not only estimates the correct axial distribution of entropy sources, but also comes very close the converged result from Eqn. (3.13). This leads us to conclude that the finite volumes with net negative entropy generation rate are balanced by adjacent volumes

with excessive entropy generation rate. Therefore, despite this local inconsistencies, the entropy generated on a global scale is adequately estimated. It is postulated that the cause of the local inconsistency is that the CFX finite volume code conserves mass, energy and momentum, but not necessarily entropy. Further investigation on this subject is desirable, in order to confirm this conjecture and find a possible solution.

## 3.3 Summary of Loss Accounting with Entropy

There are two key conclusions resulting from the discussion on loss accounting with entropy. Firstly, only entropy generated due to viscous effects ought to be considered a loss for the turbine. Thermal mixing between purge and mainstream flows generates a significant amount of entropy that must be factored out in the loss accounting process, and considered only during cycle analysis. A practical method for doing this is developed based on the concept of work-averaged pressure. Secondly, although volumetric entropy generation rate can directly be separated into viscous and thermal contributions, a quadratic dependence on temperature and velocity gradients requires significantly higher grid resolution to achieve quantitative convergence for these quantities. An indirect method for evaluating local entropy generation rate, based on net flux of entropy through finite volumes, appears to suffer from a different kind of numerical challenge - entropy is a derived variable that is not conserved locally. However, direct evaluation of entropy generation rate (from velocity and temperature gradients) correctly captures qualitative trends, making $\dot{S}'''_{visc}$ in particular a useful tool for identifying loss sources.

# Chapter 4

# Baseline Losses

Having established a consistent framework for interpreting loss, key findings, addressing where and how losses are generated, will be presented. In this chapter, the losses in the baseline case without purge flow will be presented, in order to provide a context for the additional loss mechanisms associated with purge flow injection, which are the subject of the following chapters.

## 4.1 Loss Distribution for Baseline Turbine Stage

The accumulation of viscous loss as a function of axial distance through the blade passage is shown in Fig. 4-1. Viscous lost work (ordinate) is normalized by the total loss up to the outflow plane, which is 0.85 axial chord lengths downstream of the rotor trailing edge. The axial distance from the leading edge of the rotor (abscissa) is normalized by the rotor axial chord, such that the rotor spans from 0 to 1. There is a discrete jump in loss that marks the location of the mixing plane.

It is clear that the larger proportion of loss is generated in the rotor. To gain further insight into why that is so, and why the accumulated loss curve looks the way it does, we can break down the total loss into four basic categories - profile loss, endwall wetted loss, tip clearance flow loss and secondary flow loss. The final breakdown at the outflow plane is presented in the bar chart of Fig. 4-1. The procedure for delineating the various loss categories will be presented in the following section.

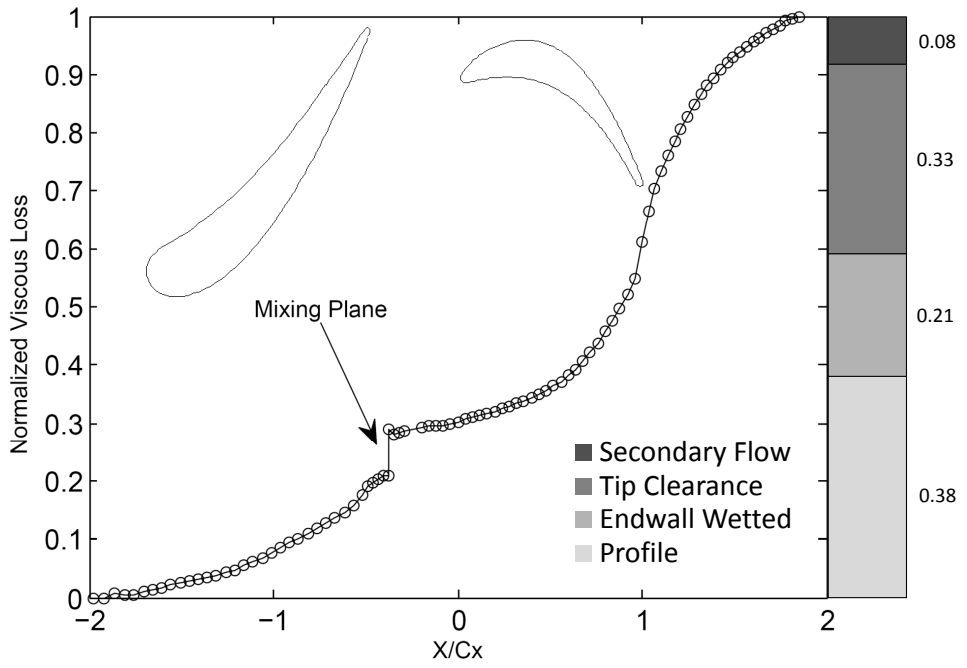


Figure 4-1: ACCUMULATED VISCOUS LOSS FOR BASELINE CASE WITH NO PURGE FLOW

## 4.2 Delineating Loss Sources

As discussed in chapter 3, quantitative assessment of viscous losses must be based on Eqn. (3.9) and not on volume integration of $\dot{S}'''_{visc}$. Indeed, the results in Fig. 4-1 are based on the former method. However, it is also instructive to compare loss estimates based on $\dot{S}'''_{visc}$, in order to identify which loss categories are not being resolved accurately by this latter method. The procedure for delineating the four baseline loss categories, using each of these two methods, is as follows:

1. Profile loss is calculated at midspan. The flow here is approximately two dimensional and the two dimensional limits of Eqn. (3.13) and Eqn. (3.14) are used (note that in the baseline case with no purge flow, thermal mixing losses are negligible, so that a direct use of change in entropy as a measure of viscous loss is acceptable). In an analogous fashion to Eqn. (3.13), Eqn. (4.1) subtracts the mass-flow averaged specific entropy at a given axial location on a midspan surface, from reference inlet specific entropy. The integrals for entropy and mass flux used in averaging are performed over lines of constant radius on the

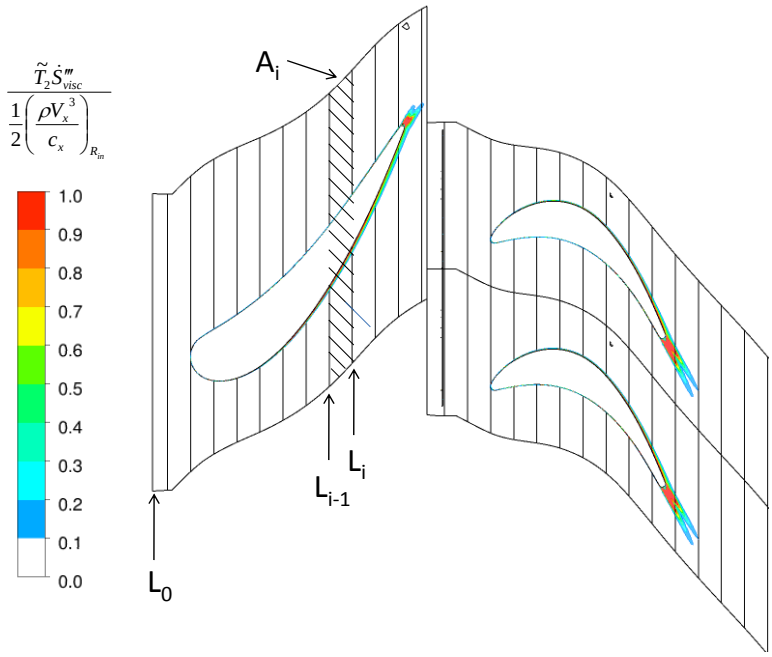


Figure 4-2: ENTROPY GENERATION RATE PER UNIT VOLUME AT MIDSPAN

midspan surface, as indicated in Fig. 4-2 by $L_0 - L_i$.

$$\Delta s_{profile} = \frac{\int_{L_i} s\rho V_x r d\theta}{\int_{L_i} \rho V_x r d\theta} - \frac{\int_{L_0} s\rho V_x r d\theta}{\int_{L_0} \rho V_x r d\theta} \tag{4.1}$$

Alternatively, profile loss in terms of specific entropy change can be computed using Eqn. (4.2)

$$\Delta s_{profile} = \sum_{i=1}^{n} \frac{\iint_{\mathcal{A}_j} \dot{S}'''_{gen} d\mathcal{A}}{\int_{L_j} \rho V_x r d\theta} \tag{4.2}$$

Here $\dot{S}'''_{gen}$ is integrated over discretized strips of the midspan surface, $A_i$, an example of which is given in Fig. 4-2. The resulting entropy generation rate per unit span is normalized by mass flow per unit span, to give the change in specific entropy between axial locations $L_{i-1}$ and $L_i$.

2. Dissipation of mechanical energy due to endwall boundary layers is calculated using a constant dissipation coefficient ($Cd = 0.002$) and the local velocity-cubed relationship given in [17]. To express endwall wetted loss in terms of change in specific entropy, Eqn. (4.3) is used. (Note the use of relative and

absolute velocities)

$$\Delta s_{endwall} = \begin{cases} \frac{1}{\dot{m}} \int_{\mathcal{A}} \frac{C_d \rho V^3}{T} d\mathcal{A} & \text{for NGV hub/shroud, rotor shroud} \\ \frac{1}{\dot{m}} \int_{\mathcal{A}} \frac{C_d \rho W^3}{T} d\mathcal{A} & \text{for rotor hub} \end{cases} \tag{4.3}$$

Alternatively, volume integrals of $\dot{S}'''_{gen}$ can be performed over the bottom and top 1%-span of the stage, to capture the enrtopy generated due to endwall boundary layers while excluding that associated with secondary flow features. The 1%-span limit was chosen, as it corresponds to 0.8-1.5 boundary layer thicknesses. This approach for obtaining endwall wetted loss from $\dot{S}'''_{gen}$ is expressed in Eqn. (4.4)

$$\Delta s_{endwall} = \frac{1}{\dot{m}} \iiint_{span<1\%} \dot{S}'''_{gen} d\mathcal{V} + \frac{1}{\dot{m}} \iiint_{span>99\%} \dot{S}'''_{gen} d\mathcal{V} \tag{4.4}$$

3. Tip clearance loss can be inferred by subtracting the losses from a case with no tip clearance. A fillet was applied to the rotor tip to avoid corner separation for the case of no tip clearance.

4. Baseline secondary flow loss (which includes losses due to all vortical structures) is calculated as the remainder of the loss after subtracting out the profile, endwall and tip clearance losses.

The axial distribution of these loss mechanisms is presented in Fig. 4-3. Comparing the two methods for loss accounting suggests that $\dot{S}'''_{gen}$ is capable of capturing blade wetted losses relatively accurately, but severely underestimates all other losses. This is in line with the discussion in Chapter 3, where it was shown that $\dot{S}'''_{gen}$ can become a quantitative tool only in regions of sufficient mesh resolution. In this case, blade surfaces are well resolved with more than 12 nodes in the boundary layer, as shown in Fig. 4-4. Despite a similar y+ on the hub and shroud, there are much fewer nodal points in the endwall boundary layers, resulting in insufficient resolution of velocity gradients, and underestimation of endwall wetted losses based on $\dot{S}'''_{gen}$. Tip clearance

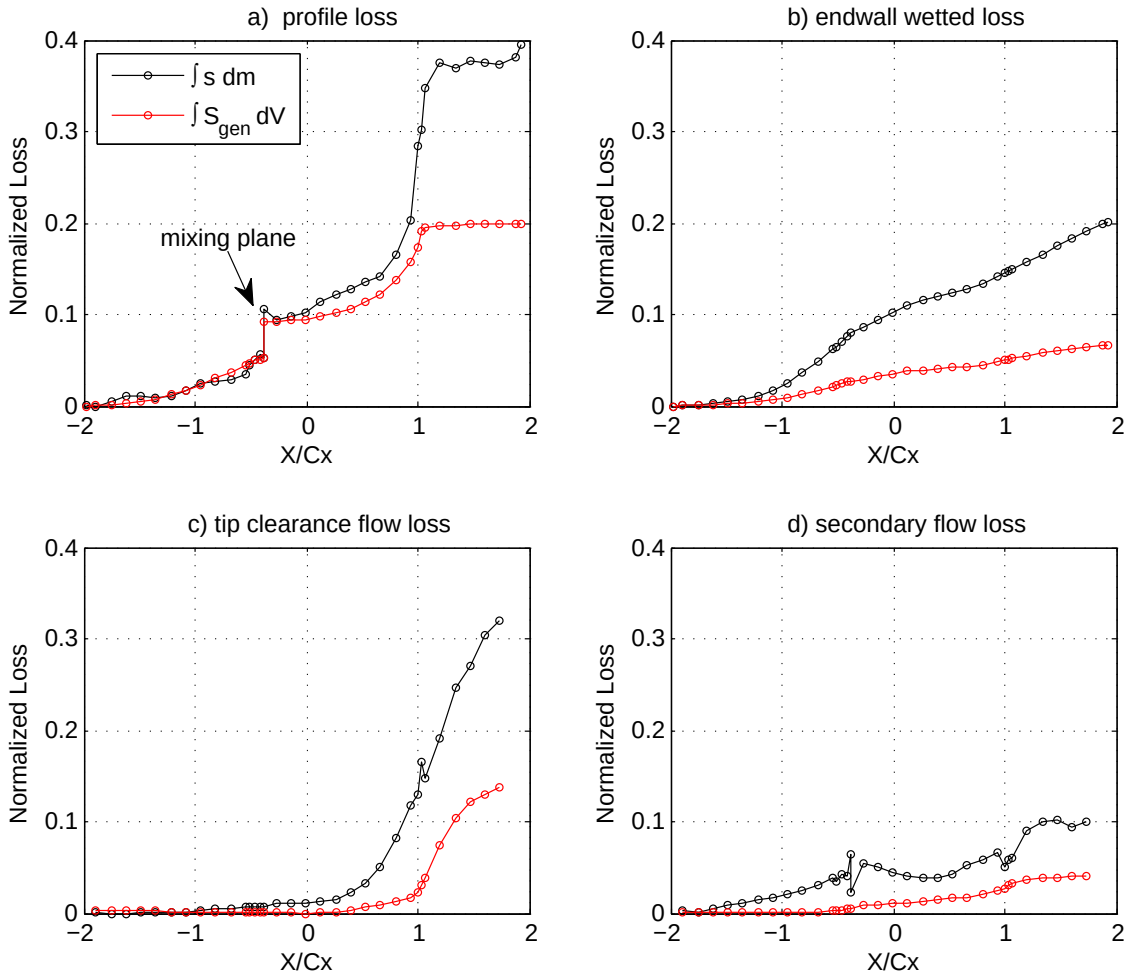


Figure 4-3: BREAKDOWN OF ACCUMULATED LOSS FOR BASELINE CASE WITH NO PURGE FLOW

flow, secondary flow and trailing edge losses are more obvious examples of flow features with high gradients in regions of insufficient grid resolution. These observations make a strong argument for the use of adaptive meshing based on velocity gradients. For our purposes, we will simply use differences in entropy flux (black curves in Fig. 4-3) for any quantitative conclusions, as this method demonstrates convergence at currently available grid resolutions. However, contours of $\dot{S}'''_{visc}$ are still a useful qualitative tool. In the next section, the $\int sdm$ curves in Fig. 4-3 will be examined in more detail, in conjunction with contours of $\dot{S}'''_{visc}$, to explain the main features of the baseline losses.

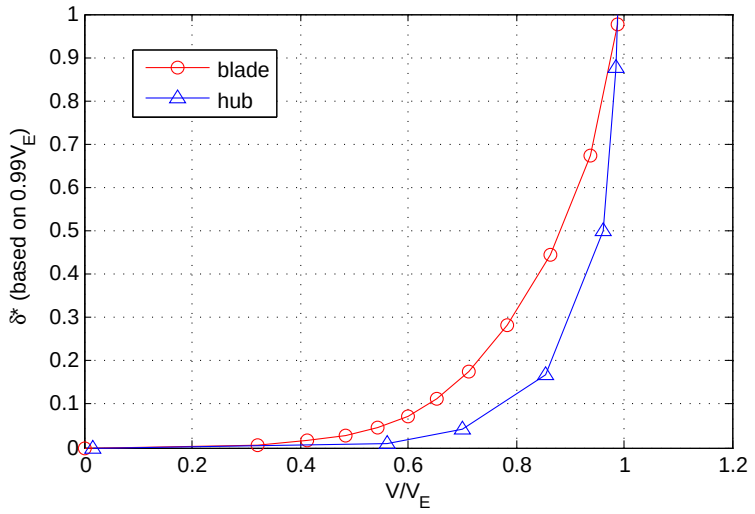


Figure 4-4: RESOLUTION OF BOUNDARY LAYERS ON BLADE AND ENDWALL SURFACES

## 4.3 Implications of Loss Source Delineation

In Fig. 4-3(a) we observe that the mixing plane loss is manifested in the two dimensional profile loss, indicating that it is due to the mixing out of the NGV wake and not due to any residual secondary flows. Another interesting characteristic of the stage profile loss is the amount by which rotor trailing edge loss exceeds NGV trailing edge loss - a factor of more than 4. Previous authors [17] suggest that 3/4 of the trailing edge loss is due to low base pressure behind blunt trailing edges. To a first approximation (based on the control volume analysis in [17]), this base pressure loss is proportional to trailing edge thickness to throat ratio, t/w, defined in Fig. 4-5. This ratio is more than three times larger for the rotor compared to the NGV, explaining most of the disparity between the two trailing edge losses.

Figure 4-3(b) shows how endwall losses accumulate at an increasing rate through the NGV, as free stream absolute Mach number increases. However, in the rotor, the hub and shroud see increasing and decreasing Mach numbers respectively and losses increase at a steady rate.

The other large contributor to loss is tip clearance flow, which can be seen to commence at about 50% rotor axial chord in Fig. 4-3(c). The phenomenon is also evident in Fig. 4-6, where contours of $\dot{S}'''_{visc}$ at various axial cuts through the rotor

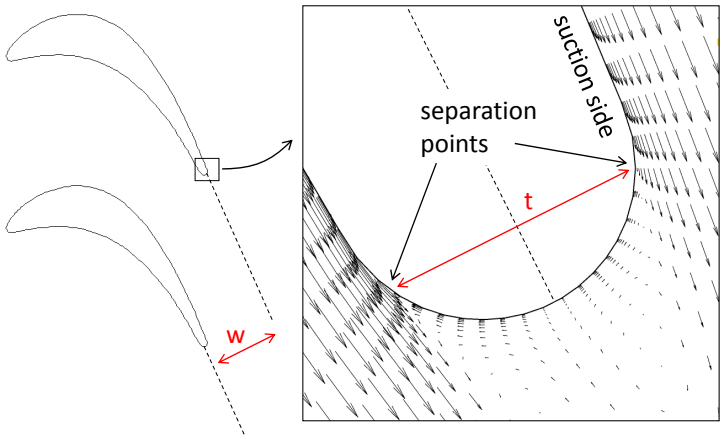


Figure 4-5: ROTOR THROAT AND TRAILING EDGE THICKNESS DEFINITIONS

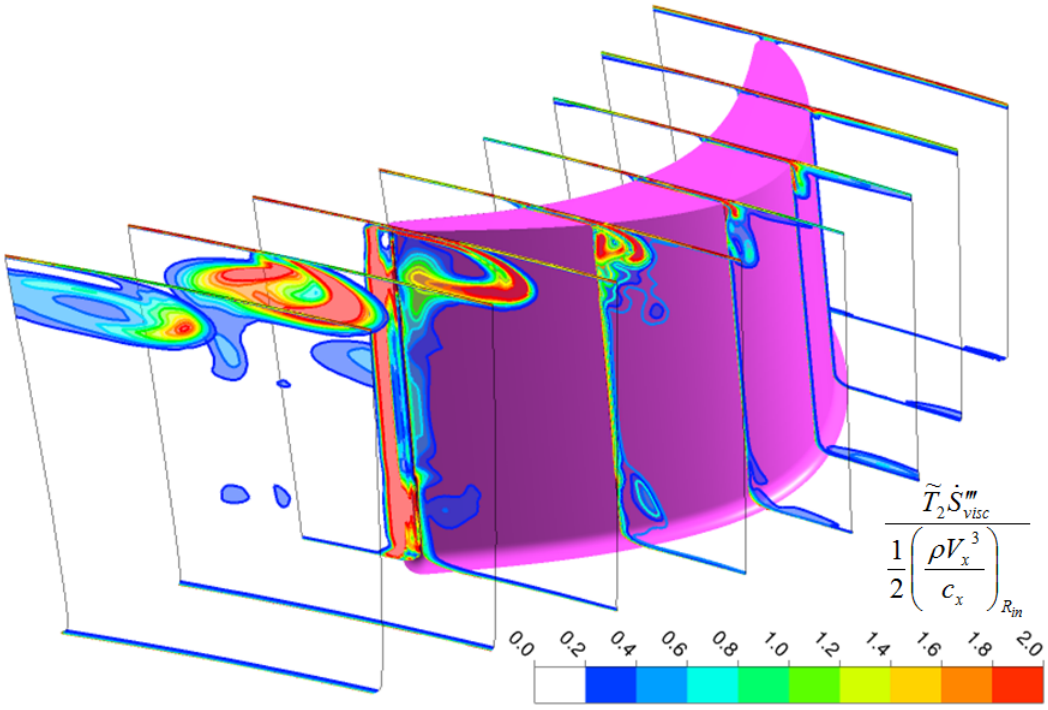


Figure 4-6: ENTROPY GENERATION RATE PER UNIT VOLUME AT AXIAL PLANES THROUGH ROTOR

($x/c_x = 0-1.4$) show high enrtopy generation rates near the blade tip. The computed results also indicate that the tip-clearance flow vortex results in loss generation well downstream of the rotor trailing edge[1].

In Figure. 4-6 it is also possible to observe a region of loss that is associated with

[1]Personal correspondence with colleague Arthur Huang, who is studying tip clearance flow losses in detail, confirms this finding

the hub passage vortex (there is a similar region of loss associated with the shroud passage vortex, but it is somewhat obscured by the dominant tip clearance flow losses). This secondary flow loss will be discussed in detail in the next chapter, but here it is pointed out that its contribution to the baseline losses is small - approximately 8% according to the computed results in Figure 4-3(d).

## 4.4 Summary of Baseline Losses

To summarize the loss characteristics of the baseline turbine stage, we note significant base pressure and tip clearance flow losses. The fact that tip clearance flow losses play a major role, and that most of these losses are generated downstream of the rotor trailing edge, will be relevant to the discussion of additional purge flow effects. Secondary flow losses in the baseline case amount to about 8% of total stage losses.

In this chapter it was also shown that $\dot{S}'''_{visc}$ is capable of capturing wetted loss if there are more than 12 nodes in the boundary layer. For all other losses, particularly those away from the well resolved surfaces, $\dot{S}'''_{visc}$ underestimates the entropy generated but provides qualitatively accurate trends.

# Chapter 5

# Purge Flow-Induced Losses

When purge air is injected upstream of the rotor, additional losses are incurred beyond those in the baseline case described in chapter 4. This chapter will first illustrate where these additional losses are generated. Subsequently, the chapter will focus on the physics of four distinct effects that were found to be responsible for these changes in loss. These effects are:

1. a shear layer between purge and mainstream flows
2. an increase in secondary flow losses associated with gradients in radial velocity
3. increased tip clearance flow and wetted losses, due to increased reaction
4. suppression of tip-clearance flow due to shroud-injected purge flow

These effects will be discussed in the order listed, with an emphasis on establishing the causal relationship between flow features and loss generation. Quantitative comparison of these effects, as well as an assessment of purge flow design parameters, will be presented in the next chapter.

## 5.1 Where are Purge Flow Losses Generated?

The first step in understanding how purge flow losses come about is to identify where they occur. Figure 5-1 compares the accumulated loss for two cases with purge flow, comparing them to the accumulated losses through the baseline stage that were

discussed in the previous chapter. The two purge flow cases shown have the nominal purge flow parameters[1] $mf = 1.5\%,\ sf = 0\%,\ gf = 5\%,\ \phi = 30°$. Losses increase immediately downstream of the purge slot, and continue to do so through the rotor passage for the hub-injection case. For the case of shroud-injection, the additional lossses generated through the rotor are significantly lower.

The net effect of purge flow on loss generation is brought out more clearly by subtracting out the baseline losses, to yield the results shown in Fig. 5-1(b). Here we also observe a reduction in loss through the NGV. Note also that the purge flow loss profiles for the two cases are similar up to the rotor leading edge. Beyond that point, hub-injected purge flow continues to monotonically increase stage losses. In contrast, the irregular rise and fall of net purge flow loss in the shroud-injection configuration suggests the presence of a competing beneficial effect.

To gain further insight, as to where the additional losses due to purge flow are being generated within the rotor passage, we refer to Fig. 5-2. This figure shows the *change* in volumetric entropy generation rate, $\Delta\dot{S}'''_{visc}$, relative to the baseline case with no purge flow, plotted on axial cuts spanning $x/c_x = 0 - 1.4$. For the case of hub-injected purge flow, Fig. 5-2(a) points out a number of regions with increased entropy generation rate. It will be shown in the following sections that the increased losses in region "A" are due to a viscous shear layer between purge and mainstream flows, those in region "B" are due to secondary flow enhancement, and the increased wetted loss and tip clearance flow loss are due to an increased degree of reaction. For the case of shroud injection, these same effects occur near the shroud, but there is a substantial reduction in the tip clearance flow losses. This last effect will be shown to account for the lower penalty of purge flow injected at the shroud.

[1]These parameters were chosen intentionally. The highest mass fraction in our design space was used to illicit a clear response in purge flow losses. A swirl fraction of zero was used, since that is what the purge flow would have if no specific measures were taken to pre-swirl purge flow. The narrowest gap fraction in the design space was chosen to minimize the variation of purge flow across the gap, thereby simplifying the situation. Finally, a 30° injection angle was chosen because no chamfer is needed for this configuration, once again keeping the flow near the purge slot exit simple.

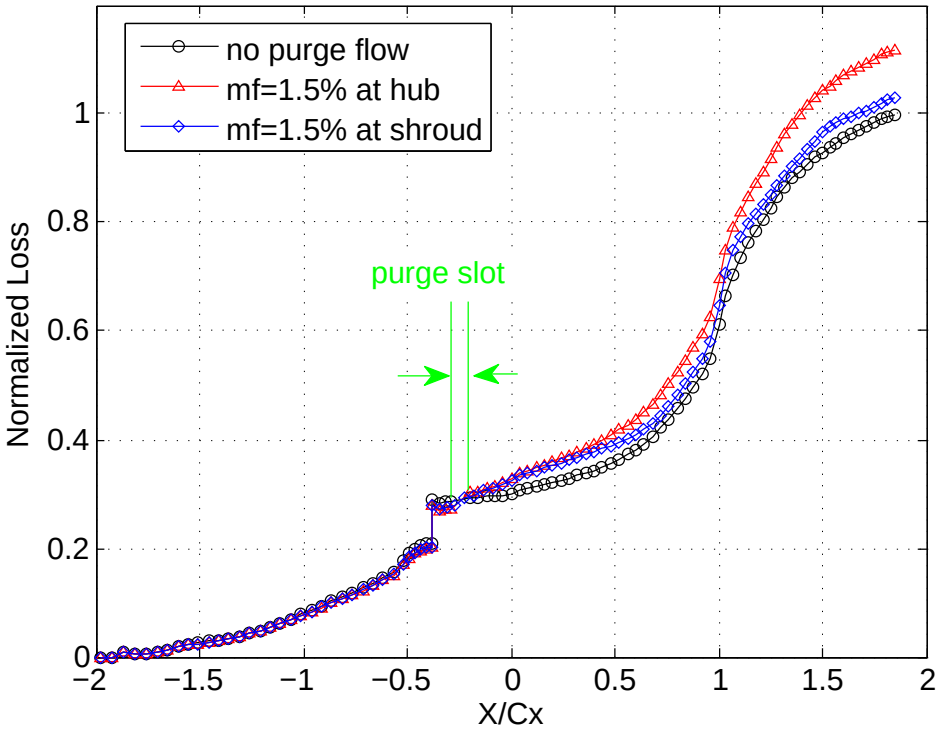


(a) Total accumulated viscous loss

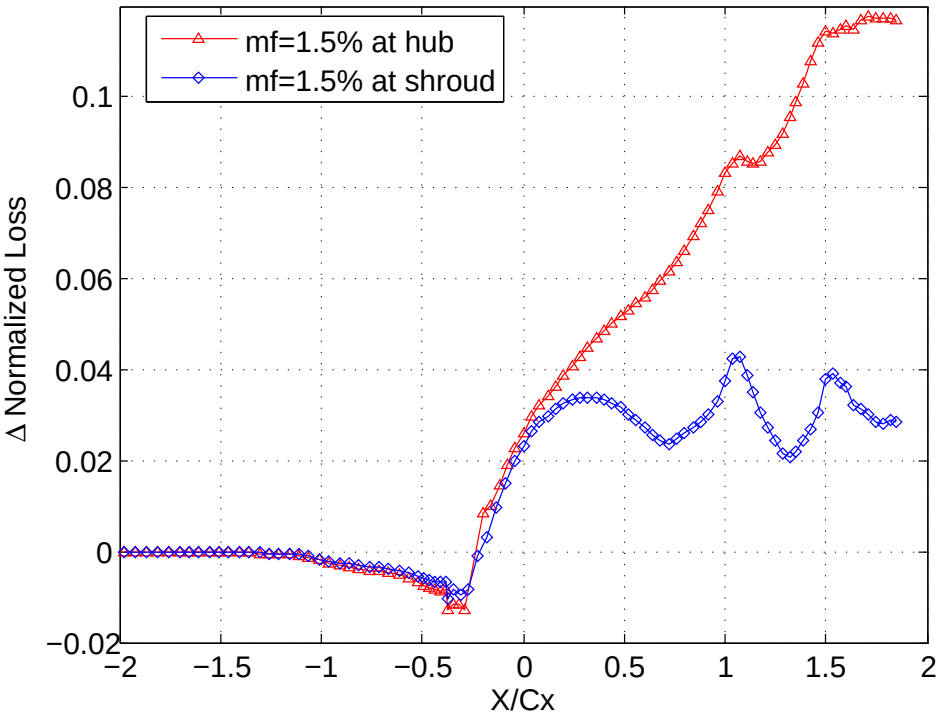


(b) Net purge flow loss

Figure 5-1: AXIAL ACCUMULATION OF TOTAL VISOCUS LOSS AND NET PURGE FLOW LOSS. NOMINAL PURGE FLOW PARAMETERS: $mf = 1.5\%$, $sf = 0\%$, $gf = 5\%$, $\phi = 30°$

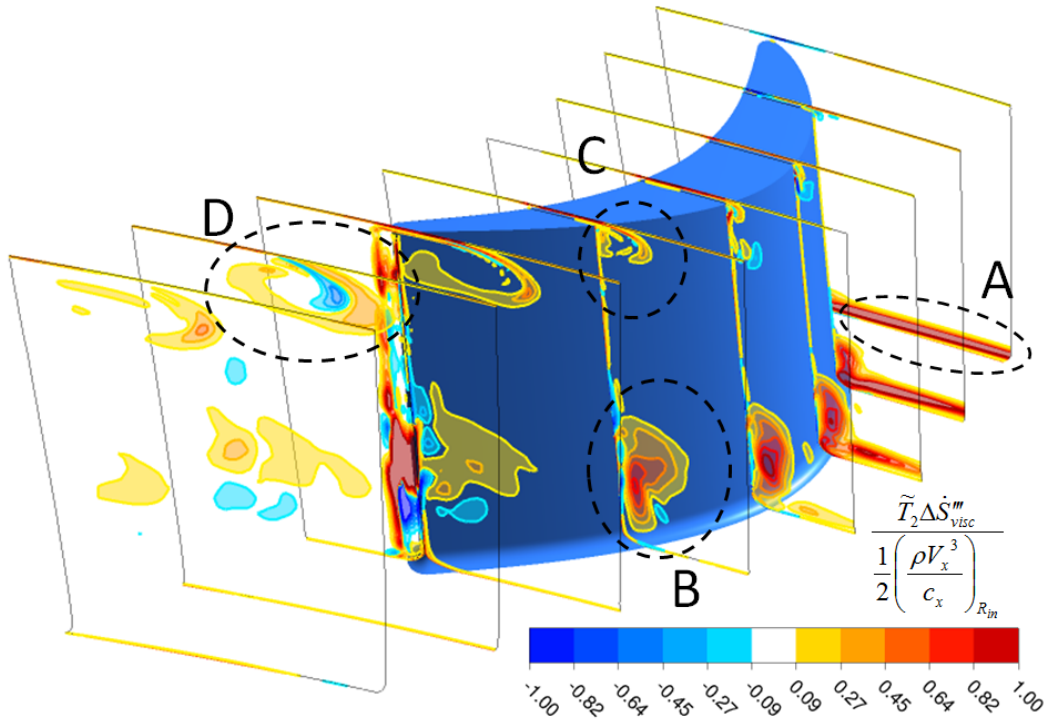


(a) Purge flow injected at hub

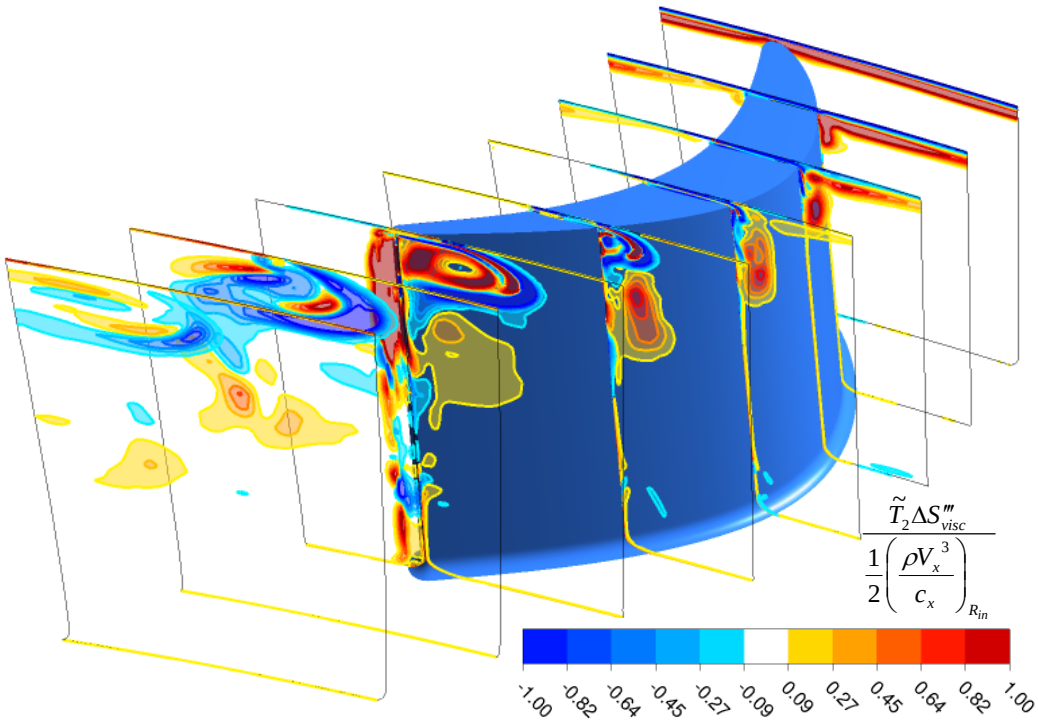


(b) Purge flow injected at shroud

Figure 5-2: CHANGE IN ENTROPY GENERATION RATE PER UNIT VOLUME RELATIVE TO BASELINE CASE. NOMINAL PURGE FLOW PARAMETERS: $mf = 1.5\%$, $sf = 0\%$, $gf = 5\%$, $\phi = 30°$

## 5.2 Viscous Shear Layer

When purge flow is injected into the main stream, its velocity generally differs from the mainstream flow in both direction and magnitude. The resulting shear layer, at the interface between the purge and main streams, generates entropy as the velocity gradients are dissipated through viscous action. This is the phenomenon that is responsible for the $\Delta\dot{S}'''_{visc}$ in region "A" of Fig. 5-2(a), and the corresponding region near the shroud in Fig. 5-2(b). It will first be shown that this shear layer is essentially an axisymmetric effect, which will then allow us to study its parametric dependence on purge flow design parameters using an analytical approach.

### 5.2.1 Axisymmertic nature of the shear layer

The viscous shear layer is the only purge flow loss mechanism present in the axisymmetric model of Fig. 2-1(a). It is convenient to demonstrate that the three dimensional shear layer is similar enough to that in the axisymmetric case, so that understanding of the latter can be applied to the former.

The characteristics of the shear layer loss are observed most clearly in $\dot{S}'''_{visc}$ contours on a meridional plane, shown for the axisymmetric and three dimensional models in Fig. 5-3. The locus of points with maximum entropy generation rate outline the interface between purge and mainstream flows. Comparing Fig. 5-3(a) and Fig. 5-3(b) one can see an obvious similarity in the entropy generation rate contours: highest entropy generation rates occur near the upstream edge of the purge slot (where the gradients are highest) and most of the losses appear to be generated upstream of the rotor blade. In the presence of the rotor blade, purge flow emerges from the cavity in a circumferentially non-uniform manner. The mid-pitch meridional plane depicted in Fig. 5-3(b) happens to have slightly lower losses than the axisymmetric case (other circumferential locations have slightly higher losses than the axisymmetric case).

For a more quantitative comparison, we turn to accumulated loss curves. The same procedure that was used to factor out baseline losses in the three dimensional case, resulting in Fig. 5-1(b), can be performed on the axisymmetric configuration.

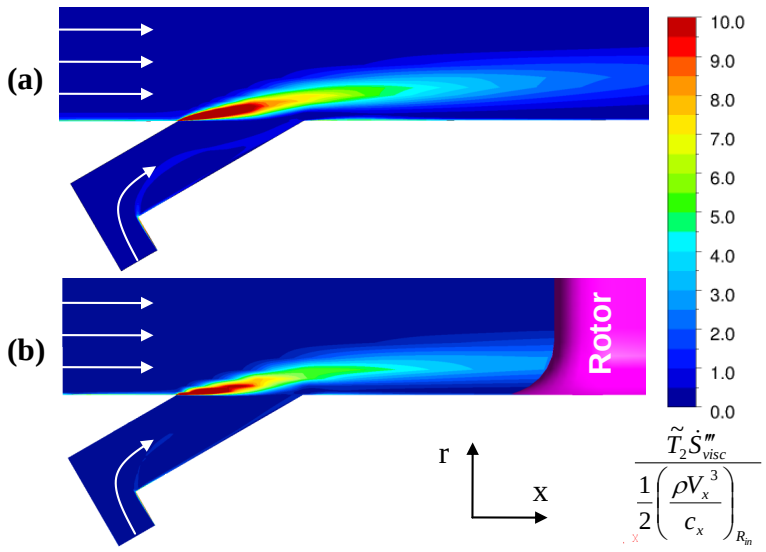


Figure 5-3: MERIDIONAL VIEW OF $\dot{S}'''_{visc}$ IN SHEAR LAYER (a)AXISYMMETRIC MODEL (b) THREE DIMENSIONAL ROTOR PASSAGE.

In Fig. 5-4, the net accumulated purge flow loss in the axisymmetric case is compared to that in the three dimensional blade passage. There is excellent agreement between the two loss profiles up to a point where most of the shear layer loss has been realized (about 30% axial chord from the rotor leading edge). Beyond that point additional loss mechanisms (which will be discussed later in the chapter) come into play for the three dimensional case.

### 5.2.2 Control volume analysis of shear layer loss

Agreement between the axisymmetric and three dimensional purge flow losses upstream of $x/c_x = 0.3$, demonstrates that the shear layer loss can be treated as an axysimmetric effect. Therefore, we can use an axysimmertic control volume mixed-out analysis, based on that outlined by Young and Wilcock[10], to gain insight into how the shear layer loss scales. Young and Wilcock's analysis was modified to include mainstream and purge flow swirl, as outline in Appendix B.1, resulting in Eqn. (5.1).

$$\Delta s_{visc} = \frac{\dot{m}_b}{\dot{m}_a}\left[\frac{(V_{x,a}-V_{x,b})^2 + (V_{r,a}-V_{r,b})^2 + (V_{\theta,a}-V_{\theta,b})^2}{2T_a}\right] \tag{5.1}$$

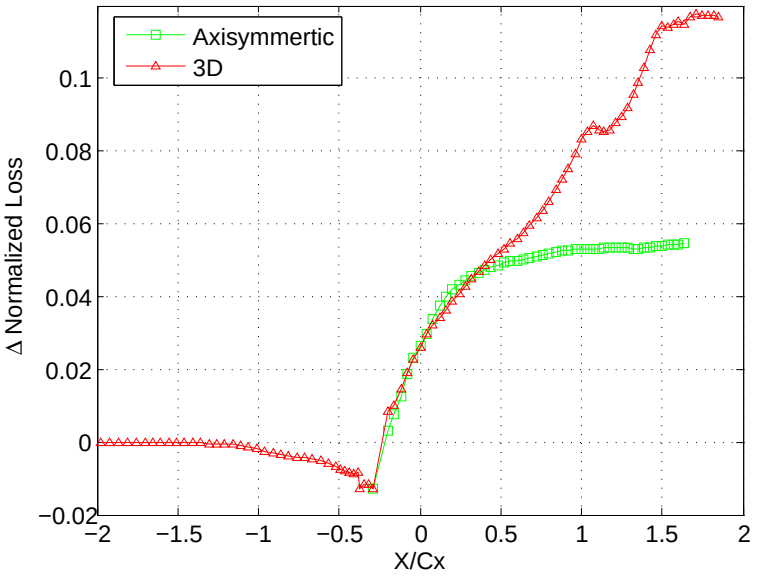


Figure 5-4: AXIAL ACCUMULATION OF NET PURGE FLOW LOSSES, THROUGH AN AXISYMMETRIC ANNULUS AND THREE DIMENSIONAL BLADE PASSAGE.

The quantities in this equation can be expressed in terms of the non-dimensional purge flow parameters under investigation, allowing for an expedient parametric study of their effects on entropy generation. The results from such an analysis are assessed against CFD results in Fig. 5-5(a). To be consistent with the CFD results in Fig. 5-4, entropy change from the mixed out analysis is related to lost work through Eqn. (3.9) and normalized by the baseline stage losses. Data points from CFD estimate somewhat lower losses, due to the fact that the flow is not fully mixed out at the exit of the computational domain. Nevertheless, the CFD results do corroborate trends with respect to all purge flow design parameters. Appendix B.2 presents a further modification to Young and Wilcock's analysis that accounts for incomplete-mixing. Figure 5-5(b) demonstrates that when the mixed out condition is relaxed, analytical results agree with CFD in quantitative terms as well. Though a detailed discussion on the effectiveness of purge flow parameters in managing losses will be presented in the next chapter, here we point out that shear layer loss is dominated by the term $(V_{\theta,a} - V_{\theta,b})^2$ in Eqn. (5.1). This term is exclusively a function of $sf$, while the other terms are functions of $gf$ and $\phi$. This explains why Fig. 5-5 shows a greater decrease in shear layer loss with $sf$, as compared to the effects of $gf$ and $\phi$.

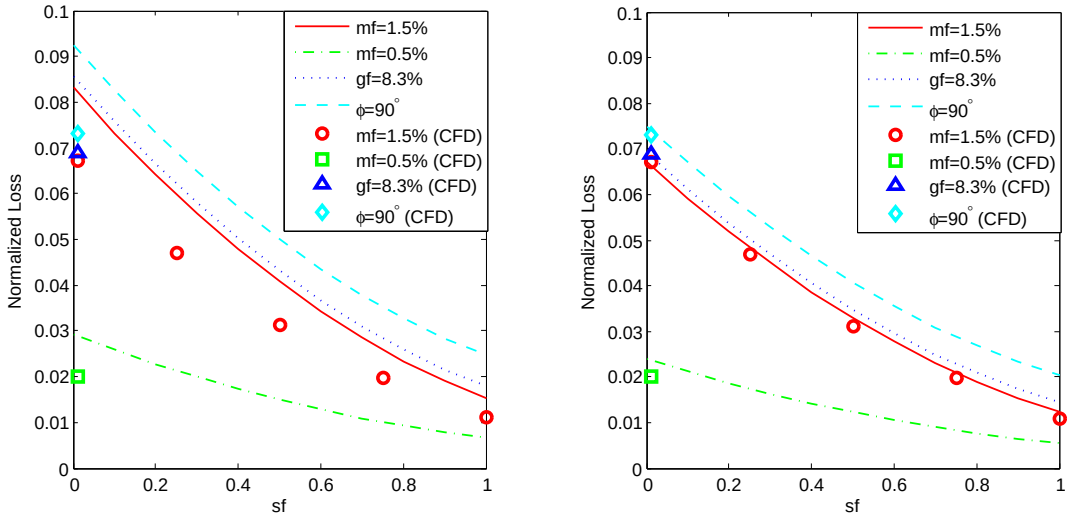


(a) CFD results compared to Young and Wilcock's analysis modified for swirling flow

(b) CFD results compared to Young and Wilcock analysis with mixing layer modification

Figure 5-5: COMPARISON OF SHEAR LAYER LOSSES BASED ON YOUNG AND WILCOCK'S ANALYSIS AND CFD

## 5.3 Purge-Secondary Flow Interaction

In Fig. 5-4 it can be seen that, when purge flow is injected at the hub in the presence of a downstream rotor blade, the additional losses incurred exceed what would be expected from mixing out of a shear layer. Previous authors [3][18][6][4] have commented on the potential for purge flow to interact with secondary flow structures, such as the passage vortex, to generate additional losses. Indeed, we noted that the increased entropy generation rate in region "B" of Fig. 5-2(a) is likely related to purge-secondary flow interaction. However, we seek a more direct causal relationship between secondary flow and loss. After defining secondary flow more rigorously, it will be shown that the passage vortex is not directly responsible for significant losses in either baseline or purge flow cases. Rather it is the generation of high radial velocity gradients on the blade suction surface that is the primary contributor to secondary flow losses in this region. This new insight will explain how purge flow leads to enhanced secondary flow losses, and why the swirl velocity of purge flow is an important parameter in this phenomenon.

### 5.3.1 Definition of secondary flow

In this context, we define the concept of secondary flow to be flow normal to the circumferentially averaged meanline flow direction. This includes spanwise flow in the meridional plane and "cross-flow" in the blade-to-blade plane. For the nearly two dimensional geometry of the turbine stage under investigation, using radial flow in lieu of spanwise flow is a good approximation that simplifies analysis considerably. To define cross-flow more rigorously, Fig. 5-6(a) demonstrates the transformation from axial and circumferential to streamwise and cross-flow velocity. Later in the chapter it will be convenient to approximate the polar coordinate system defined by streamwise, cross flow and radial directions $(s, c, r)$ with a set of local Cartesian coordinates $(s', c', r')$. These Cartesian coordinates are a result of rotating the global $(x, y, z)$ coordinates to align with the streamline direction as illustrated in Fig. 5-6(b).

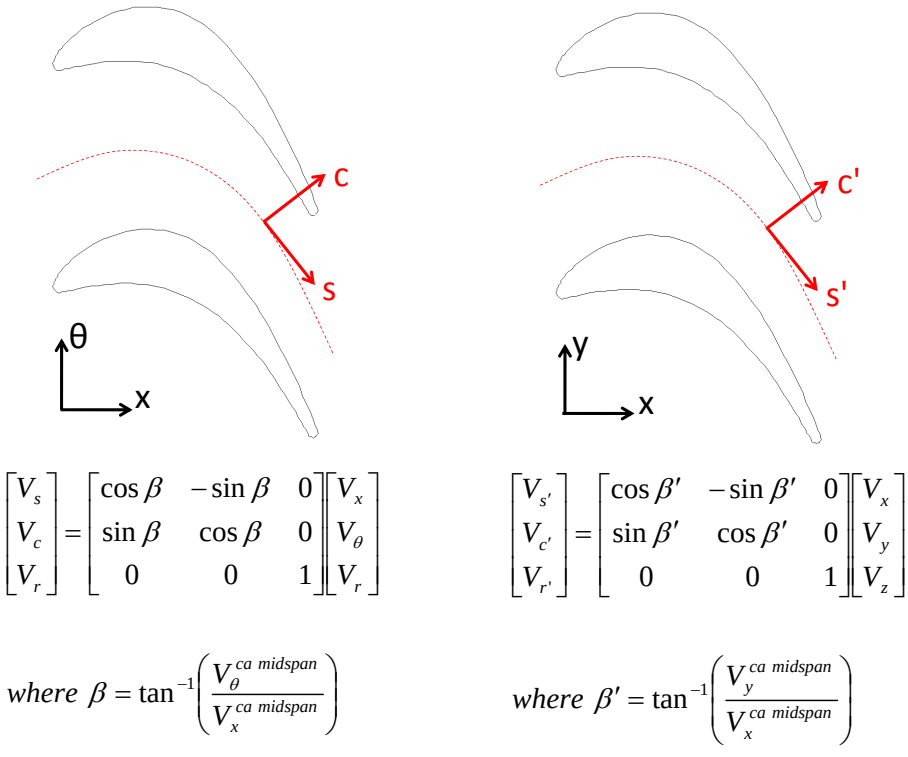


$$\begin{bmatrix} V_s \\ V_c \\ V_r \end{bmatrix} = \begin{bmatrix} \cos\beta & -\sin\beta & 0 \\ \sin\beta & \cos\beta & 0 \\ 0 & 0 & 1 \end{bmatrix} \begin{bmatrix} V_x \\ V_\theta \\ V_r \end{bmatrix} \qquad \begin{bmatrix} V_{s'} \\ V_{c'} \\ V_{r'} \end{bmatrix} = \begin{bmatrix} \cos\beta' & -\sin\beta' & 0 \\ \sin\beta' & \cos\beta' & 0 \\ 0 & 0 & 1 \end{bmatrix} \begin{bmatrix} V_x \\ V_y \\ V_z \end{bmatrix}$$

$$\text{where } \beta = \tan^{-1}\left(\frac{V_\theta^{\,ca\ midspan}}{V_x^{\,ca\ midspan}}\right) \qquad \text{where } \beta' = \tan^{-1}\left(\frac{V_y^{\,ca\ midspan}}{V_x^{\,ca\ midspan}}\right)$$

(a) Polar streamwise and cross flow velocities

(b) Cartesian approximation of streamwise and cross-flow velocities

Figure 5-6: Definition of streamwise and cross-flow velocities

Because we are dealing with a high hub-to-tip ratio machine $\left(\frac{r_{hub}}{r_{tip}} = 0.9\right)$ this is a good approximation.

### 5.3.2 Role of hub passage vortex

For the case of hub injection, direct interaction between purge flow and secondary flow features occurs only near the hub. The important secondary flow feature in this region has long been considered to be the hub passage vortex. However, by focusing on the region marked "B" in Fig. 5-2(a), it will be shown that local entropy production is not a direct consequence of the vortical structure.

Figure 5-7 superimposes contours of $\dot{S}'''_{visc}$ on top of the secondary flow field (i.e. cross-flow and radial velocity). Three cases are shown: the baseline case with no purge flow, a case with purge flow injected with no swirl, and a case with purge

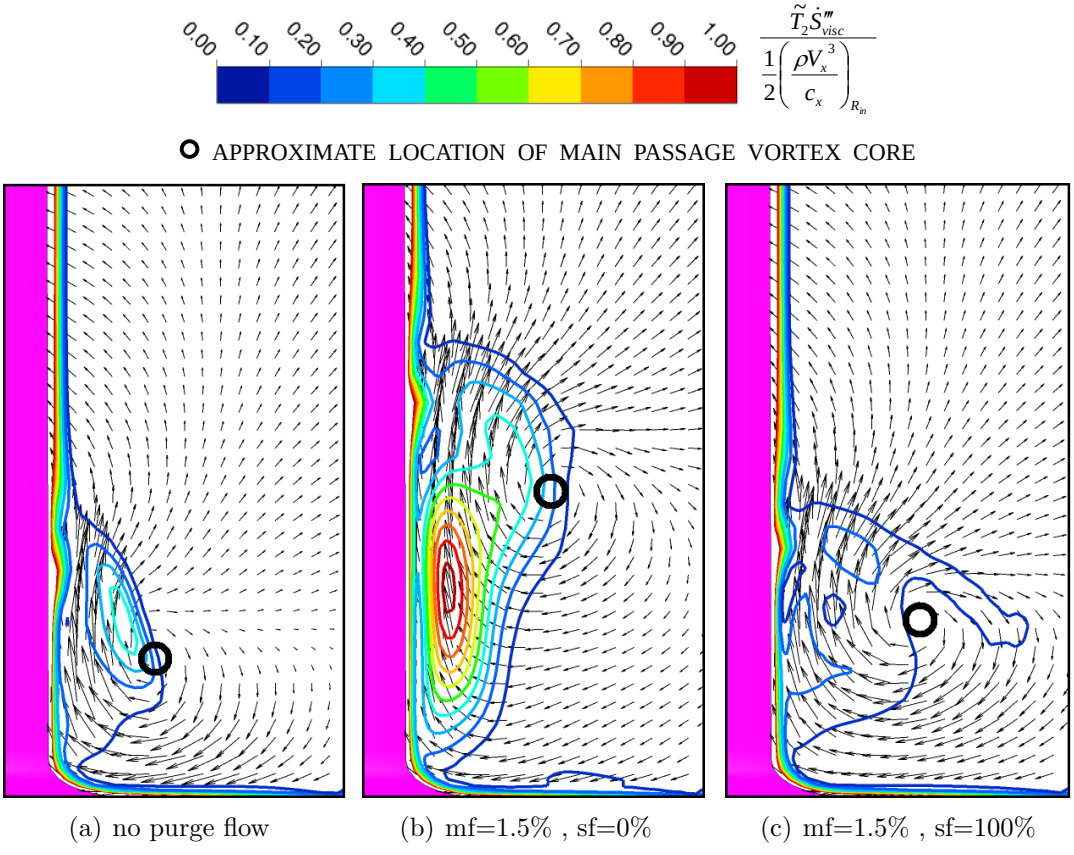


(a) no purge flow (b) mf=1.5% , sf=0% (c) mf=1.5% , sf=100%

Figure 5-7: ENTROPY GENERATION RATE PER UNIT VOLUME IN REGION "B" OF FIG. 5-2(a) IN THE PLANE $x/c_x = 0.8$

flow that is pre-swirled to rim speed. The flow fields in Fig. 5-7 show a distinct hub passage vortex in each of the three cases, the core of which is marked by a circle. It is clear that when purge flow is injected, this core is displaced towards midspan, but when the same purge flow is swirled, the vortex core resides at approximately the same radial location as in the baseline case. This behavior has been observed by a number of other authors [8][18][19]. Though there is an increase in the circulation of the passage vortex for the case with non-swirled purge flow, it is no more than 8%. The second notable feature of Fig. 5-7 is the substantial increase in entropy generation rate associated with purge flow injection - an effect that is once again mitigated by pre-swirling purge flow. Finally, Fig. 5-7 clearly shows that, in each of the three cases, the region of high entropy generation rate does not coincide with the main vortex core.

This last observation is a new finding, which challenges the widespread interpretation that the passage vortex cores is the primary source of secondary flow loss. Thus far, the literature ([19] [18] [6]) has justified this view based on the observed correspondence between the location of the passage vortex and regions of low stagnation pressure. Low stagnation pressure does reflect that viscous losses have been generated, but that could have occurred somewhere upstream, with low stagnation pressure fluid having been convected to the current location. Therefore, changes in stagnation pressure cannot precisely be traced back to the specific flow processes responsible. Figure 5-7 uses volumetric entropy generation rate, which is not a convected quantity, but rather a direct measure of the local rate of entropy production, to call into question the specific role of the vortex in generating viscous loss. These doubts are strengthened by the fact that the large increase in secondary flow loss due to purge flow is disproportionate to the increase in vortex circulation. The next section will present an in-depth investigation into this issue, and identify the flow features that are directly responsible for losses in this region.[2]

[2]It has been suggested by Professor Nick Cumpsty that the so-called "passage vortex" is really not a vortex at all, but rather a three dimensional separation region with a complex topology. The objective here is to describe what that topology is and how it comes to generate losses

### 5.3.3 Velocity gradients dominating secondary flow loss

In order to understand the physical cause for the secondary flow losses in the vicinity of the passage vortex, it was necessary to identify the velocity gradients dominating local entropy production. For this purpose, we would like to express $\dot{S}'''_{visc}$ in terms of the polar streamline coordinates $(s, c, r)$ defined in Fig. 5-6(a), and identify the terms in Eqn. (3.11) that have the largest contribution. However, because the rotor has a high hub-to-tip ratio, and since it is convenient to work with Cartesian coordinates[3], the rotated Cartesian coordinate system $(s', c', r')$ will be used instead (refer to Fig. 5-6). Appendix C.2 demonstrates how the expression for $\dot{S}'''_{visc}$, given earlier in tensor notation as Eqn. (3.11), can be expanded as Eqn. (5.2)

$$\dot{S}'''_{visc} = \frac{\mu_{eff}}{T} \left\{ \begin{array}{l} 2\left[\left(\frac{\partial V_{s'}}{\partial s'}\right)^2 + \left(\frac{\partial V_{c'}}{\partial c'}\right)^2 + \left(\frac{\partial V_{r'}}{\partial r'}\right)^2\right] + \\ \left(\frac{\partial V_{s'}}{\partial c'} + \frac{\partial V_{c'}}{\partial s'}\right)^2 + \left(\frac{\partial V_{s'}}{\partial r'} + \frac{\partial V_{r'}}{\partial s'}\right)^2 + \left(\frac{\partial V_{c'}}{\partial r'} + \frac{\partial V_{r'}}{\partial c'}\right)^2 \end{array} \right\} \tag{5.2}$$

Using this formulation of $\dot{S}'''_{visc}$, and evaluating the necessary gradients as discussed in Appendix C.2, we can infer approximate statements regarding the contributions of gradients in $V_s, V_c$ and $V_r$ to entropy generation rates in the passage vortex region. Upon expanding bracketed terms and systematically plotting each of the terms in Eqn. (5.2), the results are summarized in Fig. 5-8. It can be seen that, both for the baseline case and the case with purge flow, the losses in the vicinity of the passage vortex are almost entirely due to $\left(\frac{\partial V_{r'}}{\partial c'}\right)^2$, while the remaining terms are either negligible or associated with boundary layer losses. (The non positive-definite term $2\frac{\partial V_{r'}}{\partial c'}\frac{\partial V_{c'}}{\partial r'}$ arises from expanding the last bracket in Eqn. (5.2)). Although Fig. 5-8 focuses on the axial plane at 80% axial chord, the results at other axial locations within the blade passage are similar.

The gradient $\frac{\partial V_{r'}}{\partial c'}$ can be visualized clearly in Fig. 5-9, where the blade-to-blade variation in the secondary flow field is superimposed on the contribution to $\dot{S}'''_{visc}$ associated with the $\left(\frac{\partial V_{r'}}{\partial c'}\right)^2$ term. High radial velocities (in excess of the rotor hub

[3]It is much simpler to express $\dot{S}'''_{visc}$ in Cartesian coordinates. In addition, gradients of velocity in $(s', c', r')$-coordinates are easily backed out from the available solution variables in CFX

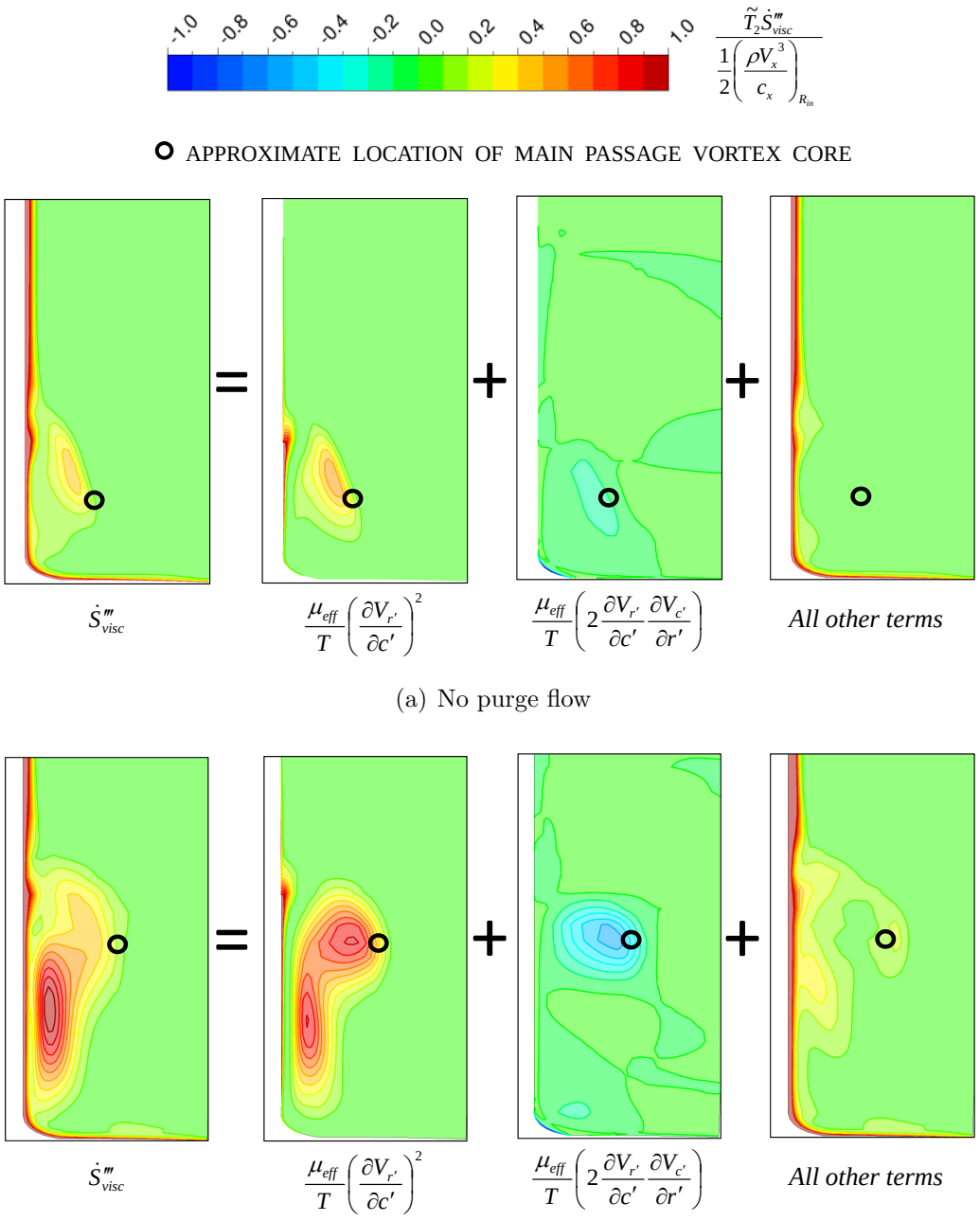


(a) No purge flow

(b) mf=1.5% , sf=0%

Figure 5-8: DECOMPOSITION OF ENTROPY GENERATION RATE PER UNIT VOLUME IN REGION "B" OF FIG. 5-2(a) INTO SIGNIFICANT AND NOT SIGNIFICANT TERMS.

speed) are shown to develop between the vortex core and the suction side of the passage. This effect is more pronounced when purge flow in injected.

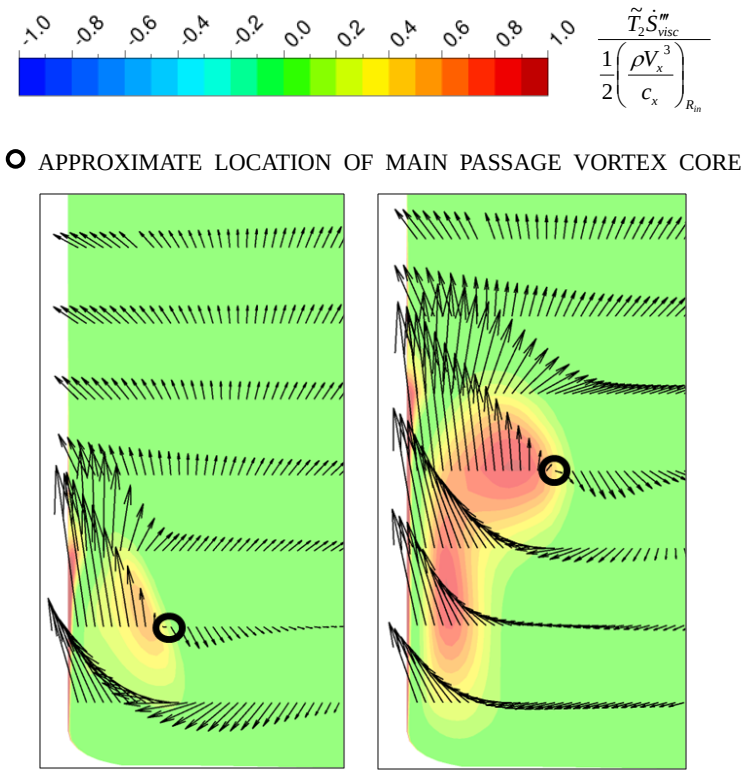


(a) No purge flow (b) mf=1.5% , sf=0%

Figure 5-9: SECONDARY FLOW FIELD AND ENTROPY GENERATION RATE ASSOCIATED WITH $\left(\frac{\partial V_{r'}}{\partial c'}\right)^2$ IN REGION "B" OF FIG. 5-2(a)

### 5.3.4 Traceability of purge-secondary flow interaction loss

Having identified the physical cause of the losses in the vicinity of the passage vortex, we seek to rationalize how these losses are enhanced by purge flow. To to this, it is first necessary to consider the root cause of the radial velocities generated on the blade suction surface. Once this root cause is recognized, the effect of purge flow injection will be evident.

The generation of radial velocities can potentially be associated with two effects: cross-flow being directed radially as it comes up against the blade surface, and streamwise flow being diverted in the radial direction as a consequence of flow blockage. These two possible routes for generating radial velocities near the blade suctions surface are summarized and illustrated, using the limiting streamline pattern on the blade in Fig. 5-10. The former mechanisms can be inferred intuitively from Fig. 5-9.

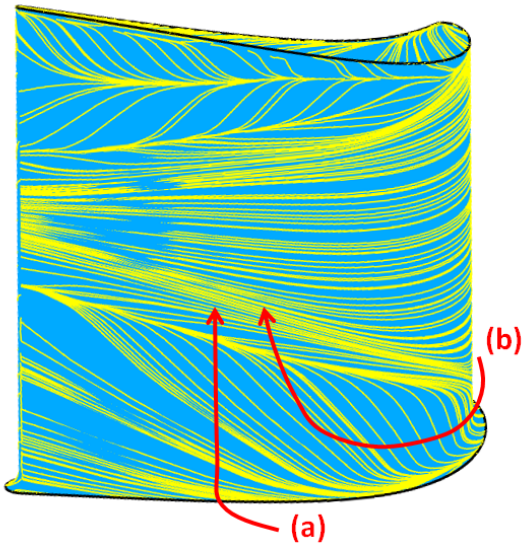


Figure 5-10: Limiting streamlines of blade suction surface, illustrating two routs for generation of radial velocities.

The latter mechanisms is postulated based on the fact that decreased streamwise velocity is observed in the region of high radial velocity. Figure 5-11(a) illustrates this on the 80%-chord plane. Another perspective is provided in Fig. 5-11(b), showing streamwise and radial velocities on a blade-to-blade line at a radius cutting through the passage vortex core (dashed line in Fig. 5-11(a)). As a reference, Fig. 5-11(b) also gives the streamwise velocity profile at misdpan. The blockage effect is manifested as a deficit between the streamwise velocity at the radius of the vortex and that at midspan.

It is difficult to quantify the relative contributions of these two mechanisms in generating radial flow. In fact, it is possible that they are both manifestations of the same effect: the blockage observed could be the result of entrainment of low momentum fluid from the endwalls, rather than an additional cause for generation of radial flow. However, this distinctions is less important when one considers that both of these mechanisms have the same root cause. In the first instance (mechanism "a" in Fig. 5-10), blade-to-blade cross-flow is directly responsible for fluid being diverted in the radial direction. In the second (mechanism "b" in Fig. 5-10), it is again cross-flow that is responsible for the development of the passage vortex [20][21] and the

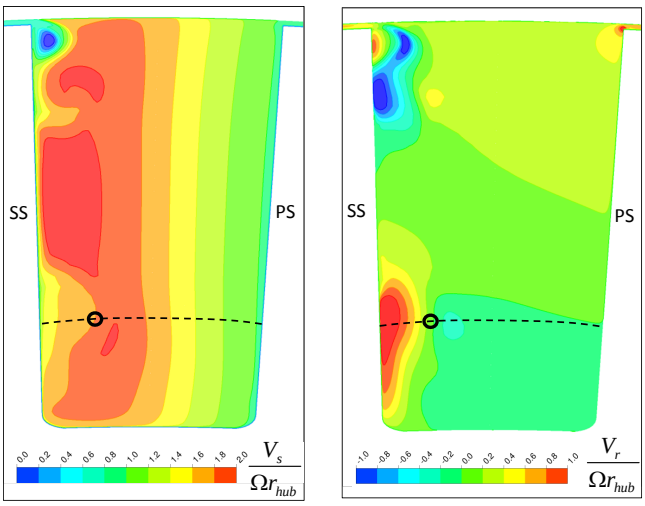


(a) Contours of streamwise and radial velocity on an axial cut across the passage at 80% axial chord. Black circle indicates location of passage vortex core

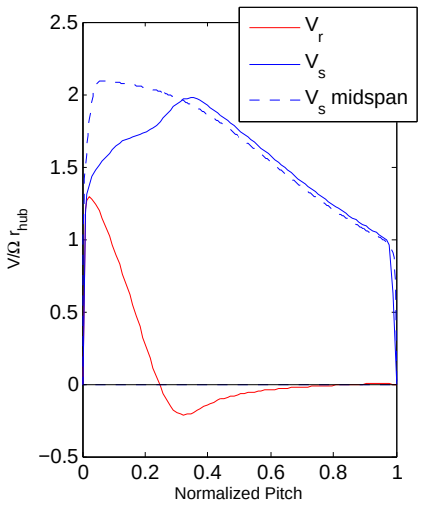


(b) Blade-to-blade profiles of streamwise and radial velocity, cutting through passage vortex core

Figure 5-11: RADIAL VELOCITY GENERATION AS A CONSEQUENCE OF BLOCKAGE. $x/c_x = 0.8$, $mf = 1.5\%$, $sf = 0\%$, $gf = 5\%$, $\phi = 30°$

blockage effect associated with it.

In the baseline case with no purge flow, cross-flow exists near the endwalls due the higher turning of low momentum fluid under the action of the blade-to-blade pressure gradient. When purge flow is injected without swirl, in the frame of reference of the rotor, this purge flow has a strong cross-flow component. Figure 5-12 shows the circumferentially averaged cross flow profile at various axial cuts through the rotor, for the baseline case with no purge flow, a case with non-swirled purge flow, and a case with purge flow swirled to rim speed. It can be seen that for the baseline case, a cross-flow layer near the hub begins to form at about 20% axial chord. This eventually leads to the development of a passage vortex, the core of which can clearly be discerned (labeled Core 1) near 20% span at the rotor exit plane. When purge flow is introduced with no swirl, the cross-flow layer near the hub, and consequently the passage vortex, are given an early start. The result of this is primarily reflected, not in the vortex strength, but in the vortex core being displaced toward midspan (Core 2). Swirled purge flow results in a secondary flow field closly resembling that in the baseline case.

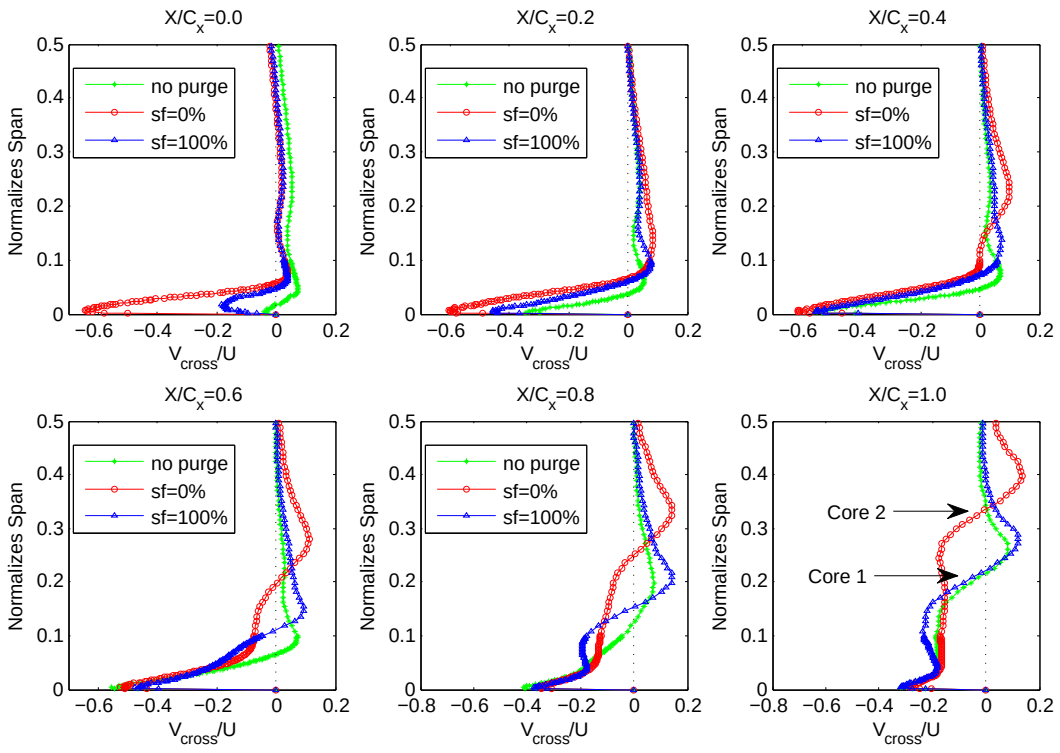


Figure 5-12: CIRCUMFERENTIALLY AVERAGED CROSS-FLOW

The significance of early development and radial migration of the passage vortex is two-fold: more fluid is swept under the vortex and towards the blade suction surface, and the blockage effect associated with the vortex is increased. Both of these characteristics enhance the generation of radial flow on the blade suction surface. Figure 5-13 shows the radially averaged blade-to-blade profiles of radial velocity (the radial averaging is applied over the bottom 50% span only). We find higher average radial velocities on the suction side of the blade, which is indicative of higher $\frac{\partial V_{r'}}{\partial c'}$. As shown earlier in this section, it is this radial velocity gradient that is responsible for the majority of secondary flow loss commonly associated with the passage vortex. Undesrstandably, purge flow injected without swirl leads to higher losses. Pre-swirling purge flow prior to injection eliminates the driving force for early development and radial migration of the passage vortex, thereby mitigating the secondary flow losses associated with purge flow.

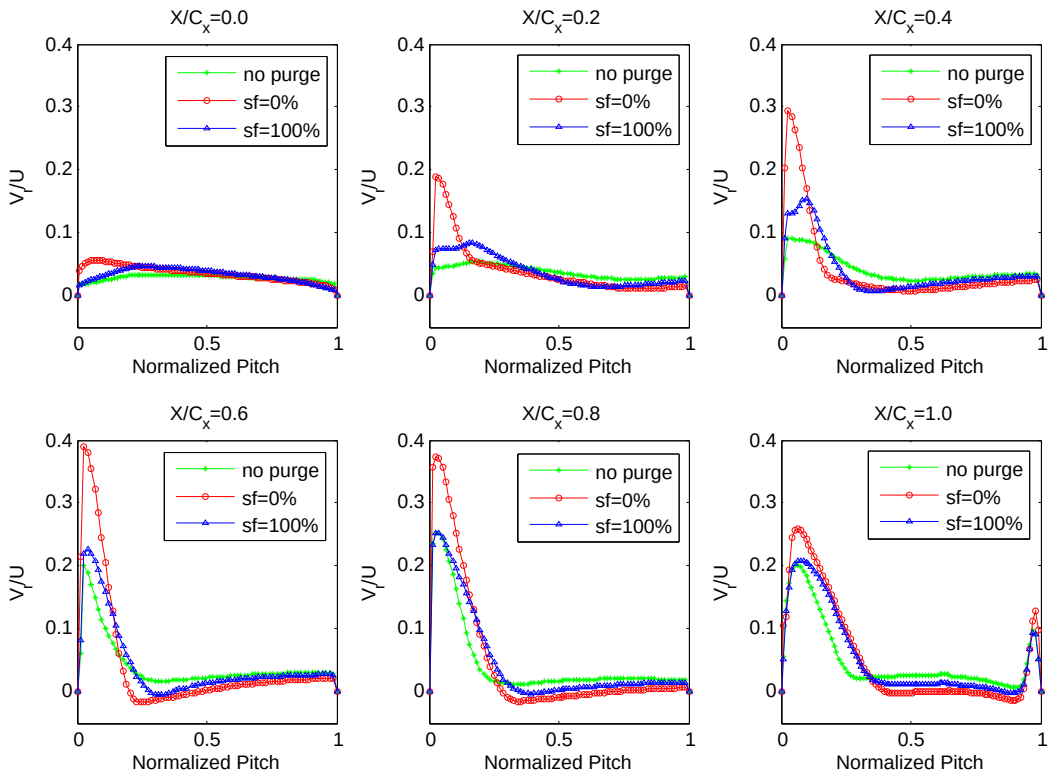


Figure 5-13: RADIAL VELOCITY AVERAGED OVER THE LOWER 50% SPAN

## 5.4 Losses due to Change in Reaction

As noted in the discussion of Fig. 5-2(a), aside from the increased losses in the vicinity of the passage vortex, there are also increases in the entropy generation rate near the blade tip and over most of the wetted surfaces of the rotor passage. The reduction in losses through the NGV, shown in Fig. 5-1(b) must also be addressed.

The reduction in loss through the NGV has been observed previously in [1], where it was attributed to an increased degree of reaction - a consequence of the blockage effect introduced with purge flow injection. However, it is important to realize that this change in reaction, while reducing the losses through the NGV, also accounts for some of the increased losses through the rotor. Changes in reaction due to cooling and purge flows are taken into account in the design process[4], but in our current research, it is important to be aware of this effect, so that one does not mistakenly attribute

[4]Personal communications with Dr. David Little, Siemens Energy Inc.

all of the additional rotor losses in Fig. 5-4 to the purge-secondary flow interaction discussed in the previous section.

For the present configuration, injecting 1.5% purge flow increases the degree of reaction from 0.412 to 0.439. Another way of looking at it is that the operating point of both NGV and rotor is shifted as illustrated in Fig. 5-14, with less pressure drop $\left(\frac{P_t}{P}\right)$ through the NGV but more pressure drop $\left(\frac{P_{t,rel}}{P}\right)$ through the rotor. The higher pressure drop across the rotor indicates a higher pressure difference between the suction and pressure side of the blade, thus leading to higher tip clearance flow. In addition, the changes in pressure ratio indicate likewise changes in freestream Mach number, which in turn explains the decreased NGV losses and the higher wetted losses through the rotor. All of these changes are consistent with the observations in Fig. 5-2(a).

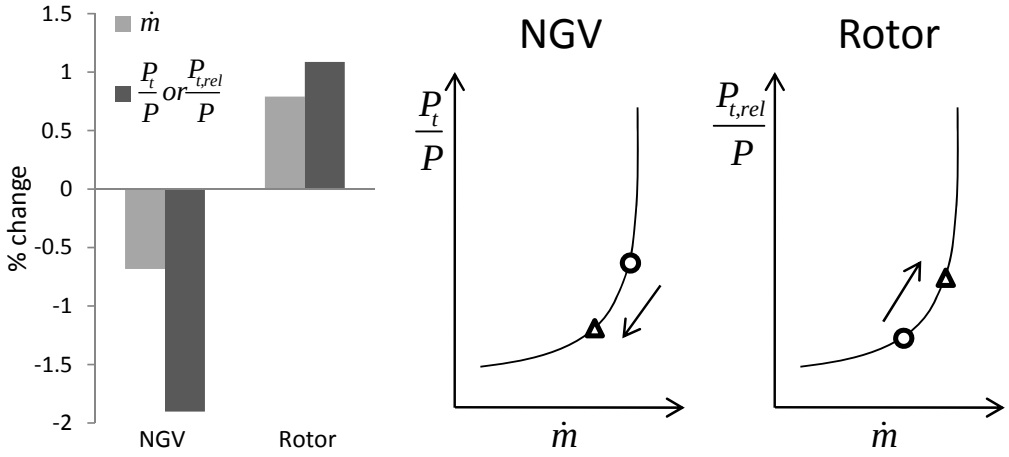


(a) Change in $\dot{m}$ and $\frac{P_t}{P}$

(b) Change in operating point

Figure 5-14: CHANGE IN OPERATING POINT FOR NGV AND ROTOR, mf=1.5% sf=0%

## 5.5 Purge-Tip Clearance Flow Interaction

When purge flow is injected from the shroud, the previously discussed effects are still present. However, it will be shown that an additional potential for purge flow interaction with tip clearance flow exist for unshrouded rotors. This effect will compensate

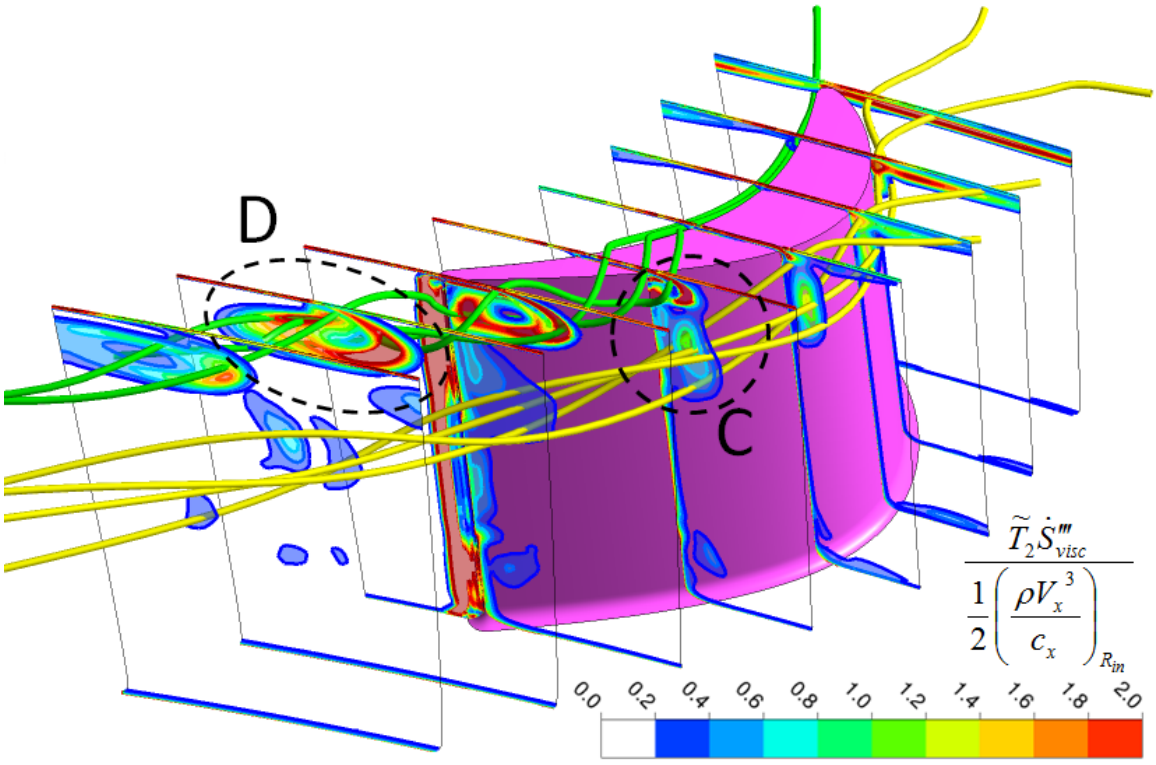


Figure 5-15: ISOMETRIC VIEW OF ROTOR, SHOWING $\dot{S}'''_{visc}$ CONTOURS, AND PARTICLE TRACES FROM TIP AND SHROUD-PASSAGE VORTEX REGIONS. 1.5% PURGE FLOW INJECTED AT THE SHROUD

for purge flow losses to a large extent, as was noted in Fig. 5-1(b).

The fact that losses due to the purge-mainstream shear layer are similar to those for hub-injected purge flow can be inferred from agreement between the curves in Fig. 5-1(b) up to the rotor leading edge. In terms of secondary flow effects, Fig. 5-15 shows the distinct loss regions associated with the counter-rotating tip clearance flow and passage vortices, for the case of shroud-injected purge flow. Figure 5-16 takes a closer look at the regions marked "C" and "D" both with and without purge flow.

Comparison between (Ci) and (Cii) demonstrates the migration of the passage vortex towards the midspan (passage vortex core is marked with a black circle). As in the case of hub-injection, the region of high loss that does not coincide with the passage vortex core, but is rather related to radial velocity gradient $\left(\frac{\partial V_r}{\partial c}\right)^2$, is clearly enhanced when purge flow is injected. Therefore, in addition to the similarity of shear layer loss between hub and shroud-injected purge flow, similar secondary flow losses

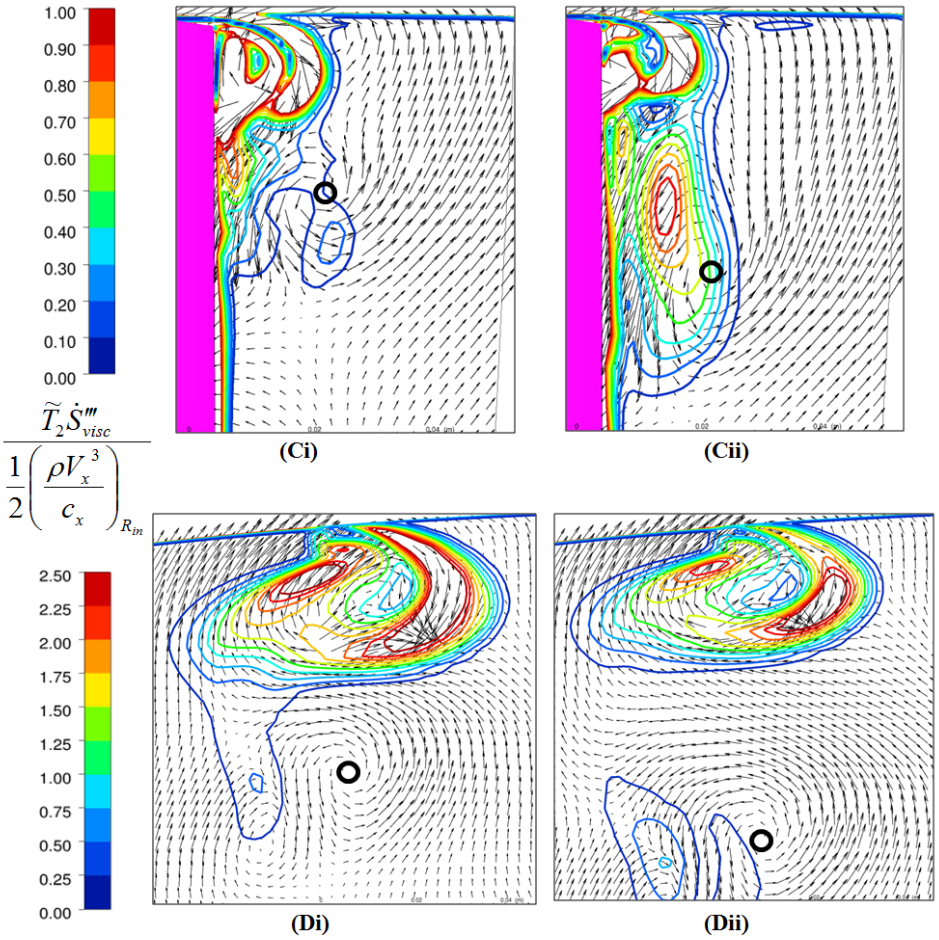


Figure 5-16: ENTROPY GENERATION RATE PER UNIT VOLUME IN REGIONS "C" AND "D" IN FIG. 5-15 FOR THE BASELINE CASE (Ci,Di) AND A CASE WITH 1.5% PURGE FLOW INJECTED AT THE SHROUD (Cii, Dii)

are generated in the vicinity of the passage vortex. However, despite an increase in degree of reaction, tip clearance flow loss has decreased dramatically. This reduction can be seen most clearly downstream of the blade, where most the tip clearance flow losses are realized, in (Di) and (Dii) of Fig. 5-16. Figure 5-2(b) shows the net effect of shroud-injected purge flow more clearly.

This reduction in tip clearance loss can be explained once again by thinking in terms of the cross-flow, introduced in the shroud region due to the non-swirled purge flow's relative motion in the rotating frame. Figure 5-17 shows the vector field in a plane halfway between the rotor tip gap, for a case with and without purge flow.

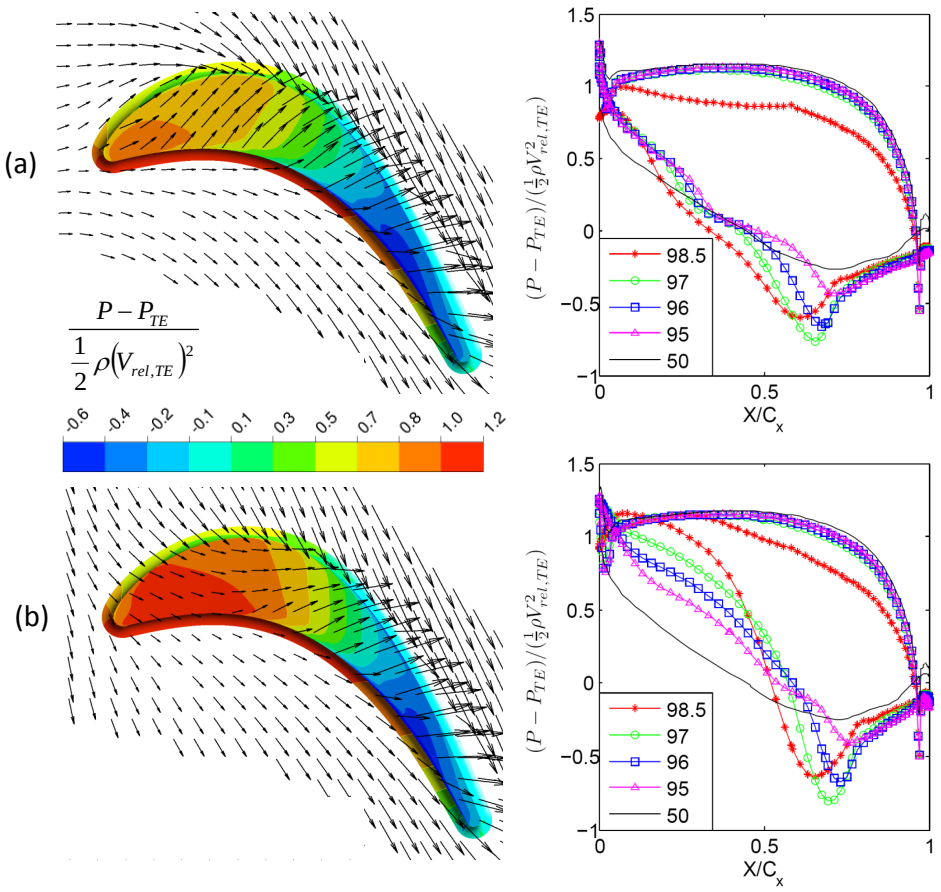


Figure 5-17: VELOCITY FIELD IN ROTOR FRAME OF REFERENCE, HALF WAY BETWEEN ROTOR TIP AND SHROUD, AND BLADE LOADING AT 95,96,97,98.5 AND 50% SPAN a)NO PURGE b)1.5% PURGE FLOW AT SHROUD

Figure 5-17(b) shows how the tangential momentum of the purge flow suppresses tip clearance flow in the forward part of the blade. The mechanism for suppression is essentially effective flow-turning in the tip region, arising from the momentum balance between mainstream and purge flows. Another way to think about it is that the negative incidence of the purge flow unloads the tip region, hence reducing the driving force for tip clearance flow. The blade loading distribution of the top 5% span is given in Fig. 5-17 to illustrate this point.

## 5.6 Implications for Purge Flow Upstream of First NGV

In general, purge flow is also injected upstream of the first NGV to cool the platform. Based on the understanding of purge flow loss effects gained through this work, one can make the following predictions: In terms of shear layer loss, there is no swirl in the mainstream flow entering the first NGV (immediately downstream of the combustor), so the shear layer associated with non-swirled purge flow injection would be weak. In addition, non-swirled purge flow does not lead to enhanced cross-flow, since it enters with zero incidence. Finally, the degree of reaction of the turbine stage is not changed. From these arguments, one would expect hardly any losses associated with this type of purge flow. Indeed, CFD results show no measurable purge flow losses for this configuration. The above does not apply to purge flow injected upstream of vanes other than the first NGV.

## 5.7 Summary of Purge Flow Loss Mechanisms

In this chapter, four mechanisms by which purge flow affects viscous losses were identified. These are summarized in Table 5.1, along with the purge flow features that drive them. The next chapter will give a quantitative account of the relative contributions these purge flow effects have on loss. Design guidelines, in terms of mitigating purge flow losses using the four design parameters under investigation, will also be presented.

Table 5.1: SUMMARY OF THE EFFECTS PURGE FLOW HAS ON LOSS

| Effect | Traceability of loss generation | Drivers |
|---|---|---|
| Shear layer | Purge-mainstream velocity deficit, leads to viscous shear | primarily $\Delta V_\theta$ |
| Secondary flow interaction | Cross flow and blockage due to the passage vortex both contribute to generating radial velocity gradients on the suction side of the blade. Non-swirled purge flow exacerbates both effects. | purge flow swirl in relative frame |
| Increased reaction | Purge flow blockage decreases $\frac{P_t}{P}$, $\dot{m}$, $M$ and wetted loss through NGV, but increases $\frac{P_{t,rel}}{P}$, $\dot{m}$, $M_{rel}$ and wetted + tip clearance losses through rotor. | purge flow mass fraction |
| Tip clearance flow interaction | Tangential momentum of purge flow in the relative frame suppresses tip clearance flow in the forward part of the blade | purge flow swirl in relative frame |

# Chapter 6

# Quantifying Effects of Purge Flow Design on Loss

Four ways by which purge flow affects viscous loss generation in a turbine stage have been identified in chapter 5. The discussion so far has been primarily qualitative, with a focus on understanding the flow physics. In this chapter, a quantitative comparison of the losses in different purge flow configurations will be presented. The understanding of the loss mechanisms, identified in the previous chapter, will help synthesize these quantitative results into design guidelines. The current results will also be assessed against published data.

## 6.1 Design Guidelines

A number of cases were modeled, in which purge flow parameters were systematically varied from the following nominal configuration: hub injection upstream of the rotor with $mf = 1.5\%,\ sf = 0\%,\ gf = 5\%,\ \phi = 30°$. The resulting purge flow losses are presented in Fig. 6-1(a). For clarity, the parameters that differ from the nominal values are highlighted.

As shown in Fig. 6-1(a), purge flow can result in a 12% increase in stage loss if injected at the hub, but the penatly is far smaller if injected at the shroud. Figure 6-1(a) also conveys the fact that, of the four purge flow design parameters investigated,

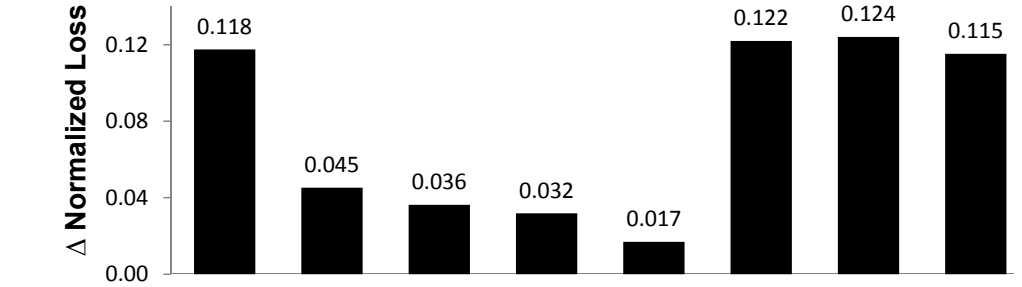


| Location | hub | hub | hub | shroud | shroud | hub | hub | hub |
|---|---|---|---|---|---|---|---|---|
| mf (%) | 1.5 | 0.5 | 1.5 | 1.5 | 1.5 | 1.5 | 1.5 | 1.5 |
| sf (%) | 0 | 0 | 100 | 0 | 100 | 0 | 0 | 0 |
| gf (%) | 5 | 5 | 5 | 5 | 5 | 8.3 | 5 | 2.5 |
| $\phi$ (deg) | 30 | 30 | 30 | 30 | 30 | 30 | 90 | 15 |

(a) Total purge flow losses

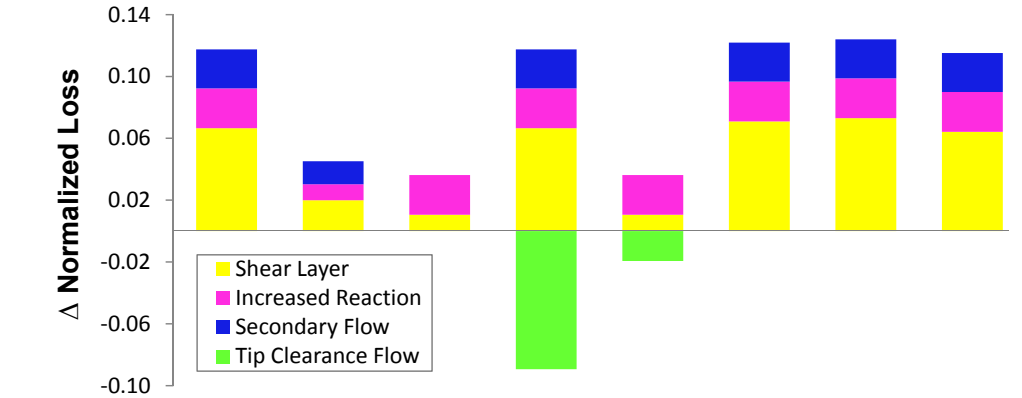


| Location | hub | hub | hub | shroud | shroud | hub | hub | hub |
|---|---|---|---|---|---|---|---|---|
| mf (%) | 1.5 | 0.5 | 1.5 | 1.5 | 1.5 | 1.5 | 1.5 | 1.5 |
| sf (%) | 0 | 0 | 100 | 0 | 100 | 0 | 0 | 0 |
| gf (%) | 5 | 5 | 5 | 5 | 5 | 8.3 | 5 | 2.5 |
| $\phi$ (deg) | 30 | 30 | 30 | 30 | 30 | 30 | 90 | 15 |

(b) Breakdown of purge flow loss

Figure 6-1: PURGE FLOW LOSSES FOR A NUMBER IF ILLUSTRATIVE CONFIGURATIONS

mass fraction and swirl fraction have substantially higher leverage on purge flow losses. To understand why that is, it is useful to view a breakdown of the purge flow losses in terms of the various mechanisms listed in Table 5.1. Such a decomposition is presented in Fig. 6-1(b). In the following discussion, the method for delineating the

loss mechanism will first be presented. Subsequently, the purge flow configurations that lead to substantial reduction in loss, and those that do not, will be rationalized, based on our understanding of the loss mechanisms and their drivers. This will allow design guidelines to be cast in terms of effective and ineffective purge flow parameters.

### 6.1.1 Delineating between loss mechanisms

The method for delineating between the loss mechanisms associated with purge flow injection, yielding the breakdown in Fig. 6-1(b), is illustrated in Fig. 6-2. The procedure is as follows: Shear layer loss is based on the axisymmetric results (labeled 'i' in Fig. 6-2). For the case of hub-injection into the three dimensional blade passage ($3D_{hub}$), purge flow losses beyond those found in the axisymmetric case (ii and iii) are due to the combined effect of change in reaction and purge-secondary flow interaction. The delineation between these two additional effects can be approximated

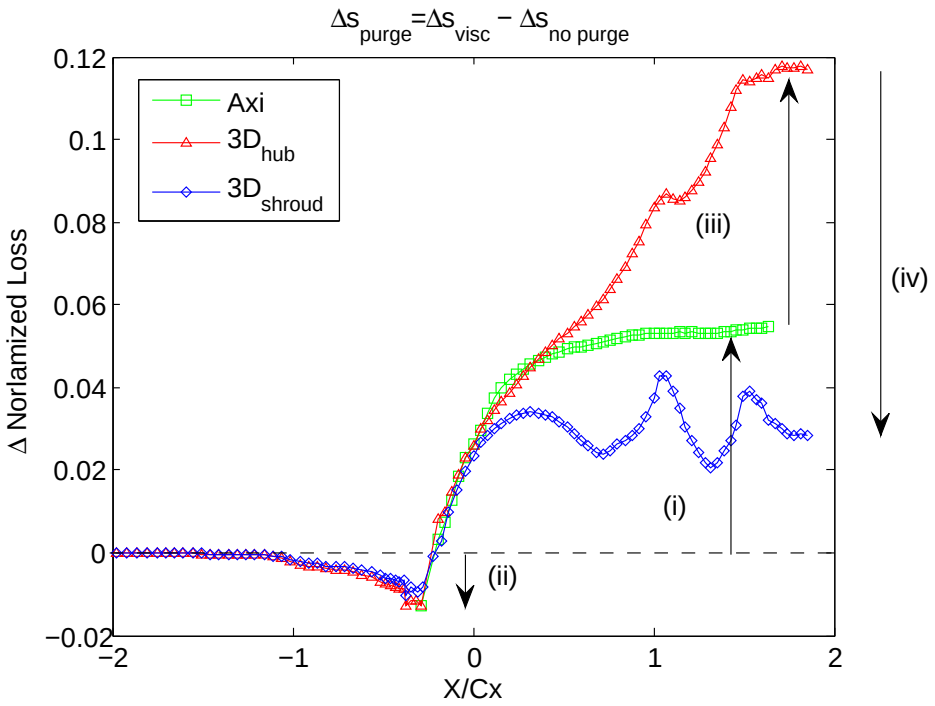


Figure 6-2: ACCUMULATED NET PURGE FLOW LOSSES FOR VARIOUS CASES, ILLUSTRATING PROCEDURE OF DELINEATING BETWEEN VARIOUS EFFECTS OF PURGE FLOW

by assuming that swirling purge flow to rim speed ($sf = 100\%$) elliminates purge-secondary flow interaction. This assumption is based on a qualitative comparison of the entropy generation rate contours in Fig. 5-7 and at other axial locations. On the other hand, the blockage effect of swirled and non-swirled purge flow is similar, since it is primarily a function of purge flow mass fraction. We therefore make the approximation that, for the case $sf = 100\%$, all losses beyond those due to the shear layer are due to change in reaction. The diference between $sf = 0\%$ and $sf = 100\%$ is then attributed entirely to purge-secondary flow interaction. The tip clearance flow suppression effect with shroud-injected purge flow is quantified by assuming that all other losses are the same as for hub-injection. Any difference in the losses between cases of hub and shroud-injection is attributed to tip clearance flow suppression(iv).

### 6.1.2 Effective design parameters

Comparing the first two configurations in Fig. 6-1(a) indicates that purge flow losses are almost proportional to mass fraction. Figure 6-1(b) shows that this is true for all of the purge flow loss mechanisms. The third configuration in Fig. 6-1(a) shows that swirling purge flow to rim speed reduces the penalty of purge flow injection by more than 2/3, relative to the nominal case. For intermediate values of swirl, Fig. 6-3 gives approximately quadratic scaling of loss.

The reason that purge flow swirl is such an effective design parameters is that it affects both shear layer and secondary flow losses. In addition, the shear layer loss, which amounts to 1/2 of the penalty, is dominated by the circumferential velocity deficit between purge and mainstream flows. Because the shear layer loss is such a significant contribution, the quadratic scaling in Fig. 6-3 can in part be explained by the quadratic dependence of shear layer loss on purge flow swirl velocity (see Fig. 5-5).

Referring back to Fig. 6-1(a) and Fig. 6-1(b), we note that in the case of shroud injected purge flow, total purge flow losses are not that high to begin with, due to the tip clearance flow suppression effect. On the other hand, swirling shroud-injected purge flow does not lead to significant further reduction in loss, since there is a tradeoff with the tip clearance flow suppression effect.

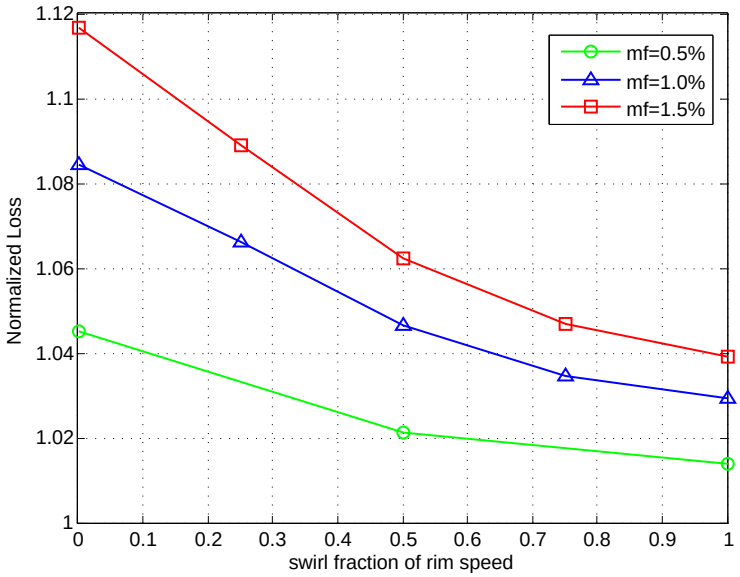


Figure 6-3: SCALING OF PURGE FLOW LOSSES WITH SWIRL AND MASS FRACTION

### 6.1.3 Ineffective design parameters

Figure 6-1(a) shows that gap fraction and injection angle yield at most a 6% change in purge flow losses over the entire design space. An additional case was generated with an even narrower gap and lower injection angle ($gf = 2.5\%,\ \phi = 15°$) to simulate the effect of an overlapping seal, however this did not lead to significant loss reduction either.

The lack of sensitivity of purge flow losses to gap fraction and injection angle can be rationalized as follows. In the first place, $gf$ and $\phi$ are control parameters affecting the shear layer loss only, which is responsible for 1/2 of the purge losses. Secondly, within this already limited scope, it was shown in chapter 5 that the shear layer loss is dominated by the circumferential velocity deficit between purge and mainstream flows, rather than the axial and radial components that are determined by $\phi$ and $gf$. Results from a more extensive parametric study, using the control volume mixed-out analysis described in the same chapter, are presented in Fig. 6-4.

Fig. 6-4(a) shows almost linear scaling of shear layer loss with $mf$. It is also evident from Fig. 6-4(a) that swirling purge flow to rim speed brings down shear layer loss by 75-80%. In contrast to mass fraction and swirl velocity, Fig. 6-4(b)

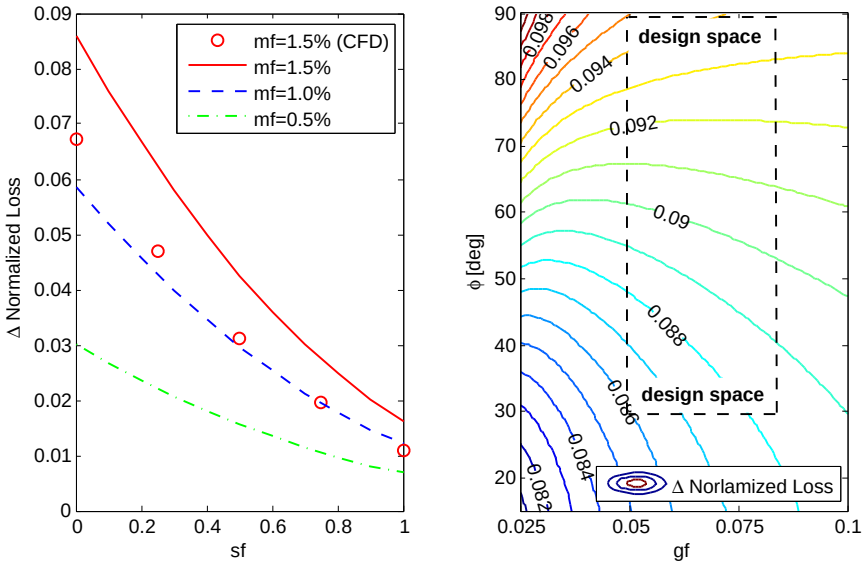


(a) Effect of $mf$ and $sf$

(b) Effect of $gf$ and $\phi$

Figure 6-4: PARAMETRIC STUDY OF SHEAR LAYER LOSS USING CONTROL VOLUME MIXED-OUT ANALYSIS

shows that gap width and injection angle are less effective in reducing shear layer loss. Within the original design space, spanning $30° < \phi < 90°$ and $5\% < gf < 8.3\%$, the contour plot of change in loss due to the shear layer associated with purge flow injection varies only by less than 10%. These results indicate that the circumferential velocity term in Eqn. (5.1) dominates shear layer loss. If we allow for some swirl to be picked up by purge air due to windage at the rotor disc, or if we intentionally design purge flow to enter the flow path with high swirl, the relative significance of the radial and axial velocity terms increases. However, in absolute terms, the effect of the radial and axial velocity deficit, and hence the design parameters $gf$ and $\phi$, never exceeds 1.5% of the baseline stage losses. Beyond this design space (particularly for very narrow purge gaps, where the purge jet axial and radial kinetic energy become more important), the effect of injection angle can also become significant. However, this would require gap widths much narrower than what is used in current practices.

As noted, CFD results suggest an even weaker dependence on $gf$ and $\phi$ ($< 6\%$ change in loss). This is most likely due to potential flow effects that act to change the effective geometry of the purge slot. Figure 6-5 shows how the blockage effect of the

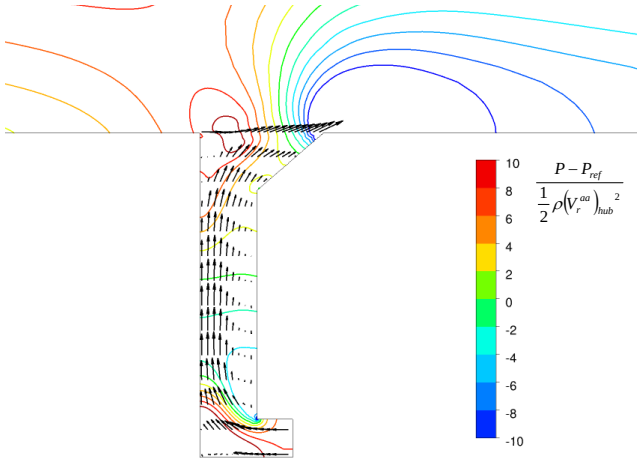


(a) Pressure field and velocity distribution in axisymmetric purge cavity

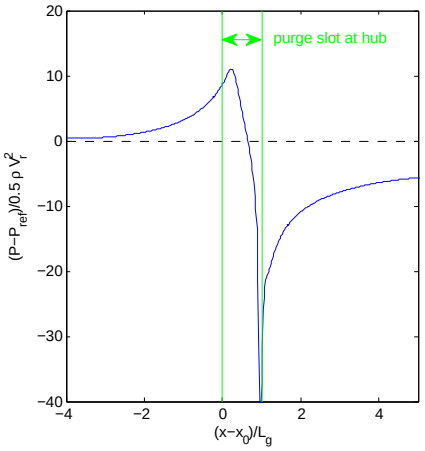


(b) Pressure at hub, demonstrating blockage effect of purge flow

Figure 6-5: EFFECT OF PURGE FLOW BLOCKAGE AND SLOT CHAMFER IN MODIFYING EFFECTIVE INJECTION ANGLE

purge flow jet increases the upstream static pressure, effectively putting a lid on the forward part of the gap. This forces the purge flow to be turned in the axial direction, even when the physical geometry is designed for radial injection ($\phi = 90°$). Note that, although chamfering appears to be an easy way to lower the injection angle, it is not necessarily good practice with respect to ingestion, as diffusion near the entrance to the mainstream flowpath makes the system susceptible to ingestion. Considerations regarding ingestion will be discussed further in Chapter 7.

## 6.2 Comparison to Published Results

Although the present study does not include assessment of computational results through experiments, there is reasonable agreement between our findings and published data in the literature. Figure 6-6 shows normalized efficiency trends with purge flow swirl and mass fraction, as compared to experimental data published in [1]. The results from the present study yield a quadratic trend of loss with swirl fraction. This is not surprising, as the shear layer loss was shown analytically to be a quadratic function of purge flow swirl velocity in Eqn. (5.1). On the other hand, the experi-

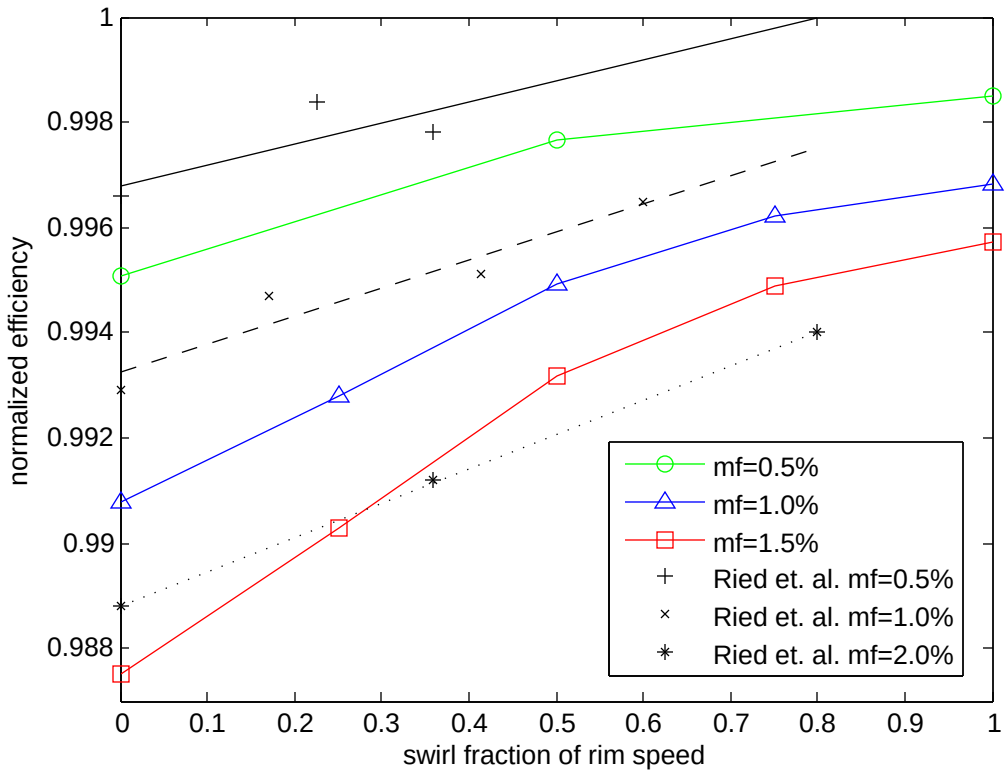


Figure 6-6: COMPARISON OF PRESENT RESULTS TO EXPERIMENTAL DATA PUBLISHED BY REID ET. AL.[1]

mental data of Reid et. al. suggests a linear trend in efficiency improvement with swirl fraction. This is likely because, in a physical scenario, purge flow tends to pick up swirl due to windage as it travels through rim seals, particularly at low swirl fractions (when the relative motion between purge flow and rotating walls is highest). At higher swirl fractions, when this phenomenon is less pronounced, the present results are in reasonable accord with the experimental results of Reid et. al.[1]. Since non-swirled purge flow is never really the case, a more realistic assessment of the potential for reducing purge flow losses through an intentional swirling device, would be the comparison of sf=30% vs. sf=100%, in which case the higher swirl reduces the purge flow losses per unit mass injected by 50%.

The present results are also in accord with the numerical investigation of Ong

[1]The measured efficiencies are slightly higher, possibly due to both a difference in seal geometry and additional swirl due to windage. In fact, it is reasonable to suspect that the experimental results under-estimate purge flow losses, since they predict that the baseline efficiency with no purge flow will be recovered at sf=80% for mf=0.5%

et.al.[4]. In that study, the authors found a 0.75%-point increase in efficiency when going from mf=0.84% sf=0% to mf=0.69 sf=110% (the mass flow was not kept constant between the swirled and non-swirled cases in that study). Of this improvement, it was estimated that 0.4%-points are due to reductions in shear layer loss, and the remaining 0.35%-points are due to reducing the negative incidence of purge flow - a similar breakdown to what was found in the present results. Interpolating from the results of the present work would give an improvement of about 0.55%-points of efficiency.

Although the numbers do not agree perfectly, the observed trends, in terms of secondary flow kinematics and loss generation, are consistent with what has been documented by other researchers. By looking at the problem in the context of entropy sources and drivers for high shear strain rate, the current work adds new insight into how loss generation in a turbine flow path comes about as a result of purge flow injection.

## 6.3 Summary of Design Guidelines

The design guidelines for reducing the loss characteristics of purge flow can be summarized as follows:

1. For every 1% purge flow, turbine stage losses increase by roughly 8%, though the relationship between $mf$ and loss is somewhat less than linear

2. Swirling purge flow prior to injection is an effective way for mitigating both shear layer and secondary flow losses. With a $sf = 100\%$, 2/3 of the purge flow losses can be recovered.

3. $gf$ and $\phi$ are not effective design parameters for mitigating loss. Their combined effect can reduce purge flow losses by 5-6% only.

4. Purge flow injected from the shroud, upstream of an unshrouded rotor, does not result in severe losses, as most of the negative impact is compensated by

suppression of tip clearance flow. Swirling shroud-injected purge flow does not result in significant additional benefit, as there is a tradeoff between purge flow losses and tip clearance flow suppression.

5. Purge flow injected upstream of the first NGV does not generate significant losses

Note that these design guidelines do not take into account sealing effectiveness. After all, the purpose of purge flow is to prevent hot gas ingestion, and it would be necessary to evaluate a given design based on the losses generated for a minimum required sealing effectiveness. In particular, it was found that pre-swirling purge flow, though an effective way to reduce losses, increases the system's susceptibility to ingestion. The next chapter will address this issue.

# Chapter 7

# Effects of Purge Flow Design on Ingestion

Chapters 5 and 6 focused on answering the question "which characteristics of purge flow are most detrimental to turbine performance, given that secondary air has to be injected into the mainstream?". It was demonstrated that swirling purge flow prior to injection was an effective way to mitigate the losses associated with injecting a given amount of purge air. However, it is important to consider how such design changes will influence the system's resistance to ingestion.

## 7.1 Effect of Purge Flow Swirl on Ingestion

With the purge slot located downstream of the mixing plane (Fig. 2-1(b)), the circumferential pressure non-uniformity, which drives externally-induced ingestion, is due to the upstream influence of the downstream rotor blades. Given the same external flow in the annulus, one would expect the same rotor upstream influence, and the same requirement for purge flow to seal a given cavity, regardless of the purge flow swirl velocity. However, Fig. 7-1 shows that, at a mass fraction of $mf = 0.5\%$, non-swilred purge flow fully seals a cavity with $gf = 5\%$, $\phi = 30°$, while the same quantity of purge flow swirled to rim speed is insufficient to prevent ingestion (negative radial velocities upstream of the rotor leading edge). This behavior implies that, unless

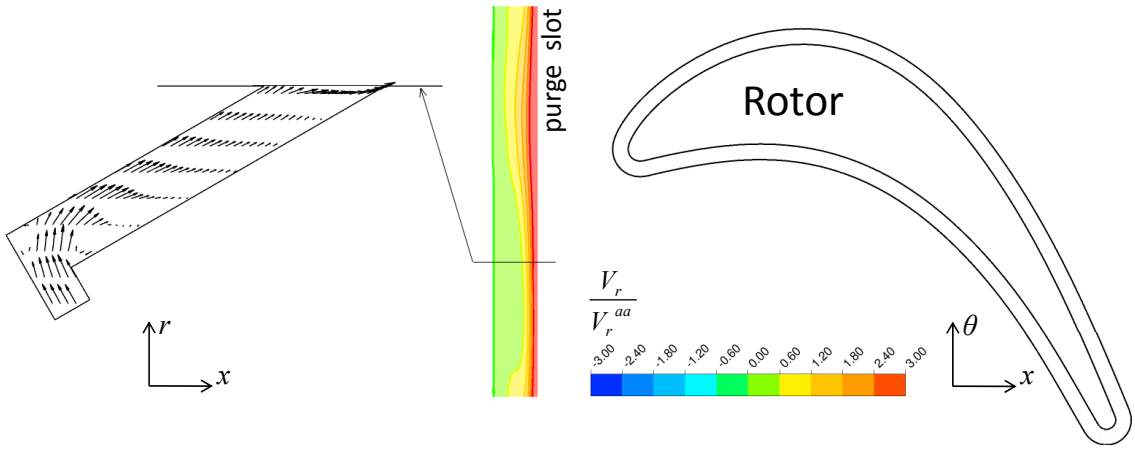


(a) $mf = 0.5\%, sf = 0\%$, cavity fully sealed

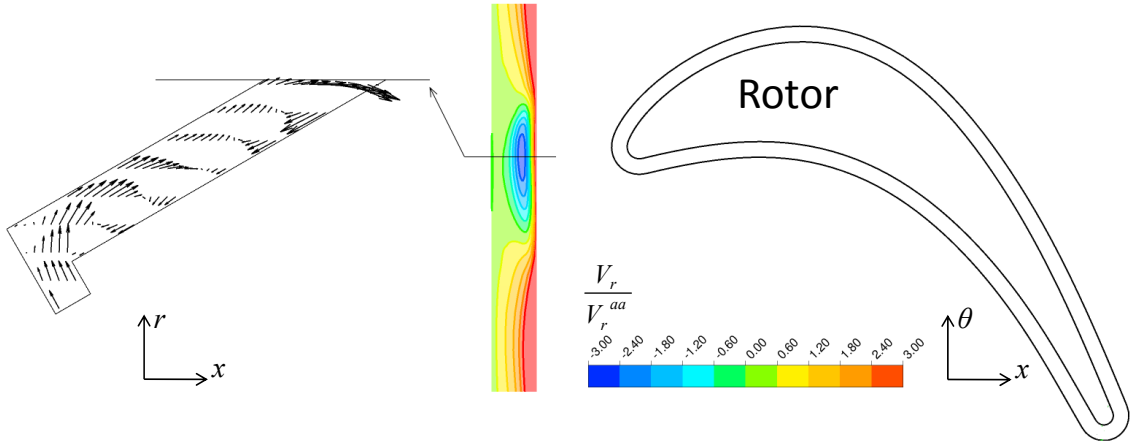


(b) $mf = 0.5\%, sf = 100\%$, ingestion occurs

Figure 7-1: BLADE-TO-BLADE VIEW, SHOWING CONTOURS OF RADIAL VELOCITY ACROSS PURGE SLOT, AND A MERIDIONAL CUT SHOWING MERIDIONAL FLOW FIELD INSIDE CAVITY.

additional measures are taken to compensate for this effect, some of the benefit of pre-swirling purge flow may be negated by the higher mass fractions required to seal the cavity.

Popovic and Hodson's [5] experimental and computational work confirms this phenomenon. They observed reduced sealing effectiveness as purge flow circumferential velocity in the relative frame was decreased (which is equivalent to increasing purge flow swirl). They argue that this can be explained by a reduction in the pressure non-uniformity associated with the rotor blade's upstream influence. This chapter

will suggest an alternative explanation.

The new hypothesis will first be presented through an analogy to a spring-mass-damper system, and justified with a time-scale argument. The ingestion phenomenon will then be modeled analytically, using a linear analysis, in order to establish scaling with relevant parameters. The linear analysis will identify reduction in $gf$ as effective means of compensating for the decreased sealing effectiveness of swirled purge flow. The analysis will also be extended to unsteady flow, with results suggesting that in unsteady flow situations, swirling purge flow would actually be beneficial, both with regard to loss and to ingestion.

## 7.2 Hypothesis

The fact that the region of ingestion in Fig. 7-1(b) occurs upstream of the rotor leading edge, indicates that the driving force is the external pressure non-uniformity associated with the rotor upstream influence. The pressure field at the hub and into the purge cavity, shown in Fig. 7-2, is steady in the relative frame. Figures 7-2(a) and 7-2(b) also show the path traced by example purge flow fluid particles emerging from the cavity, for a non-swirled and swirled case respectively. It is evident that in the relative frame of the rotor (i.e. the frame of the pressure disturbance), non-swirled purge flow takes a highly circumferential path across multiple peaks and troughs of the pressure non-uniformity, while swirled purge flow essentially tracks the rotor upstream influence. In the former case, the time-averaged effect of the pressure disturbance on non-swirled purge flow fluid particles results in a less pronounced response in velocity.

### 7.2.1 Analogy to spring-mass-damper system

The mechanisms is analogous to the situation of a spring-mass-damper harmonic oscillator, forced at a high frequency. Figure 7-3(a) shows a schematic of such a system, with a periodic force applied to it with some frequency, $f = \frac{\omega}{2\pi}$. The resulting

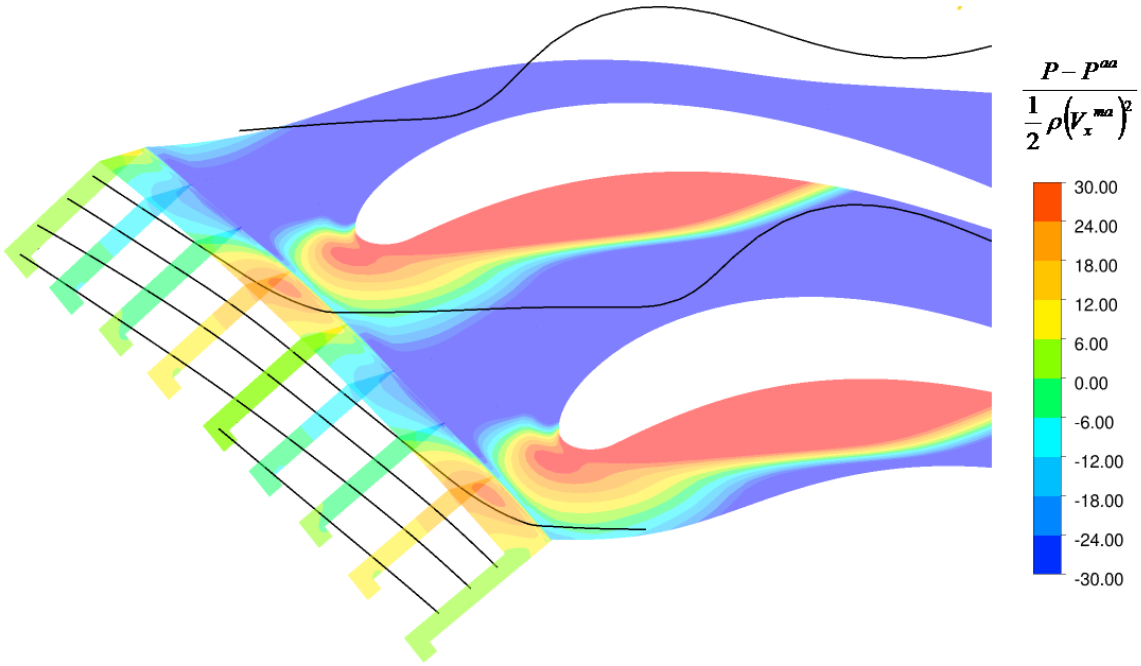


(a) $sf = 0\%$, cavity fully sealed

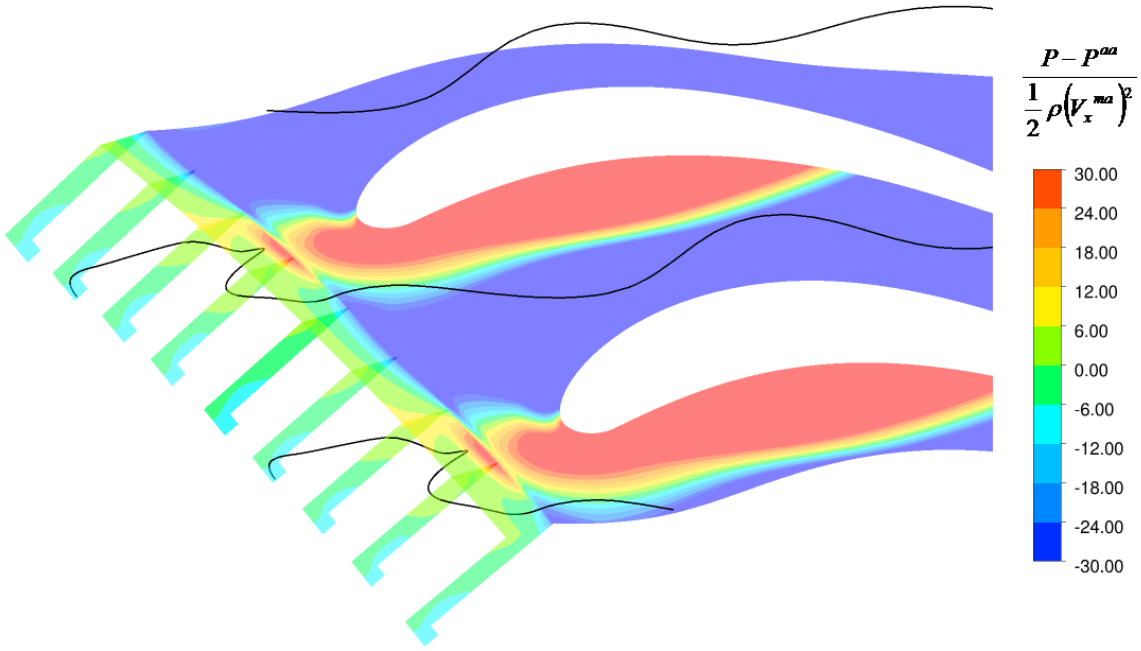


(b) $sf = 100\%$, ingestion occurs

Figure 7-2: HUB PRESSURE FIELD AND PURGE FLOW STREAMLINES IN ROTOR FRAME.

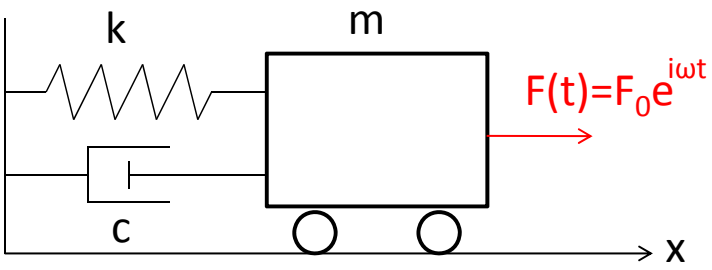


(a) Schematic of spring-mass-damper system

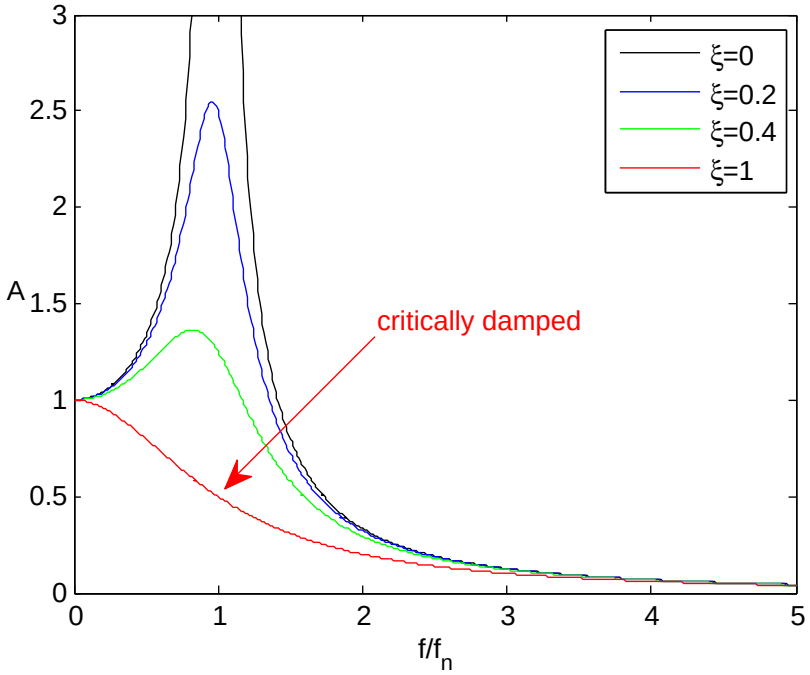


(b) Dynamic amplification factor of displacement response

Figure 7-3: HARMONIC RESPONSE OF SPRING-MASS-DAMPER SYSTEM.

periodic response in displacement will take the form of Eqn. (7.1)

$$x(t) = A\frac{F_0}{k}e^{i(\omega t-\phi)} \tag{7.1}$$

where $A$ is the dynamic amplification factor and $\phi$ is a phase shift. Figure 7-3(b) illustrates that $A$ approaches zero at high frequencies (relative to the natural frequency of the system, $f_n$). At these high frequencies, the system reacts to the time-average of the forcing term, which is zero.

In this analogy, the periodic pressure disturbance, imposed by the rotor upstream

influence, acts as a forcing function with a time-averaged value of zero. If the time scale over which the pressure disturbance acts on purge flow fluid particles in the cavity is greater than the blade passing period, the flow will react with a corresponding disturbance in velocity that is proportional to the time-averaged pressure disturbance. The next section will verify this condition.

### 7.2.2 Time-scale argument

To obtain the purge flow time scale, we must estimate the upstream influence of the pressure non-uniformity imposed on the purge flow cavity at hub radius. In order to simplify the analysis and bring out the most important effects, a Cartesian approximation of the purge slot will be used. Unwrapping the annular purge slot, and viewing it as a two dimensional duct, is a good approximation for the high hub-to-tip ratio machine we are working with. The circumferential direction will be designated as "y", and the meridional direction, defined in Fig. 7-4(b), will be designated as "x". To avoid confusion between the meridional direction in the purge slot and the axial direction in the external flow, subscript *ext* will be used when referring to the latter. This notation will be used for the remainder of this chapter.

We can describe the pressure and rotor-fame relative velocities as periodic fluctu-

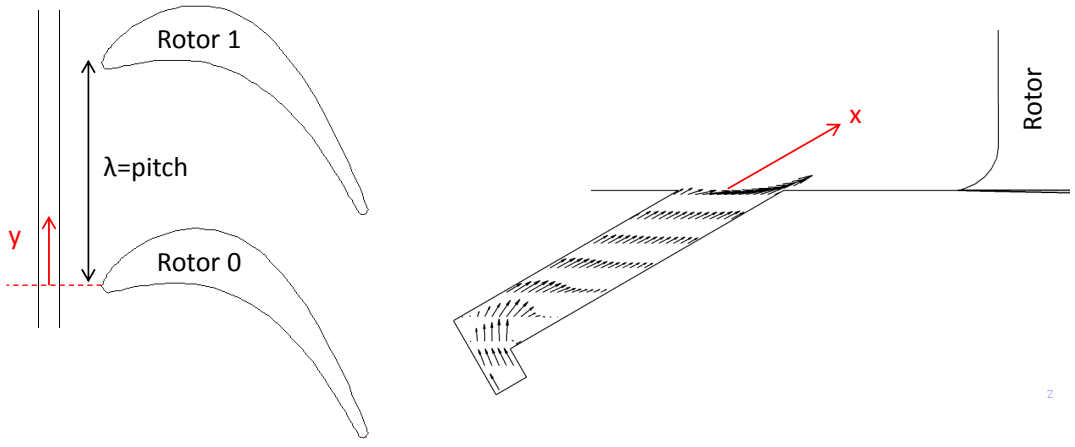


(a) blade to blade view (b) meridional view

Figure 7-4: AXIS DEFINITION FOR INVESTIGATION OF INGESTION PHENOMENON.

ations about mean values, as in Eqn. (7.2)-(7.4)

$$P(x,y) = \overline{P} + P'(x,y) \tag{7.2}$$

$$W_x(x,y) = \overline{W_x} + W'_x(x,y) \tag{7.3}$$

$$W_y(x,y) = \overline{W_y} + W'_y(x,y) \tag{7.4}$$

Under the conditions of small pressure and velocity disturbances[1], $P'$ obeys the Laplace equation[16]

$$\nabla^2 P' = 0 \tag{7.5}$$

The pressure non-uniformity at the exit of the purge slot ($x = 0$) is set by the external flow field, which imposes a periodic boundary condition of the form in Eqn. (7.6)

$$P'(0,y) = P_0 e^{i\left(\frac{2\pi}{\lambda}\right)y} \tag{7.6}$$

where $P_0$ is the amplitude of the pressure disturbance and $\lambda$ its period (in this case the rotor pitch). The resulting solution to the Laplace equation is given by Eqn. (7.7).

$$P'(x,y) = P_0 e^{\left(\frac{2\pi}{\lambda}\right)x + i\left(\frac{2\pi y}{\lambda}\right)y} \tag{7.7}$$

This result indicates that the upstream influence (x-length scale) is equal to the wavelength of the pressure disturbance (y-length scale), which in this case is the blade pitch, $\lambda$. Therfore, using blade pitch as a length scale, and average meridional velocity, $\overline{W}_x = \frac{\dot{m}_b}{\rho(2\pi r d_g)}$, the purge flow time scale can be calculated. Equation (7.8) shows that the purge flow time scale is approximately 20 times larger than the blade passing period

[1]In this context, "small" means that $W'_x \ll \overline{W}_x$, $W'_x \ll \overline{W}_y$ and $P' \ll \frac{1}{2}\rho\overline{W}_x^2$. These conditions are not met in the current configuration, but asymptotic analysis arguments can be used to derive conclusions about the current system based on the behavior of a system that does satisfy the small perturbation conditions. It will be shown that these conclusions compare well to CFD results even when the small perturbation conditions are not rigorously satisfied

$$\frac{purge\ flow\ time\ scale}{blade\ passing\ period} = \frac{\frac{\lambda}{\overline{W}_x}}{\frac{\lambda}{\Omega r_{hub}}} = \frac{\Omega r_{hub}}{\overline{W}_x} \approx 20 \tag{7.8}$$

Two conclusions can be drawn from Eqn. (7.8). Firstly, multiple blade passing events can occur in the time it takes for a non-swirled purge flow particle to move through the pressure disturbance, resulting in an averaging effect. Secondly, the blade pitch factors out of the time scale ratio, indicating that the blade count of the rotor does *not* affect this ingestion phenomenon. To gain insight into the parameters that *do* affect ingestion, and to specifically identify those that can be used to mitigate this undesirable effect, the remainder of this chapter will develop a linear model for the response of purge flow in the presence of a periodic pressure disturbance.

## 7.3 Linear Analysis of Ingestion

This section will first solve linearlized x- and y-momentum equations, given the assumed pressure field in Eqn. (7.7). This will allow for transfer functions, relating $W'_x$ and $W'_y$ to $P'$, to be cast in terms of purge flow design parameters. The behavior of these transfer functions will be assessed against computed CFD results, and then used to arrive at a criterion for ingestion. The analysis will also be extended to unsteady flow situations, where the pressure disturbance is set by NGV-rotor interaction.

### 7.3.1 Linear analysis transfer functions

To begin, we express the x-momentum equation in terms of the mean and perturbation quantities of Eqn. (7.2)-(7.4)

$$\left(\overline{W}_x + W'_x\right)\frac{\partial\left(\overline{W}_x + W'_x\right)}{\partial x} + \left(\overline{W}_y + W'_y\right)\frac{\partial\left(\overline{W}_x + W'_x\right)}{\partial y} = -\frac{1}{\rho}\frac{\partial\left(\overline{P} + P'\right)}{\partial x} \tag{7.9}$$

Assuming small perturbations in velocity and pressure, we can linearize about the average quantities, yielding Eqn. (7.10)

$$\overline{W}_x \frac{\partial W'_x}{\partial x} + \overline{W}_y \frac{\partial W'_x}{\partial y} = -\frac{1}{\rho}\frac{\partial P'}{\partial x} \tag{7.10}$$

The right-hand-side forcing term can be calculated from the expression for $P'$ given in Eqn. (7.7), resulting in Eqn. (7.11)

$$\overline{W}_x \frac{\partial W'_x}{\partial x} + \overline{W}_y \frac{\partial W'_x}{\partial y} = -\frac{1}{\rho}\frac{2\pi}{\lambda} P_0 e^{\left(\frac{2\pi}{\lambda}\right)x + i\left(\frac{2\pi}{\lambda}\right)y} \tag{7.11}$$

Realizing that the particular solution to this inhomogeneous partial differential equation will take the form $W'_x = \tilde{X} e^{\left(\frac{2\pi}{\lambda}\right)x + i\left(\frac{2\pi}{\lambda}\right)y}$, we can substitute into Eqn. (7.11) and solve for $\tilde{X}$

$$\tilde{X} = \left(\frac{-P_0}{\rho \overline{W}_x}\right) \frac{1}{1 + i\frac{\overline{W}_y}{\overline{W}_x}} \tag{7.12}$$

The same procedure can be undertaken with the y-momentum equation, yielding a solution of the form $W'_y = \tilde{Y} e^{\left(\frac{2\pi}{\lambda}\right)x + i\left(\frac{2\pi}{\lambda}\right)y}$, where $\tilde{Y}$ is given in Eqn. (7.13)

$$\tilde{Y} = \left(\frac{P_0}{\rho \overline{W}_x}\right) \frac{-i}{1 + i\frac{\overline{W}_y}{\overline{W}_x}} \tag{7.13}$$

Having obtained explicit solutions to the linearized momentum equations, transfer functions can be defined between non-dimensional quantities that characterize the response of purge flow. The primary quantity of interest is the ratio $\frac{-W'_x}{\overline{W}_x}$. As this ratio approaches unity, the system approaches a state of localized ingestion. The non-uniformity in the y-direction can also be quantified by the ratio $\frac{W'_y}{\overline{W}_x}$. Although this latter quantity does not reflect the degree of ingestion directly, it will be presented here for a an additional consistency check between the linearized analysis and CFD results. These two ratios, $\frac{-W'_x}{\overline{W}_x}$ and $\frac{W'_y}{\overline{W}_x}$, will be the outputs of the transfer functions. Because the ingestion mechanism we are dealing with is pressure driven, the relevant input to the transfer functions is $\frac{P'}{\rho \overline{W}_x^2}$. The transfer functions, defined in Eqn. (7.14)

and Eqn. (7.15), are put in the form of an amplification factor ($A$) and phase angle ($\phi$).

$$H_x = \frac{\left(\frac{-W'_x}{\overline{W}_x}\right)}{\left(\frac{P'}{\rho \overline{W}_x^2}\right)} = \underbrace{\frac{1}{\sqrt{1+\left(\frac{\overline{W}_y}{\overline{W}_x}\right)^2}}}_{A} \; e^{i\overbrace{\left(-atan\frac{\overline{W}_y}{\overline{W}_x}\right)}^{\phi}} \tag{7.14}$$

$$H_y = \frac{\left(\frac{W'_y}{\overline{W}_x}\right)}{\left(\frac{P'}{\rho \overline{W}_x^2}\right)} = \underbrace{\frac{1}{\sqrt{1+\left(\frac{\overline{W}_y}{\overline{W}_x}\right)^2}}}_{A} \; e^{i\overbrace{\left(-\frac{\pi}{2}-atan\frac{\overline{W}_y}{\overline{W}_x}\right)}^{\phi}} \tag{7.15}$$

It is clear that Eqn. (7.14) and Eqn. (7.15) are fundamentally functions of the ratio $\frac{\overline{W}_y}{\overline{W}_x}$, which is in essence the effective time scale ratio presented in Eqn. (7.8). This ratio can be expressed in terms of the purge flow design parameters $mf$, $sf$, $gf$ and a constant, $K$, that is a function of the turbine stage design, i.e.

$$\frac{\overline{W}_y}{\overline{W}_x} = (sf-1)\left(\frac{gf}{mf}\right)\underbrace{\left[\frac{4\left(\frac{\rho_b}{\rho_a}\right)}{\left(\frac{\overline{W}_{x,a}}{\Omega r_{mean}}\right)\left(\frac{r_{tip}}{r_{hub}}+1\right)^2}\right]}_{K} \tag{7.16}$$

The final and most useful form of the transfer functions defined in Eqn. (7.14) and Eqn. (7.15), is thus given by Eqn. (7.17) and Eqn. (7.18).

$$H_x = \underbrace{\frac{1}{\sqrt{1+(sf-1)^2\left(\frac{gf}{mf}\right)^2 K^2}}}_{A} \; e^{i\overbrace{\left\{-atan\left[(1-sf)\left(\frac{gf}{mf}\right)K\right]\right\}}^{\phi}} \tag{7.17}$$

$$H_y = \underbrace{\frac{1}{\sqrt{1+(sf-1)^2\left(\frac{gf}{mf}\right)^2 K^2}}}_{A} \; e^{i\overbrace{\left\{-\frac{\pi}{2}-atan\left[(1-sf)\left(\frac{gf}{mf}\right)K\right]\right\}}^{\phi}} \tag{7.18}$$

To get a sense of how these transfer functions behave, Fig. 7-5(a) and Fig. 7-5(b) illustrate the amplification factors and phase angles of $H_x$ and $H_y$ as a function of swirl fraction. The gap fraction is held fixed at $gf = 5\%$ and scenarios for three different mass fractions are shown. The amplification factors in Fig. 7-5 show peak amplitudes in $W'_x$ and $W'_y$ at $sf = 100\%$, indicating that ingestion is most likely to occur. The phase angle, $\phi$, indicates that the peaks and troughs in $W'_x$ are circumferentially aligned with those of the pressure non-uniformity, while the peaks and troughs in $W'_y$ lead by $\frac{1}{4}$ period. At $sf = 0\%$, and at swirl fractions exceeding rim speed, the time-averaged pressure disturbance elicits a diminished response from velocity, in an analogous manner to a spring-mass oscillator that is being forced at a high frequency (Note the similarity of the amplification factor to that of the critically damped spring-mass-damper in Fig. 7-3(b)). At low swirl fractions, the phase of both $W'_x$ and $W'_y$ is shifted back by $\frac{1}{4}$ period. At higher mass fractions (or lower gap fractions), the averaging effect is weaker, as purge flow has a higher meridional velocitiy and experiences fewer blade passage events as it moved through the pressure disturbance.

To assess the behavior of these transfer functions against CFD results, Fig. 7-6 and Fig. 7-7 present the computed circumferential variation in $P'$, $W'_x$ and $W'_y$, from representative locations inside the purge cavity[2]. The two figures show results from two mass flow rates, $mf = 1.5\%$ and $mf = 0.5\%$ respectively, and a case with and without swirl is given for each mass flow rate.

At $mf = 1.5\%$ (Fig. 7-6), the assumption of small velocity perturbations is satisfied. Comparing Fig. 7-6(a) with Fig. 7-6(b) we observe reduced perturbations in velocity for the case with no swirl, and a shift in the circumferential location of peaks

[2]The representative locations are approximately 0.2 - 0.6 purge slot gap widths into the purge cavity, where the results are less obscured by shearing from the mainstream flow

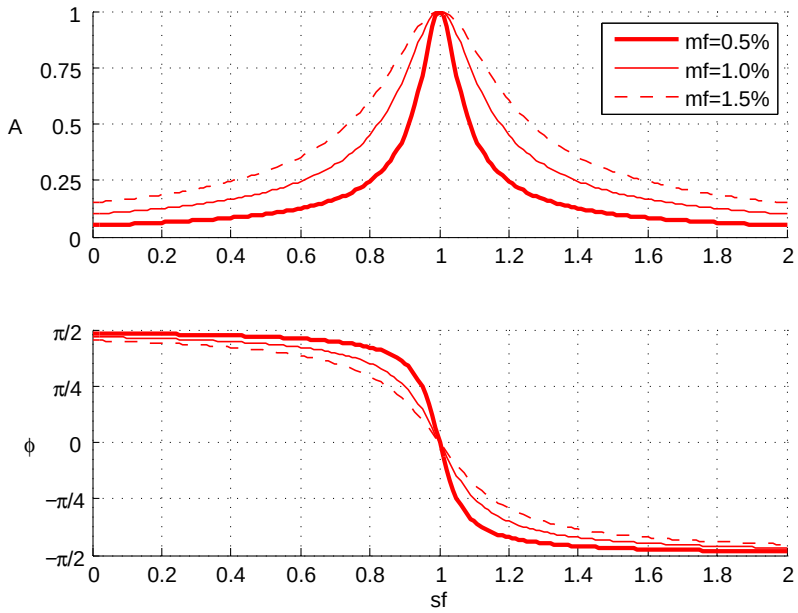


(a) Amplification factor and phase for transfer function $H_x$

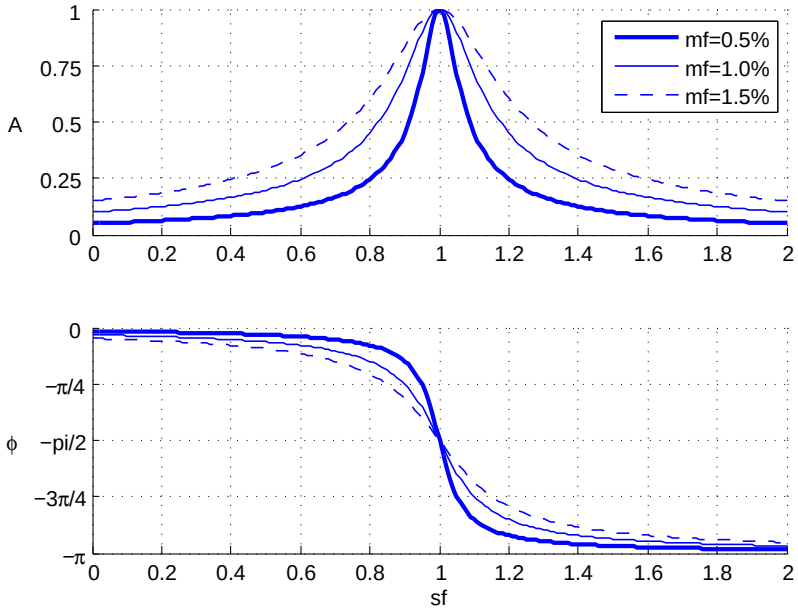


(b) Amplification factor and phase for transfer function $H_y$

Figure 7-5: AMPLIFICATION FACTORS AND PHASE OF TRANSFER FUNCTIONS.

and troughs of $W_x'$ and $W_y'$ (the arrows make it easier to see the phase relationship between the quantities in each subplot. Note the negative sign in $\frac{-W_x'}{\overline{W}_x}$ means that phase is measured from peak of $P'$ to trough of $W_x'$). Both of these features are in agreement with the predictions of the linear analysis. At the lower purge mass flow

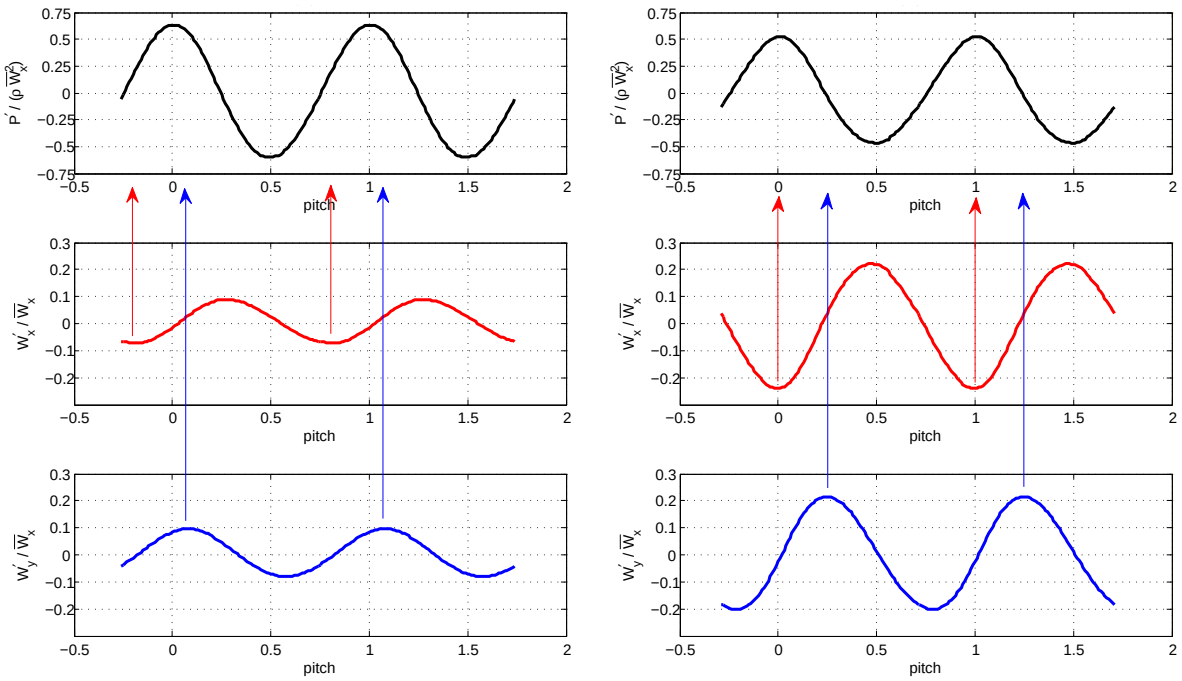


(a) No swirl (b) Rim speed swirl

Figure 7-6: PRESSURE AND VELOCITY NON-UNIFORMITIES, AT REPRESENTATIVE RADIAL LOCATIONS IN PURGE CAVITY, FOR $mf = 1.5\%$. CAVITY IS FULLY SEALED AND ALL QUANTITIES ARE AVERAGED ACROSS THE AXIAL EXTENT OF THE PURGE GAP.

rate (Fig. 7-7), where ingestion occurs and therfore the assumptions of the linear analysis are not strictly satisfied, the trends observed in CFD results are still in good agreement with those of the linear analysis (Note that for the case of $sf = 100\%$ there are two peaks in $W'_y$: one corresponds to swirl induced by the pressure disturbance and the other reflects the ingestion of highly swirled mainstream flow).

### 7.3.2 Criterion for ingestion based on linear analysis

Qualitative agreement in response amplitude and phase, between the linear analysis and CFD, suggests that we have arrived at the correct explanation for increased susceptibility to ingestion for swirled purge flow. However, we can take the linear analysis a step further and define a criterion for ingestion. This will give a first order estimate of the purge air mass fraction required to seal a given cavity, without the need for elaborate CFD calculations.

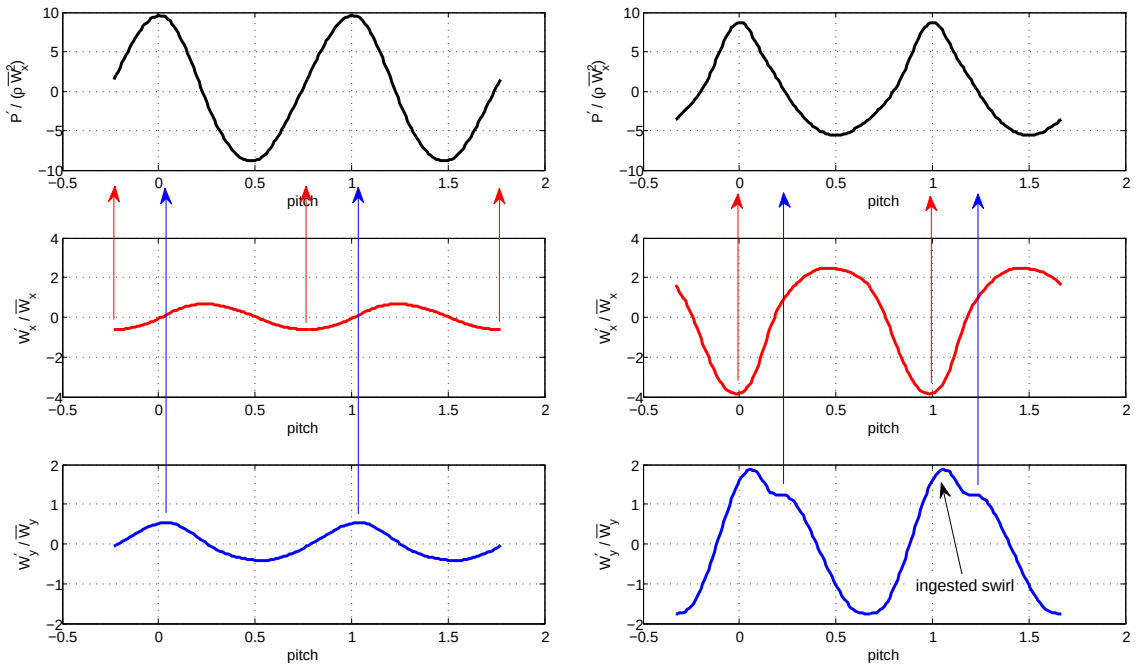


(a) no swirl (b) rim speed swirl

Figure 7-7: PRESSURE AND VELOCITY NON-UNIFORMITIES, AT REPRESENTATIVE RADIAL LOCATIONS IN PURGE CAVITY, FOR $mf = 0.5\%$. INGESTION OCCURS FOR THE CASE OF $sf = 100\%$ AND ALL QUANTITIES ARE TAKEN NEAR THE DOWNSTREAM EDGE OF THE SLOT, ACROSS THE REGION OF INGESTION.

The criterion for ingestion is that the ratio of disturbance to mean meridional velocity is greater than unity, i.e.

$$\frac{-W'_x}{\overline{W_x}} \geq 1 \tag{7.19}$$

This ratio can be obtained using the transfer function defined in Eq. (7.14), given the pressure disturbance at the purge slot exit as an input. To begin, we assume that the pressure disturbance is imposed on the purge slot exit by the external flow. The amplitude of the pressure non-uniformity at the rotor leading edge plane can be approximated by the mainstream dynamic head. The upstream influence of that non-uniformity satisfies the Laplace Equation, resulting in the exponential decay shown in Fig. 7-8. This providing an estimate of $P_0$ - the pressure disturbance amplitude at the purge slot exit. Applying the transfer function from $\frac{P'}{\rho \overline{W}'_x}$ to $\frac{-W'_x}{\overline{W_x}}$ for a range of

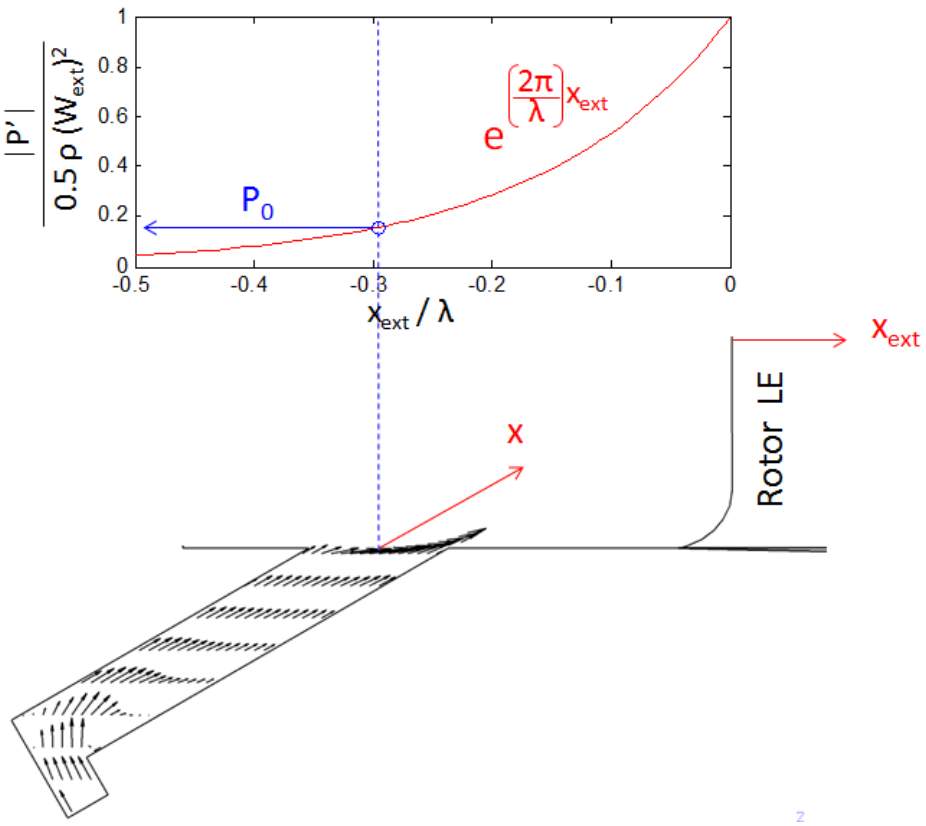


Figure 7-8: METHOD FOR ESTIMATING AMPLITUDE OF ROTOR UPSTREAM INFLUENCE AT PURGE SLOT.

$mf$ and $sf$, holding the purge gap geometry fixed at either $gf = 5\%$ or $gf = 2.5\%$, results in the contours in Fig. 7-9.

As mentioned earlier, $\frac{-W'_x}{\overline{W_x}} \geq 1$ indicates a state of ingestion. Figure 7-9 shows that swirling purge flow to $sf = 50\%$ increases the purge flow required to seal the cavity by a factor of two, and $sf = 100\%$ increases it by a factor of 5. (Note that the contours in Fig. 7-9 are symmetric about $sf = 100\%$.) The benefit of swirling purge flow to reduce losses is quickly offset by the higher purge flow requirement. However, comparing the case of $gf = 5\%$ against $gf = 2.5\%$ shows that decreasing the gap width is an effective way to improve sealing effectiveness.

Because reducing gap width does not affect the loss characteristics of purge flow (as was established in chapter 6), one can minimize losses by increasing $sf$, and compensating for decreased sealing effectiveness by reducing $gf$. However, it is worth considering the alternative strategy of reducing $gf$ in order to minimize purge flow

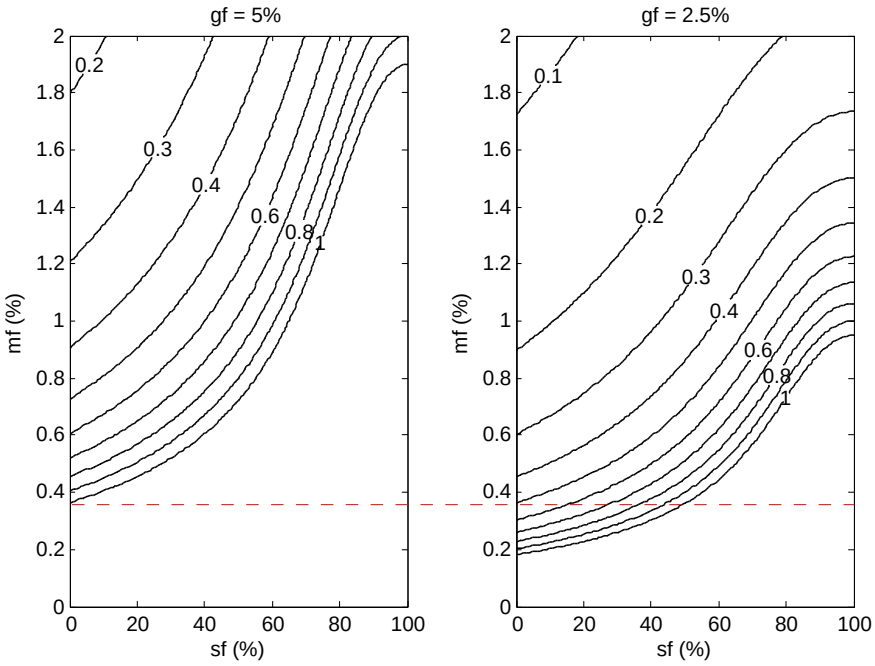


Figure 7-9: CONTOURS OF $\frac{-W'_x}{\overline{W}_x}$, BASED ON LINEAR ANALYSIS WITH PRESSURE DISTURBANCE ESTIMATED FROM FIRST PRINCIPLES.

requirement, which would in turn reduce purge flow losses directly. Both strategies require a reduction in gap width, a parameter that may be constrained by manufacturing and operational considerations. In order to accurately compare the cost of these two strategies, it is important that the criterion for ingestion is quantitatively precise.

### 7.3.3 Criterion for ingestion vs. CFD results

In the previous subsection, a criterion for ingestion was derived entirely from first principles. To assess this result, Fig. 7-10(a) includes data points from CFD that delineate the $\frac{-W'_x}{\overline{W}_x} = 1$ limit. The agreement of the analytical and computational results is good, with the exception that the peak purge flow requirement based on CFD is lower and does not occur at $sf = 100\%$. This is because the pressure disturbance cannot be considered to be entirely imposed by the external flow, and is in fact a function of purge flow parameters.

The expression for the two dimensional pressure field in the cavity, given earlier

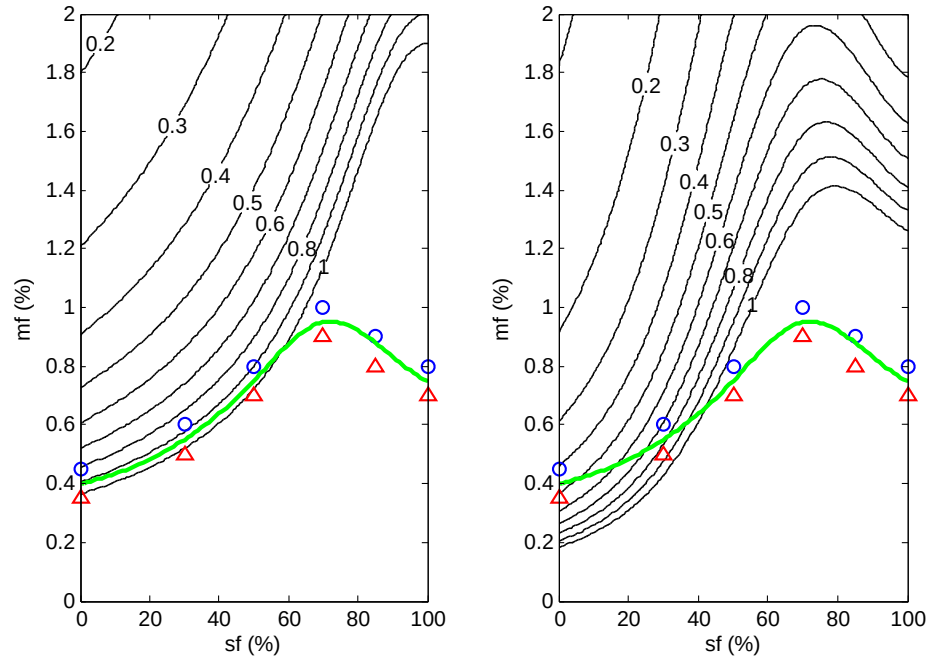


(a) pressure field from first principles (b) pressure fields from CFD

Figure 7-10: CONTOURS OF $\frac{-W'_x}{\overline{W}_x}$ BASED ON LINEAR MODEL COMPARED TO INGESTION LIMIT BASED ON CFD.

in Eqn. (7.7), can be generalized in Eqn. (7.20)

$$P'(x,y) = P_0 e^{\left(\frac{2\pi}{L}\right)x + i\left(\frac{2\pi}{\lambda}\right)y} \tag{7.20}$$

where the amplitude of the pressure disturbance at $x = 0$ is not necessarily a constant independent of purge flow parameters, and the upstream decay rate length scale, $L$, is not necessarily equal to the blade pitch[3]. Figure 7-11 shows the pressure disturbance amplitude as a function of meridional distance into the cavity, for three different values of $sf$. Both gap-averaged and peak amplitudes are given. An exponential curve is fitted to the gap-averaged data, and decay length scale is given as a ratio to the blade pitch. It is clear that both $P_0$ and $L$ are dependent on purge flow swirl. Figure 7-12 gives further details on how $P_0$ and $L$ scale with swirl and mass fraction. The constant values of $P_0$ and $L$ derived from first principles, and used to

[3]Note that the deviation of $L$ from from the y-length scale, $\lambda$, means that $W'_x$ and $W'_y$ do not satisfy continuity. However this is not unreasonable, since the linear analysis is two dimensional and does not take into account flow perpendicular to the meridional direction.

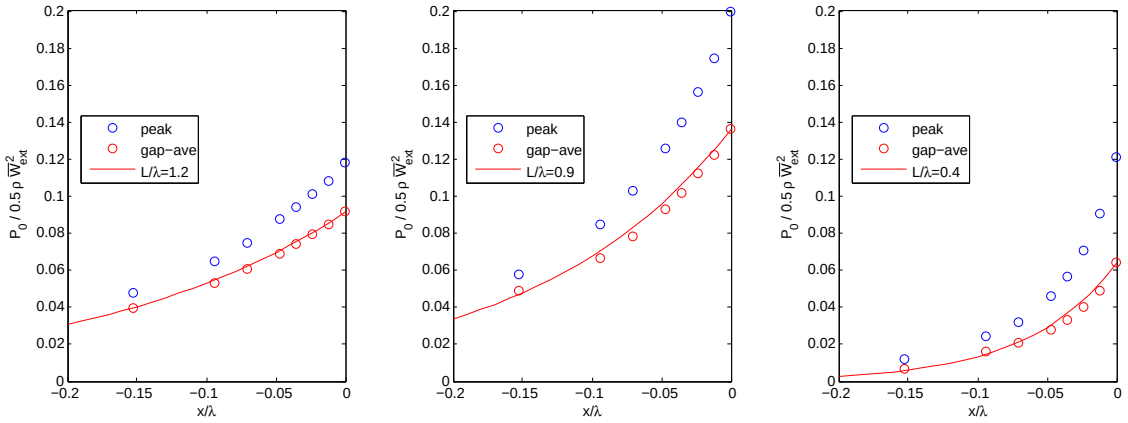


(a) sf=0% (b) sf=50% (c) sf=100%

Figure 7-11: DECAY OF PRESSURE DISTURBANCE AMPLITUDE AS A FUNCTION OF MERIDIONAL DISTANCE INTO THE CAVITY, $mf = 1\%$.

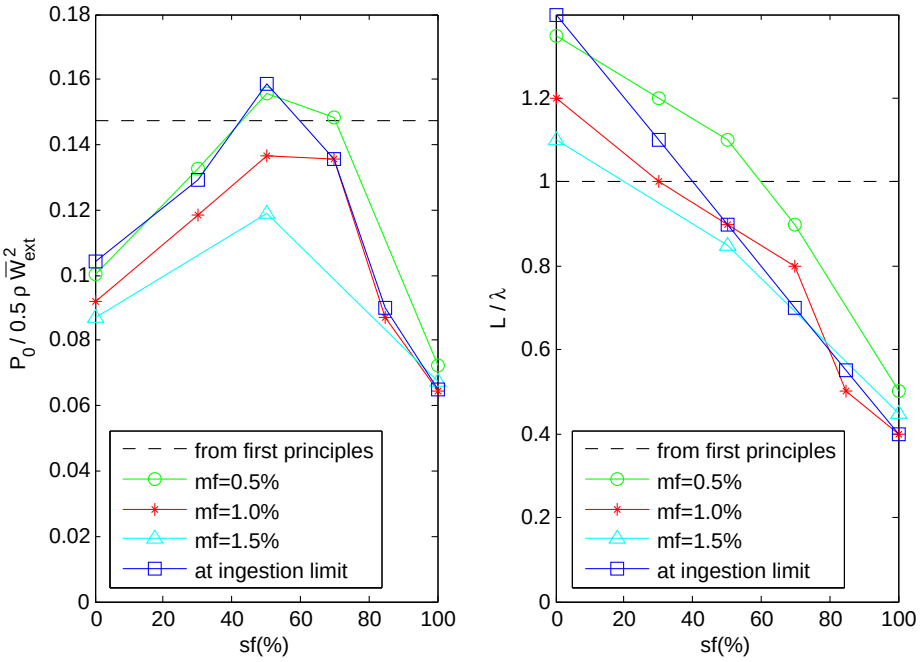


Figure 7-12: CHARACTERISTICS OF PRESSURE FIELDS IN CAVITY OBTAINED FROM CFD, SHOWING $P_0$ AND $L/\lambda$ AS A FUNCTION OF PURGE FLOW SWIRL.

generate Fig. 7-9, are also given for reference. As purge flow swirl is increased, the disturbance amplitude exhibits non-monotonic behavior, with peak values occurring at $sf \approx 50 - 70\%$, while the decay length scale decreases almost linearly. A physical explanation for this behavior has yet to be formulated.

If the pressure field obtained from CFD is used as an input to the linear analysis transfer functions, with $P_0$ and $L$ allowed to vary with swirl according to a curve fit of the data points in Fig. 7-12 that lie on the ingestion limit, the resulting criterion for ingestion is given in Fig. 7-10(b). There is now excellent agreement between the location of peak ingestion susceptibility. If an efficient way for predicting the behavior of $P_0$ and $L$ can be developed, the linear analysis results can become a good preliminary design tool for estimating ingestion susceptibility.

### 7.3.4 Criterion for ingestion for unsteady flow

The linear analysis can be extended to unsteady situations, in which the pressure disturbance at the purge slot exit is imposed by both NGV and rotor. Under the linear assumptions of the analysis, the two contributions are additive, resulting in the cumulative rotor-frame pressure field given in Eqn. (7.21)

$$P'(x,y) = \underbrace{P_{R0}e^{\left(\frac{2\pi}{\lambda_R}\right)x+i\left(\frac{2\pi}{\lambda_R}\right)y}}_{P'_R(x,y)} + \underbrace{P_{V0}e^{\left(\frac{2\pi}{\lambda_V}\right)x+i\left(\frac{2\pi}{\lambda_V}\right)y+i\left(\frac{2\pi\Omega_V r_{hub}}{\lambda_V}\right)t}}_{P'_V(x,y)} \tag{7.21}$$

where $P_{R0}$ and $P_{V0}$ are the amplitudes of the pressure disturbances imposed on the purge slot exit by the rotor and vane respectively, $\lambda_R$ and $\lambda_V$ are the rotor and vane pitches, and $\Omega_V$ is the angular speed of the vane in the rotating frame. The pressure disturbance is expressed in the rotating frame, making the vane contribution an unsteady one. In the absence of a more precise estimate of the pressure disturbances, we will use constant values for $P_{R0}$ and $P_{V0}$, and assumed an upstream influence (into the cavity) with length scale equal to the pressure disturbance's y-length scale (i.e. $\lambda_R$, and $\lambda_V$). As a first approximation, we will take $P_{R0} = P_{V0} = P_0$, where $P_0$ is the rotor upstream influence at the location of the purge slot, obtained by the procedure illustrated in Fig. 7-8.

Linearizing the unsteady momentum equation leads to Eqn. (7.22),

$$\frac{\partial W'_x}{\partial t} + \overline{W}_x\frac{\partial W'_x}{\partial x} + \overline{W}_y\frac{\partial W'_x}{\partial y} = -\frac{1}{\rho}\frac{\partial P'_R}{\partial x} - \frac{1}{\rho}\frac{\partial P'_V}{\partial x} \tag{7.22}$$

Because the two terms on the right-hand-side, pertaining to $P'_R$ and $P'_V$ respectively, are linearly independent, it is possible to obtain a solution to this differential equation using superposition. Finding solutions that will independently satisfy each of the two right-hand-side terms, and using superposition results in Eqn. (7.23)

$$W'_x = \left(\frac{P'_R}{\rho \overline{W}_x}\right) \frac{-1}{1 + i\frac{\overline{W}_y}{\overline{W}_x}} + \left(\frac{P'_V}{\rho \overline{W}_x}\right) \frac{-1}{1 + i\left(\frac{\overline{W}_y}{\overline{W}_x} - \frac{\Omega_V r_{hub}}{\overline{W}_x}\right)} \tag{7.23}$$

This time-dependent perturbation in $W'_x$ is illustrated for the case of $mf = 2\%$, $sf = 50\%$ in Fig. 7-13. The spacial coordinate in this surface plot is normalized by rotor pitch, and the temporal coordinate by the blade passing period, $\frac{\lambda_R}{\Omega r_{hub}}$. For a closer look, we can take temporal slices of this plot at regular intervals, as in Fig. 7-14. The corresponding pressure disturbance at these instances is also shown for reference.

Taking the maximum response over a given period of time, as illustrated in Fig. 7-14, provides us with the criterion for ingestion in unsteady conditions. The result is given in Fig. 7-15(b) and compared to the steady situation presented earlier, in which there is only a pressure disturbance due to the rotor upstream influence (Fig. 7-15(a)).

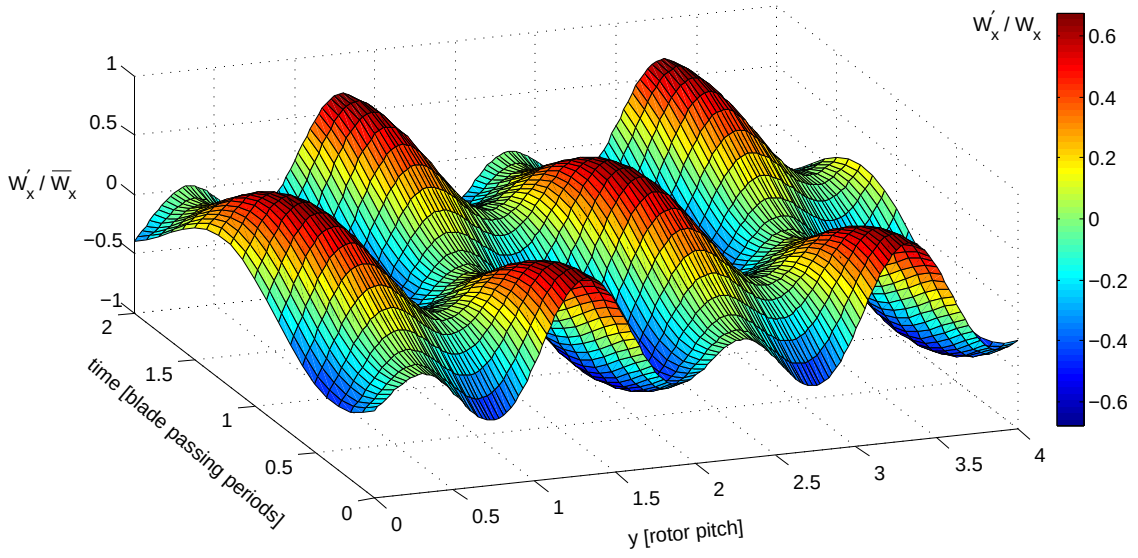


Figure 7-13: SURFACE PLOT OF UNSTEADY $\frac{W'_x}{\overline{W}_x}$ AS A FUNCTION OF SPACE AND TIME.

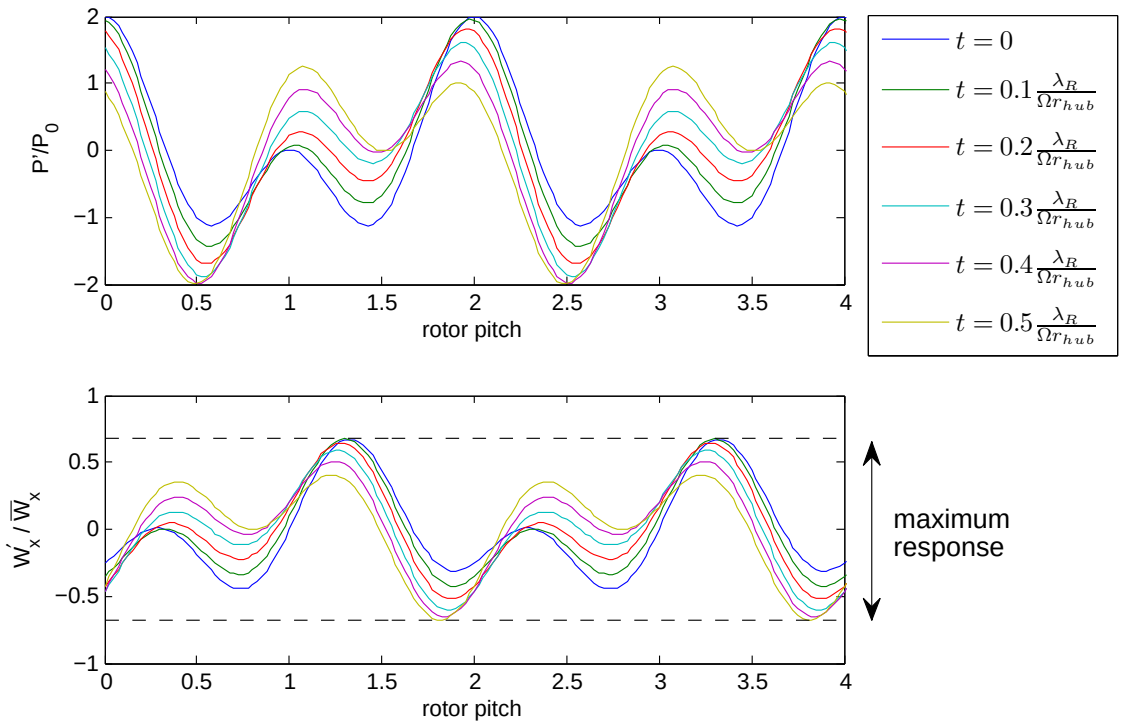


Figure 7-14: INSTANTANEOUS DISTURBANCE IN UNSTEADY $P'$, AND CORRESPONDING RESPONSE IN $W_x'$.

The unsteady result now exhibits two peaks in susceptibility to ingestion - one at rim speed swirl and one at no swirl. This is because at rim speed swirl purge flow tracks the rotor pressure disturbance, while at zero swirl it locks into the NGV pressure disturbance. Because we arbitrarily chose the same amplitude for both disturbances, the two peaks are of equal height. Note that the difference in blade to vane pitch has no impact on the result. This is because the upstream influence, and the blade passing time, scale with pitch in the same way, therefore blade pitch drops out of the analysis (recall Eqn. (7.8)).

In general, the NGV and rotor pressure disturbances are not of the same amplitude, with $P_{V0} > P_{R0}$ being the usual case[4]. Figure 7-15(c) shows how the ingestion criterion is modified when $P_{V0} = 2P_0$. Under these conditions, swirling purge flow is actually beneficial, not only for reducing purge flow losses, but also for improving sealing effectiveness and reducing purge flow requirement.

[4]Personal correspondence with Dr. David Little, Siemens Energy

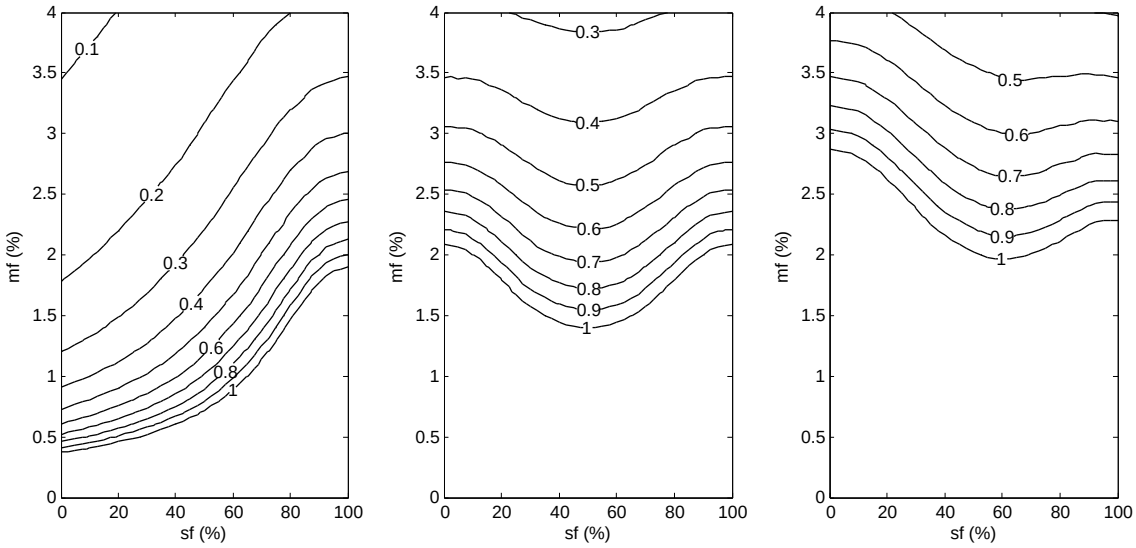


(a) $P_{V0} = 0, P_{R0} = P_0$ (steady) (b) $P_{V0} = P_{R0} = P_0$ (c) $P_{V0} = 2P_0, P_{R0} = P_0$

Figure 7-15: CONTOURS OF $\frac{-W'_x}{\overline{W}_x}$ UNDER STEADY AND UNSTEADY CONDITIONS.

## 7.4 Summary of Ingestion due to Swirl

It was found that, under the conditions of circumferentially non-uniform static pressure due to the rotor blades' upstream influence, higher mass fractions of purge air are required to seal the same cavity if purge flow is swirled. This is because, for non-swirled purge flow, relative motion of purge flow with respect to the rotor-synchronized pressure non-uniformity results in an averaging effect, analogous to that experienced by a spring-mass-damper system forced at a high frequency. This beneficial averaging effect is reduced as purge flow swirl approaches rim speed and locks step with the pressure non-uniformity. Time scale estimates and a linear analysis confirmed this hypothesis. A parametric study, based on the transfer functions obtained through the linear analysis, suggests that reducing gap width is a plausible way to improve sealing effectiveness without compromising efficiency. This leads to the proposition of two strategies for addressing purge flow losses: (i) improve purge flow loss characteristics by increasing $sf$ and compensate for reduced sealing effectiveness by reducing $gf$, or (ii) reduce $gf$ in order to minimize purge flow requirement, which will in turn reduce purge flow losses directly

However, in representative turbomachines, ingestion is driven by an unsteady pressure disturbance that is usually dominated by the pressure non-uniformity introduced by the NGV. Under these conditions, swirling purge flow is actually beneficial, both for reducing purge flow losses and for improving sealing effectiveness.

Further work needs to be done to assess the linear analysis results for unsteady flow against CFD or experiments. There is also a need to formulate an explanation for the reduced upstream influence, and the non-monotonic scaling of pressure disturbance amplitude, as a function of purge flow swirl.

# Chapter 8

# Unsteady Effects on Purge Flow Loss

The results presented in chapters 4-6 are based on an investigation of purge flow injection into a *steady* turbine mainstream flow. The inherent unsteadiness in turbomachinery was factored out through the use of a mixing plane downstream of the NGV. The logical next step would thus be to determine the effect of flow unsteadiness on purge flow losses. Likewise, the results from the linear analysis of ingestion, in the presence of unsteady NGV-rotor interaction, must also be assessed against unsteady computations.

This chapter will formulate guidelines for investigating unsteady effects on loss. Two approaches for determining time-average loss in unsteady flow will be developed. These will be applied to unsteady computational results, providing a preliminary assessment of flow unsteadiness on purge flow-induced losses. The unsteady results are from a turbine stage of a different design[1], and are presented here as a prelude to future work.

[1]These results are from an earlier study on purge flow sealing effectiveness, done at the University of Bath

## 8.1 First Approach for Determining Loss in Unsteady Flow: Appropriate Averaging of Entropy

In unsteady flow situations, one is generally interested in time-averaged effects. In addition, dealing with flow non-uniformity requires appropriate spacial averaging as well. This section will present the appropriate combination of spacial and temporal averaging of entropy, for the purpose of determining turbine losses in situations where thermal mixing is negligible.

### 8.1.1 Appropriate averaging of entropy for unsteady flow

As noted in chapter 3, only entropy generated due to viscous effects is relevant to turbine performance. However, in the absence of secondary air steams, the entropy generated due to thermal mixing is negligible. This allows change in entropy to serve as a direct measure of turbine performance.

For steady non-uniform flow through a turbomachine, entropy can be mass-averaged at any axial location using Eqn. (8.1)

$$s^{ma} = \frac{\int s d\dot{m}}{\int d\dot{m}} = \frac{\int_{\mathcal{A}} s\rho V_x \, d\mathcal{A}}{\int_{\mathcal{A}} \rho V_x \, d\mathcal{A}} \tag{8.1}$$

The change in mass-averaged entropy, relative to a reference inlet plane, reflects the increase in loss. As discussed in [15], mass-averaging is appropriate in this context because entropy is a convected quantity. One can interpret this averaging procedure as a substitution of the original, non-uniform flow, with one that is uniform, but retains the same mass flux and entropy flux. Therefore, Eqn. (8.1) is simply a way of computing a specific quantity from the entropy flux and mass flux of the substitute flow.

The additional complexity of a time-dependent flow can be dealt with in the same manner. The objective is now to substitute an unsteady, non-uniform flow, with one

that is steady and uniform, but has the same mass flux and entropy flux over a given period of time, $\Delta t$. Computing the flux quantities now involves the additional step of averaging over time[2], resulting in Eqn. (8.2)

$$\dot{s}^{ma,ta} = \frac{\frac{1}{\Delta t}\int_{\Delta t}\int_{\mathcal{A}} s\rho V_x \; d\mathcal{A}dt}{\frac{1}{\Delta t}\int_{\Delta t}\int_{\mathcal{A}} \rho V_x \; d\mathcal{A}dt} \tag{8.2}$$

The order of integration is interchangeable, and practically it is more convenient to work with Eqn. (8.3)

$$\dot{s}^{ma,ta} = \frac{\int_{\mathcal{A}} \left(\frac{1}{\Delta t}\int_{\Delta t} s\rho V_x \; dt\right) d\mathcal{A}}{\int_{\mathcal{A}} \left(\frac{1}{\Delta t}\int_{\Delta t} \rho V_x \; dt\right) d\mathcal{A}} = \frac{\int_{\mathcal{A}} \left(s\rho V_x\right)^{ta} d\mathcal{A}}{\int_{\mathcal{A}} \left(\rho V_x\right)^{ta} d\mathcal{A}} \tag{8.3}$$

The preceding discussion provides a rational way for simultaneously accomplishing spacial and temporal averaging of enrtopy. It also emphasizes the general principle that the time-averaging step should always be applied directly to the quantity that is desired to be conserved (i.e. entropy and mass flux, rather than the individual flow variables). Therefore, with regard to volumetric entropy generation rate, the entire expression for $\dot{S}'''_{visc}$ should be time-averaged as a whole, rather than computing it from time-averaged velocity gradients.

### 8.1.2 Demonstration of mass/time-averaged entropy method for determining loss

Using mass/time-averaged entropy is a relatively straight forward way for keeping track of total losses. As mentioned, the approach can be used to account for turbine losses (viscous losses) whenever thermal mixing losses are negligible. One such situation is the expansion of a single mainstream flow. This section will use unsteady results from a turbine stage of a different design, obtained at the University of Bath[3], to illustrate the loss accounting procedure. The geometry for the University of Bath study is illustrated in Fig. 8-1. Note that the rotor is unloaded.

[2]Note that it is the mass flux and and entropy flux that are time averaged, not the individual flow variables $s, \rho, V_x$

[3]The research topic of that study was purge flow sealing effectiveness for different seal geometries

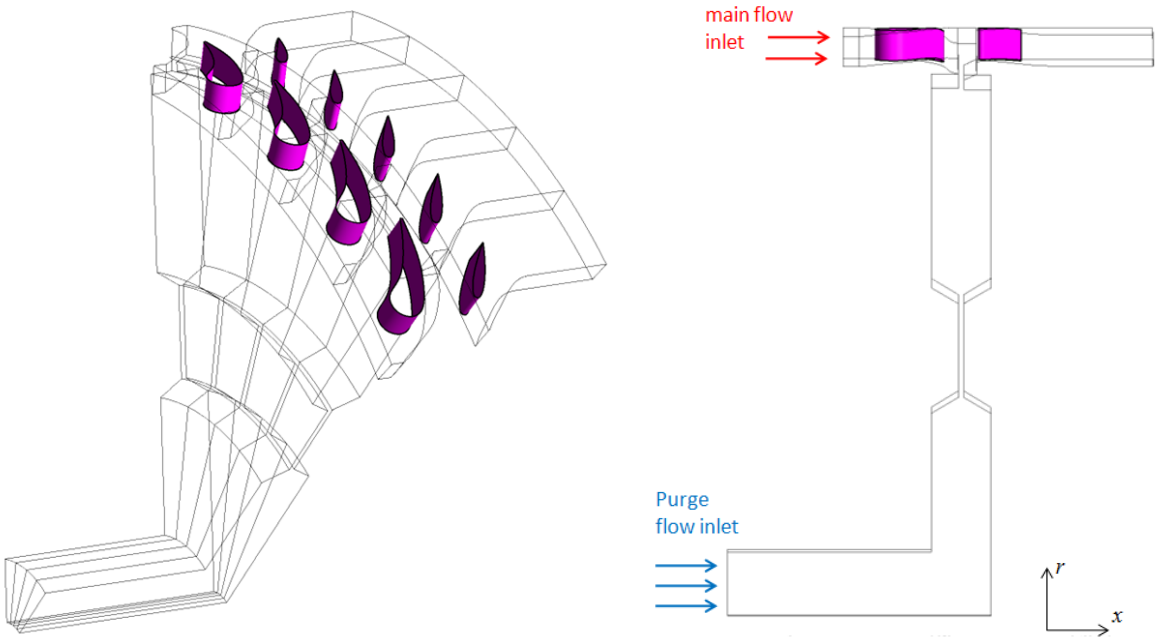


(a) Isometric view (b) Meridional view

Figure 8-1: GEOMETRY FOR UNSTEADY RESULTS FROM THE UNIVERSITY OF BATH.

Figure 8-2 presents accumulated loss curves for the stage, both from unsteady and steady calculations. The steady results are from a "frozen rotor" configuration (hence the subscript "frozen"), in which there is no mixing plane between the NGV and rotor domains, but the blades are kept at a constant relative position with respect to one another. The flow exiting the rotor is scaled by an expansion factor in order to accommodate the pitch change into the rotor, and avoid the need to model more than one blade passage.

Both total and viscous losses are shown for the frozen rotor configuration, where the viscous losses are isolated using the approach outlines in chapter 3. The two curves are indistinguishable, indicating that thermal mixing losses are negligible. Unsteady mass/time-averaged losses are obtained using Eqn. (8.3), and are also almost identical to the steady case. The reason for this is that the rotor is unloaded, and the NGV wake passes through without being distorted or effected in any significant way. This can be seen from the instantaneous entropy contours at midspan, shown in Fig. 8-3

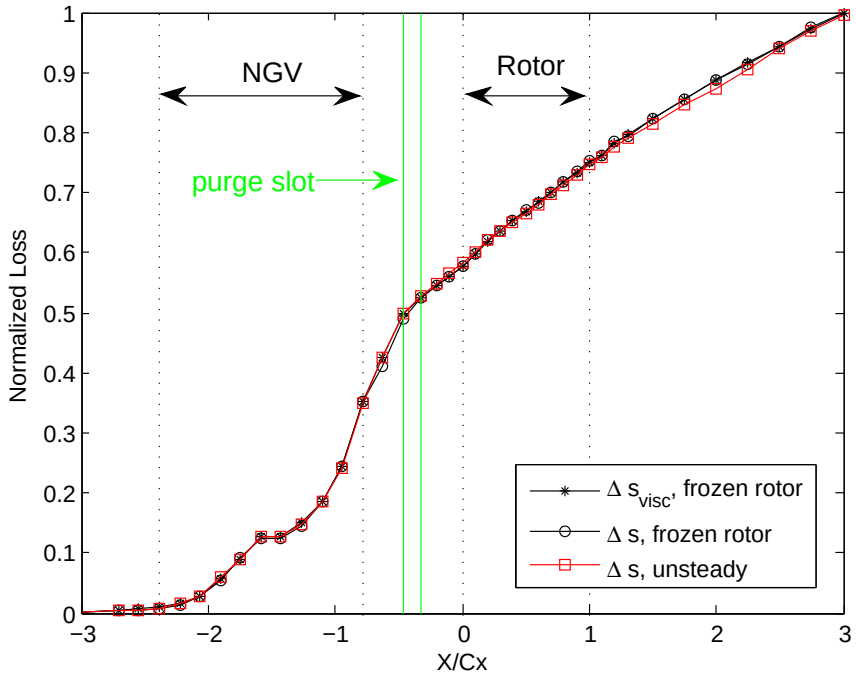


Figure 8-2: ACCUMULATED LOSS THROUGH UNIVERSITY OF BATH TURBINE STAGE WITH NO PURGE FLOW.

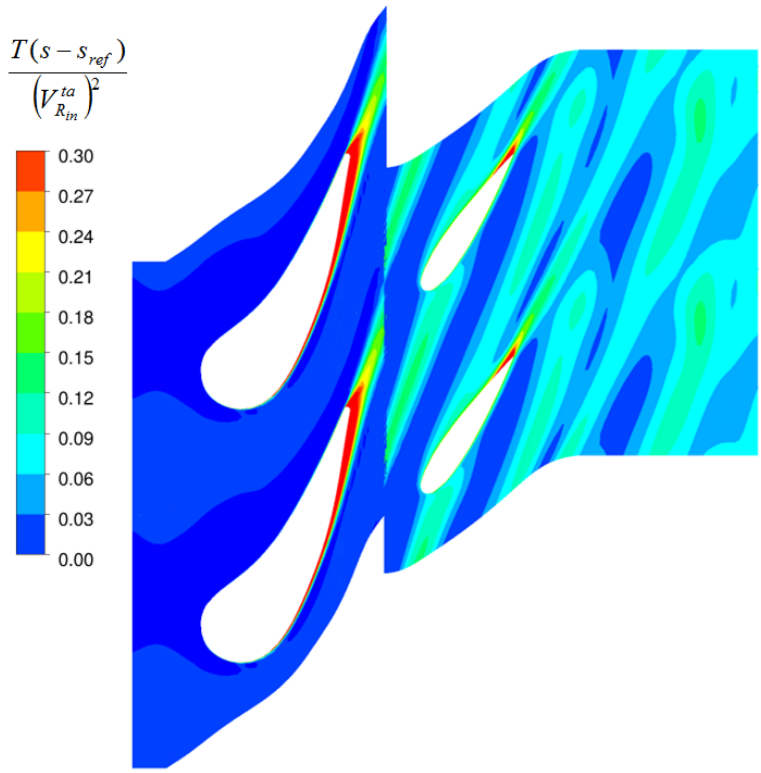


Figure 8-3: INSTANTANEOUS ENTROPY CONTOURS AT MIDSPAN.

### 8.1.3 Eliminating thermal mixing loss due to purge flow

When secondary air streams, such as purge flow, are introduced, there is likely to be a substantial amount of entropy generated due to thermal mixing. However, it is possible to design computations and experiments in such a way that thermal mixing losses are negligible, even in the presence of secondary air streams. This would allow for loss accounting with mass/time-averaged entropy to be applicable.

In review of the discussion in chapter 3, Fig. 8-4(a) shows that independently expanding two streams with distinct inlet conditions to the same downstream pressure will lead to a temperature difference between the two exit states. This constitutes a potential for doing work with a heat engine. Therefore, irreversible thermal mixing of the hot and cold streams leads to a lost opportunity to do work that is reflected in the total change in entropy, $\Delta s$. However, Fig. 8-4(b) shows that the potential for heat engine work can be eliminated if the two stream have the same inlet entropy. This would mean that any entropy generated in the expansion process will reflect only the lost opportunity to do expansion work, i.e. the viscous losses that are relevant to turbine performance. Because purge flow is injected at nearly identical static pressure as the mainstream flow, examination of the equation of state tells us that matching

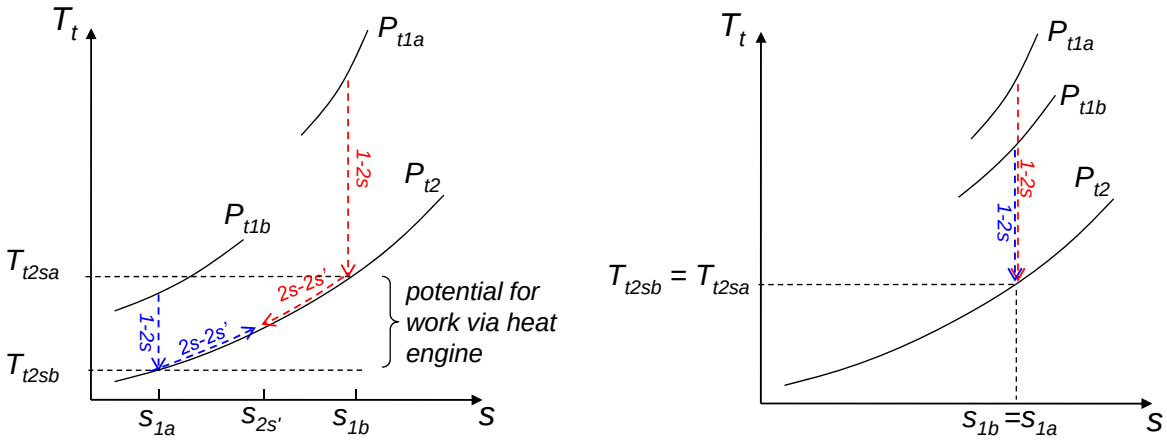


(a) Two streams have different inlet entropy (b) Two streams have identical inlet entropy

Figure 8-4: t-s DIAGRAM OF EXPANSION PROCESS OF TWO STREAMS

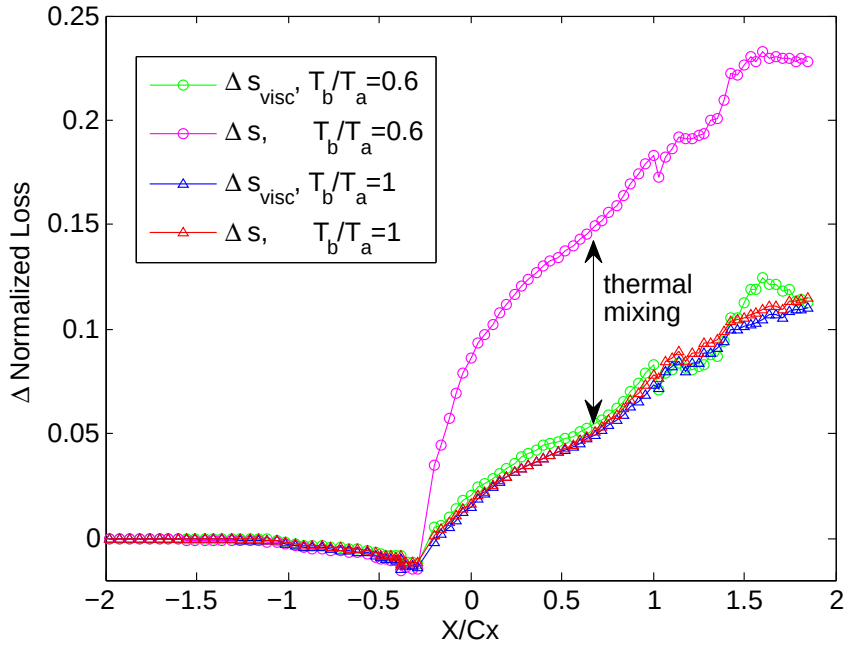


Figure 8-5: NET LOSS DUE TO PURGE FLOW INJECTION BASED ON $\Delta s$ AND $\Delta s_{visc}$. LOSS IS NORMALIZED BY BASELINE STAGE LOSS

the static temperature of the two streams is tantamount to matching their entropy.

$$s_a = s_b \tag{8.4a}$$

$$c_p ln\left(T_a\right) - \cancel{R ln\left(P_a\right)} = c_p ln\left(T_b\right) - \cancel{R ln\left(P_a\right)} \tag{8.4b}$$

To demonstrate that this temperature matching eliminates thermal mixing losses, we can compare results from steady computations (on the geometry in Fig. 2-1(b) of chapter 2) with and without a temperature difference between purge and mainstream flows. Figure 8-5 shows the lost work due to purge flow injection (i.e. losses above those in the baseline case with no purge flow) for two such cases. Lost work is calculated both based on the viscous loss accounting method of Eqn. (3.9), and based on total entropy generated. It is clear that the large thermal mixing loss, reflected in the difference between the curves based on $\Delta s$ and $\Delta s_{visc}$, is eliminated when the purge-mainstream temperature ratio is set to one[4].

[4]A small amount of entropy is still generated by thermal mixing due to the non-uniformity in the mainstream flow and due to the thermal boundary layer associated with viscous heating at the walls

### 8.1.4 Consequences of injecting purge flow at a temperature identical to the main flow temperature

Injecting purge flow at the mainstream static temperature does indeed eliminate any entropy generation due to thermal mixing, between purge and mainstream flows. However, it is important to realize that a higher purge flow temperature implies a proportionally lower purge flow density. Steady results, from computations on the geometry described in chapter 2 Fig. 2-1(b), will be used to illustrate the unintended consequences of lowering purge flow density. It will be shown that these consequences are of secondary importance, in the context of the purge flow losses we are interested in.

The first unintended consequence, of injecting purge flow at a higher temperature, and hence lower density, is higher purge flow meridional velocity. Figure 8-6(a) demonstrates that, for the same purge flow parameters $(mf, sf, gf, \phi)$, higher purge flow temperatures result in a 40% increase in mass-averaged axial and radial purge flow velocities at the exit of the purge slot. Fortunately, as it was established in chapter 5, the radial and axial components of purge flow velocity are relatively unimportant. They play a role in shear layer loss only, which was shown (by the mixed-out conrtol volume analysis in chapter 5) to scale with the square of the component-wise velocity deficit between purge and mainstream flow. Figure 8-6(a) shows that the velocity deficit in the circumferential direction, $\Delta V_\theta$, is significantly greater than that in the axial and radial directions. When these velocity deficits are squared, corresponding to the terms in the expression for mixed-out shear layer loss in Eqn. (5.1), Fig. 8-6(b) shows that the change in radial and axial velocity deficit will modify the shear layer loss by no more than 6% (which translates to 3% of purge flow losses).

The second unintentional consequence of higher purge flow density, is a change in the baroclinic torque experienced by non-uniform density fluid in a pressure gradient. Figure 8-7 illustrates an isosurface of 10% purge air mass fraction, showing clearly how purge air becomes entrained in the passage vortex. This is a phenomenon that has also been observed in [5][18][2][4]. Under realistic conditions, where purge flow

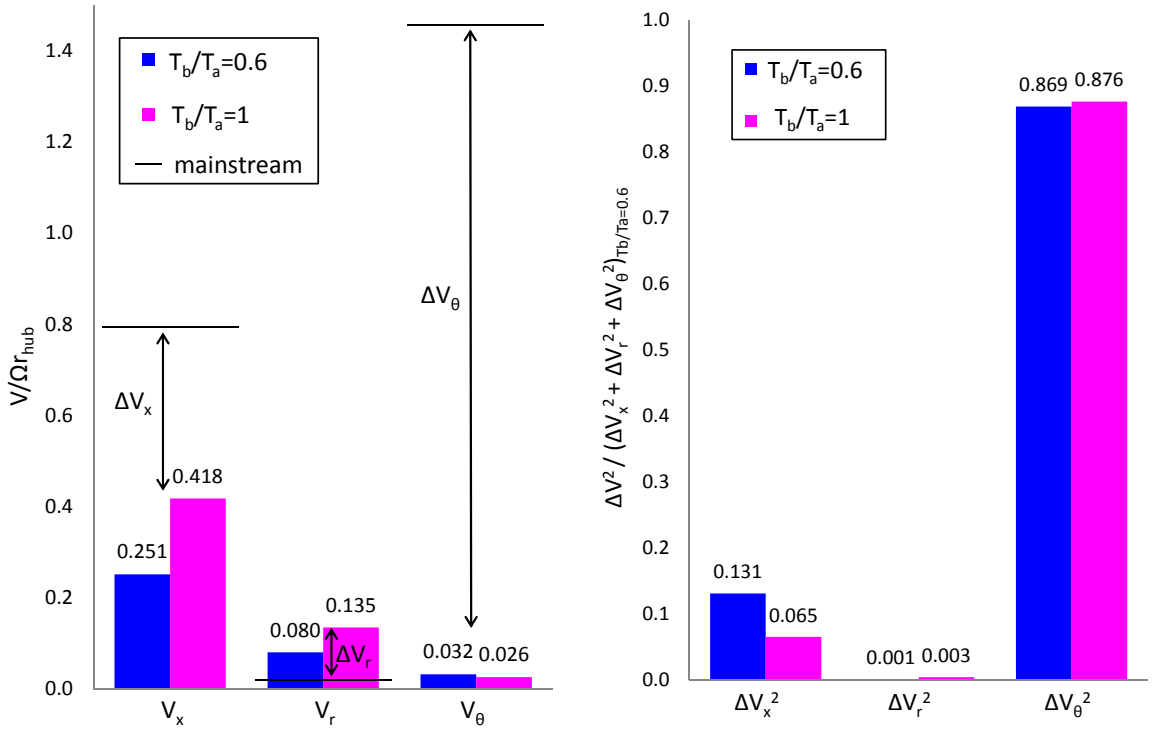


(a) Mass-averaged purge flow velocity components at hub radius, relative to mainstream velocity components

(b) Purge-mainstream velocity deficit squared

Figure 8-6: PURGE-MAINSTREAM AXIAL, RADIAL AND CIRCUMFERENTIAL VELOCITY DEFICITS, AND THEIR RELATIVE CONTRIBUTIONS TO SHEAR LAYER LOSS, FOR $\frac{T_b}{T_a} = 0.6$ AND $\frac{T_b}{T_a} = 1$.

temperatures are substantially lower than the mainstream, there is a density gradient pointing approximately towards the center of the passage vortex. This density gradient is normal to the streamwise pressure gradient, resulting in a baroclinic torque that generates vorticity. For an incompressible fluid with no body forces and viscous forces, taking the curl of the momentum equation results in an expression for the rate of change of vorticity[16] containing the term $\frac{1}{\rho^2}(\nabla\rho \times \nabla P)$

$$\frac{D\vec{\omega}}{Dt} = (\vec{\omega} \cdot \nabla)\,\vec{V} + \frac{1}{\rho^2}(\nabla\rho \times \nabla P) \tag{8.5}$$

Therefore, for the idealized vortex cross sections in Fig. 8-7, circumferential vorticity will be generated around the vortex, manifested as a slowing down of the vortex

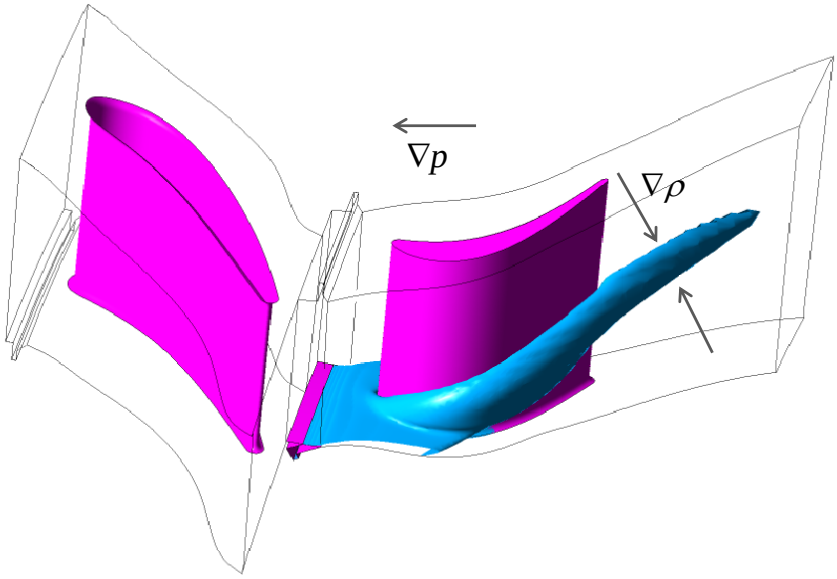


(a) Turbine stage with isosurface of 10% purge air mass fraction

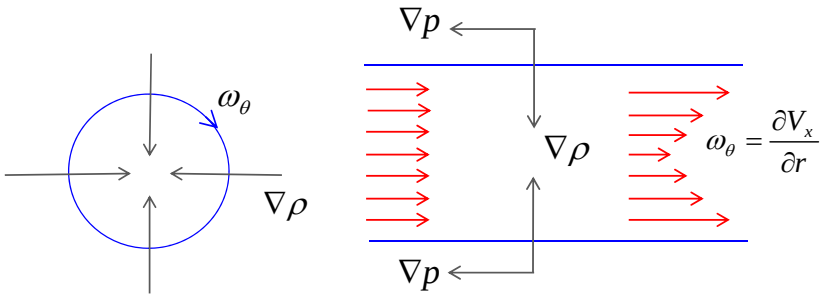


(b) Axial cut of idealized passage vortex

(c) Meridional cut of idealized passage vortex

Figure 8-7: SCHEMATIC OF DENSITY GRADIENT, PRESSURE GRADIENT AND RESULTING VORTICITY GENERATION DUE TO BAROCLINIC TORQUE.

core. This effect not only generates an axial but also a radial velocity gradient, as a consequence of of the blockage effect discussed in chapter 5. Both of these gradients contribute to viscous entropy generation. This phenomenon will not be present if the density gradient is eliminated, as in the case of purge flow injected at the mainstream static temperature. Therefore, there is the concern that eliminating this baroclinic torque will lead to a change in loss that is simply an artifact of injecting purge flow at an unrealistic temperature.

The sequence of events described are indeed observed when comparing the computed results for a case with and without temperature difference between purge and

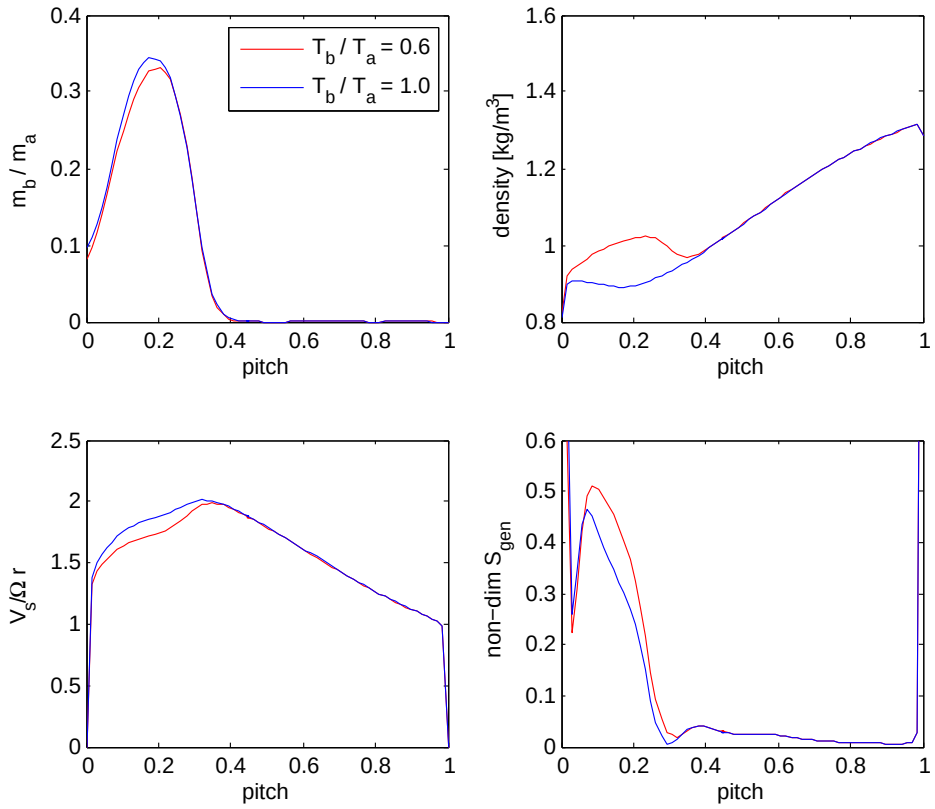


Figure 8-8: Blade-to-blade profiles of mass fraction, density, streamwise velocity and volumetric entropy generation rate, along a line of constant radius cutting through passage vortex core, on the axial plane $x/c_x = 0.8$

mainstream flows. Figure 8-8(a) shows the distribution of purge air from blade-to-blade, along a line of constant radius cutting through the passage vortex core, at an axial plane of $x/c_x = 0.8$. Figure 8-8(b) shows significantly lower density in the passage vortex core for the case of $T_b/T_a = 1$. As suggested by Eqn. (8.5), Fig. 8-8(c) shows increased streamwise velocity in the vortex core, and Fig. 8-8(d) shows a decrease in entropy generation rate. However, although the absence of baroclinic torque does modify the secondary flow loss, this effect is small. Figure 8-9 demonstrates that $\dot{S}'''_{visc}$ in the hub secondary flow region on the plane $x/c_x = 0.8$ is only slightly modified. Integrating $\dot{S}'''_{visc}$ over the area in the dashed bounding box results in less that 3% difference between the case with and without purge flow temperature difference.

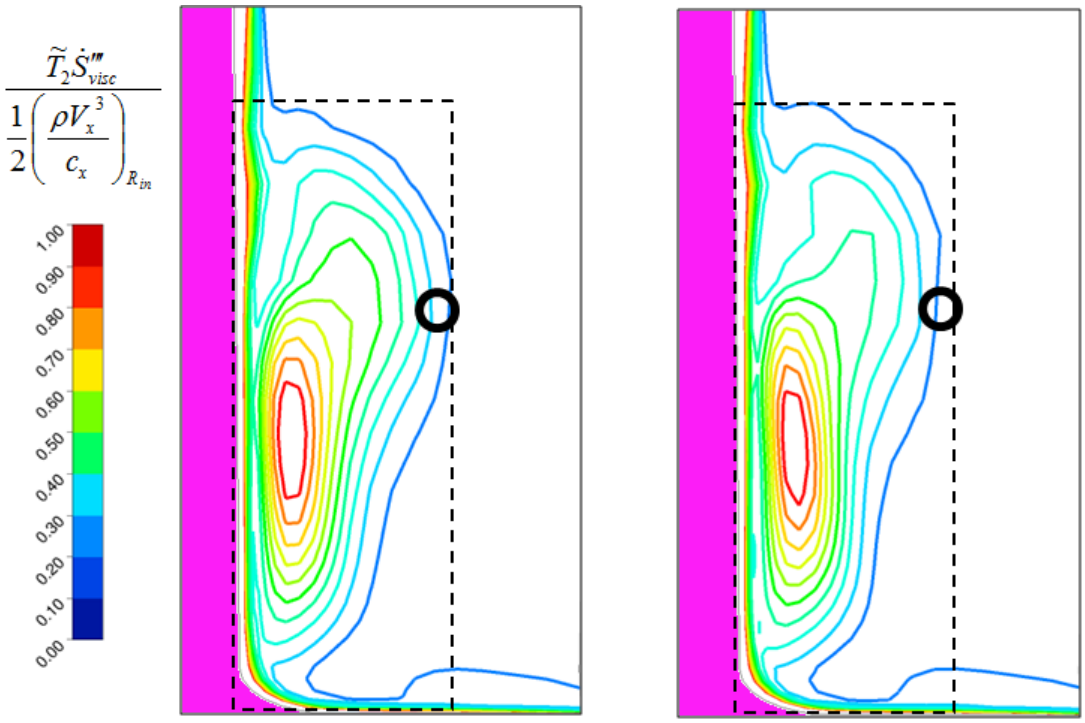


(a) $\frac{T_b}{T_a} = 0.6$ (b) $\frac{T_b}{T_a} = 1$

Figure 8-9: ENTROPY GENERATION RATE PER UNIT VOLUME IN REGION "B" OF FIG. 5-2(a) ON THE PLANE $x/c_x = 0.8$

### 8.1.5 Summary of first approach for determining loss in unsteady flow

It was shown that mass-averaging in unsteady flow situations involves an additional time-averaging step. The rationale behind mass/time-averaging of entropy is expressed in the substitution of a non-uniform unsteady flow with one that is uniform and steady, but has the same mass flux and entropy flux. It is crucial that the time-averaging step is applied directly to the quantities that are to be conserved in the substitution - in this case mass flux and entropy flux.

Change in mass/time-averaged entropy reflects both viscous and thermal mixing losses. If thermal mixing losses are negligible, this approach can be used as a measure of turbine performance. Situations in which thermal mixing losses can be neglected include single stream expansion processes, as well as multi-stream expansion precesses in which all streams have the same inlet entropy. The next section will develop another

approach for loss accounting in unsteady turbine flows. This second approach will provide a means for isolating viscous losses in unsteady flow situations, when thermal mixing losses can no longer be neglected.

## 8.2 Second Approach for Determining Loss in Unsteady Flow: Appropriate Averaging of Temperature and Pressure

In chapter 3 a method for isolating entropy generated by viscous effects, $\Delta s_{visc}$, was presented. The method relied on appropriate spacial averaging of flow quantities. By work-averaging stagnation pressure and mass-averaging stagnation temperature, it was possible to replace a non-uniform flow with an equivalent uniform flow that had the same potential for doing expansion work. The averaging procedure eliminated the potential for doing work with a heat engine, operating between hot and cold streams. Consequently, any thermal mixing losses were factored out, and the viscous losses relevant to turbine performance were isolated. This section will extend this approach to unsteady flow.

### 8.2.1 Appropriate averaging of temperature and pressure for unsteady flow

Consider an unsteady, non-uniform flow through an axial cross section of a turbine. Such a flow is characterized by stagnation quantities, $T_t$ and $P_t$, that are functions of space and time. This flow is expanded to an arbitrary downstream pressure, $P_{t2}$, and its power output is averaged over the time period, $\Delta t$. Given this unsteady, non-uniform flow, we seek an equivalent steady, uniform flow that conserves mass and energy, and produces the same amount of work over the interval $\Delta t$. The concept of such a substitution is an extension of Cumpsty and Horlock's[15] work-averaging method, with applications to unsteady flows.

As discussed in [15], because temperature is proportional to enthalpy - a convected quantity - in steady flow, non-uniform stagnation temperature is mass-averaged. In unsteady flow, the time-averaging step is applied in the same way as it was for entropy in the previous section, i.e.

$$T_t^{ma,ta} = \frac{\int_{\mathcal{A}} \left(T_t \rho V_x\right)^{ta} d\mathcal{A}}{\int_{\mathcal{A}} \left(\rho V_x\right)^{ta} d\mathcal{A}} \tag{8.6}$$

Note that that mass/time-averaging of stagnation temperature ensures that mass flux and enthalpy flux are conserved (Appendix D illustrates this in more detail).

To obtain a meaningful average of stagnation pressure, which to assign to the substitute uniform flow, we enforce the additional constraint on work output. It is desired that, when expanded to the same arbitrary downstream pressure, the substitute flow (which is steady and uniform) has the same power output as that of the unsteady flow, averaged over the time period $\Delta t$. Appendix D illustrates how this condition can be used to derive the expression for work/time-averaged stagnation pressure given in Eqn. (8.7)

$$P_t^{wa,ta} = \left[ \frac{\int_{\mathcal{A}} \left(T_t \rho V_x\right)^{ta} d\mathcal{A}}{\int_{\mathcal{A}} \left( T_t / P_t^{\frac{\gamma-1}{\gamma}} \rho V_x \right)^{ta} d\mathcal{A}} \right]^{\frac{\gamma}{\gamma-1}} \tag{8.7}$$

Mass/time-averaging of stagnation temperature and work/time-averaging of stagnation pressure can be performed at any axial cut through the turbine stage. This provides a meaningful average flow, which is steady and uniform, to which Eqn. (3.9) can be applied to yield viscous lost work.

### 8.2.2 A preliminary assessment of flow unsteadiness on purge flow-induced losses

Using this approach for isolating viscous losses, it is possible analyze the unsteady results from the University of Bath study that include purge flow. Figure 8-10 com-

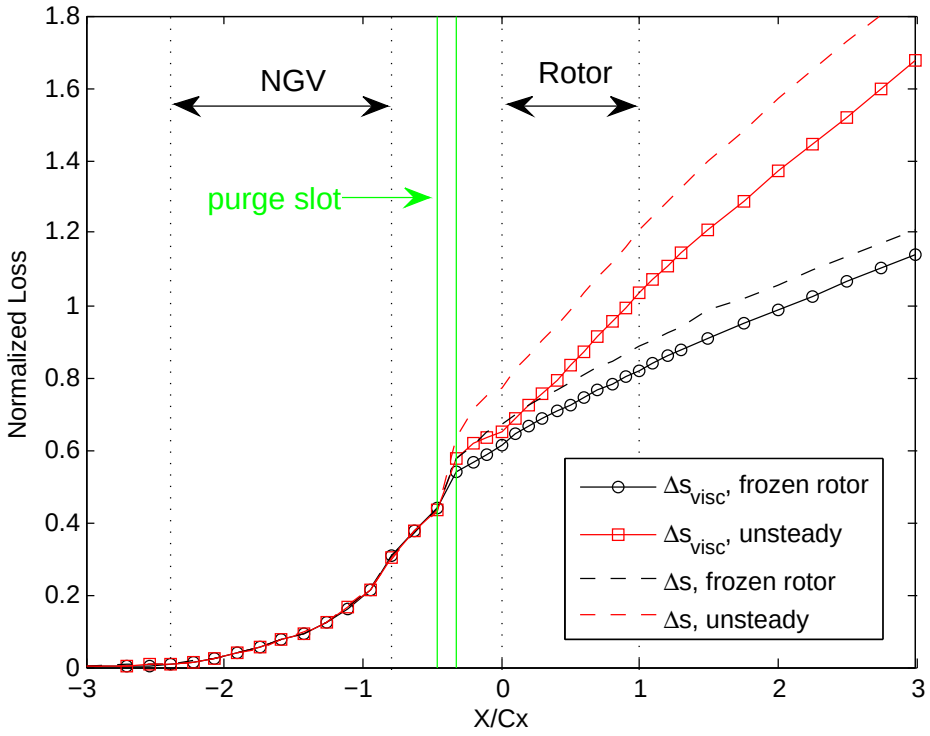


Figure 8-10: ACCUMULATED LOSS THROUGH UNIVERSITY OF BATH TURBINE STAGE, WITH 3% PURGE FLOW.

pares the viscous losses ($\Delta s_{visc}$) from frozen rotor and unsteady calculations. The total losses ($\Delta s$), based on mass/time-averaged entropy, are also plotted for reference.

It can be seen that, unlike the baseline case with no purge flow (Fig. 8-2), when purge flow is injected there is a substantial difference in the viscous loss generated downstream of the purge slot, between the steady and unsteady configurations. Loss accounting using mass/time-averaged entropy confirms this, though differences in thermal mixing losses add to the disparity in that situation[5]. Once again, it is emphasized that these results are only preliminary. A detailed study of the unsteady effects on purge flow losses is a necessary next step to this research topic.

[5]The reason for the different thermal mixing losses between frozen rotor and unsteady configurations is that purge flow was injected at a different temperature in each of the two cases

## 8.3 Summary of Unsteady Effects

This chapter was designed to provide guidelines for future work with unsteady results, with the aim of identifying the unsteady effects on purge flow loss. Two approaches to quantifying turbine losses, in the presence of unsteady NGV-rotor interaction, have been outlined. The first uses appropriate averaging of entropy. This approach is applicable in situations when thermal mixing losses are negligible. It was shown how computations involving secondary air streams can be design to satisfy this condition. The second approach builds upon the method for isolating viscous losses discussed in chapter 3. The concepts of mass-averaged stagnation temperature and work-averaged stagnation pressure are extended to unsteady flow. Both methods were applied to unsteady results from a previous study at the University of Bath. Although the geometry for this study differs substantially from the one used in the current project, preliminary results indicate that flow unsteadiness can have a large impact of the losses associated with purge flow injection. However, further work is needed to identify what these unsteady effects are.

# Chapter 9

# Conclusion

This chapter will review the objectives of the current work, as well as the approach taken to address these objectives. The key findings will be summarized, and suggestions for future work will be given.

## 9.1 Objectives and Approach

The goal of this research effort was to identify the characteristics of purge flow that are most detrimental to turbine performance, in order to provide design guidelines for improvements in efficiency. The effect of purge flow design on the system's ability to deter ingestion of hot mainstream gases, was taken into account in assessing the possible strategies for minimizing purge flow-induced losses. Relative to the existing body of literature on the subject, the current work focuses more on the traceability and causality of losses, producing generic findings with regard to purge flow loss mechanisms.

Technical aspects of the approach and tools used to accomplish the research objectives also constitute original contributions. In particular, multiple levels of modeling were used to systematically delineate between different loss mechanisms. A way for isolating viscous losses was developed, using appropriate averaging of flow quantities. Volumetric entropy generation rate was used, in conjunction with a rigorous definition of secondary flow, to relate loss generation to responsible flow features. To

the author's knowledge, the linear analysis, developed for identifying the conditions under which ingestion is likely to occur, is also new. Finally, a framework has been formulated for loss accounting in unsteady, non-uniform flow situations.

## 9.2 Key Findings

The key findings of this work include new insight into mechanisms for loss generation, and for ingestion of mainstream gases. These provide a basis for a design philosophy, as summarized below:

1. For purge flow injected at the hub, every 1% purge flow increases baseline stage losses by roughly 8%. This penatly is associated with three effects: a shear layer between purge and mainstream flows (which accounts for 1/2 of the penalty), interaction of purge flow with secondary flows through the blade passage, and an increased degree of reaction.

2. Purge flow injected from the shroud upstream of an unshrouded rotor introduces the beneficial effect of tip-clearance flow suppression. Consequently, shroud-injected purge flow does not result in significant losses.

3. Aside from the change in reaction, all of the above effects are driven by circumferential (swirl) velocity mismatch between purge and mainstream flows. Swirling purge flow prior to injection can potentially reduce losses of hub-injected purge flow by 2/3. Swirling shroud-injected purge flow does not result in significant benefit, as there is a tradeoff between purge flow losses and tip clearance flow suppression.

4. Gap width and injection angle are not effective design parameters for mitigating loss. Their combined effect can reduce purge flow losses by 5-6% only.

5. In the presence of a circumferential pressure non-uniformity associated with the rotor upstream influence, pre-swirling purge flow has the effect of reducing

sealing effectiveness. The increased requirement for purge flow essentially offsets the benefit of pre-swirling. However, a linear analysis of the phenomenon demonstrates that, if it is the stationary vane that dominates the pressure non-uniformity in the NGV-rotor gap, pre-swirling of purge flow is beneficial both with regard to loss and ingestion.

6. Preliminary results indicated that flow unsteadiness has a significant impact on the losses associated with purge-mainstream flow interaction.

A number of more general findings transcend the issue of purge flow. It was shown that regardless of whether purge flow is injected or not, blade-to-blade cross flow leads to high radial velocities generated on the blade suction surface. Specifically, it is the radial velocity gradient in the cross flow direction that is responsible for the majority of secondary flow losses. The role of the passage vortex is primarily to serve as a region of blockage, creating the conditions for high radial velocities to develop. This new insight has implications on a potential redesign of blade passages to suppress these radial flows.

It was also found that numerical evaluation of volumetric entropy generation rate is highly grid dependent. Away from well resolved endwall regions, direct evaluation of $\dot{S}'''_{gen}$ from velocity and temperature gradients is qualitatively correct, but underestimates entropy generation. Indirect evaluation of $\dot{S}'''_{gen}$, by means of Eqn. (3.15), also requires high grid resolutions. As a guideline, using wall functions with more than 12 nodal points in the boundary layer allows $\dot{S}'''_{gen}$ to capture wetted losses. To attain the same level of grid resolution in crucial regions of secondary flow will likely require an adaptive meshing strategy.

## 9.3 Future Work

Going forward, the first issue that needs to be addressed is the effect of flow unsteadiness on purge flow losses. The groundwork has already been laid in chapter 8. This final step, in the incremental modeling of purge flow interaction with main flow, will

assess the conclusions of this thesis under unsteady conditions. Preliminary results suggest that flow unsteadiness has a substantial impact of purge flow losses, and the specific mechanisms responsible need to be identified.

In chapter 7 it was noted that the pressure non-uniformity that drives ingestion is not entirely imposed by the external flow. The scaling of the pressure disturbance amplitude, and the associated upstream length scale, was observed but not explained. A rational explanation, for this coupling between purge flow and the pressure field, would be useful in improving our understanding of hot gas ingestion. Also, the ingestion criterion based on the unsteady linear analysis has yet to be assessed against CFD and/or experimental results.

One of the key conclusions of this work has been the effectiveness of purge flow swirl, in contrast to gap width and injection angle, as a means for reducing purge flow losses. Experimental assessment of this trend will be necessary.

Finally, the current work has identified generic purge flow loss mechanisms. The scaling of these mechanisms with respect to purge flow design parameters was established, but a parametric study of the effect of *stage* parameters on these mechanisms has yet to be undertaken.

# Appendix A

# Implementation of $\dot{S}'''_{gen\ indirect}$

Volumetric entropy generation rate can be calculated indirectly by applying Eqn. (3.15) on control volumes surrounding each nodal point (finite volumes). The concept is illustrated in two dimensions in Fig. A-1. Nodes at which data is stored define the vertices of elements. Elements are then discretized into sectors. by associating each sector with one vertex, a "finite volume" is created around each node, comprised of sectors from all the elements that node participates in. Surface integrals are discretized at integration points, located at the center of each surface segment within an element. Because the surface integrals are equal and opposite for control volumes adjacent to the integration points, the surface integrals are guaranteed to be locally

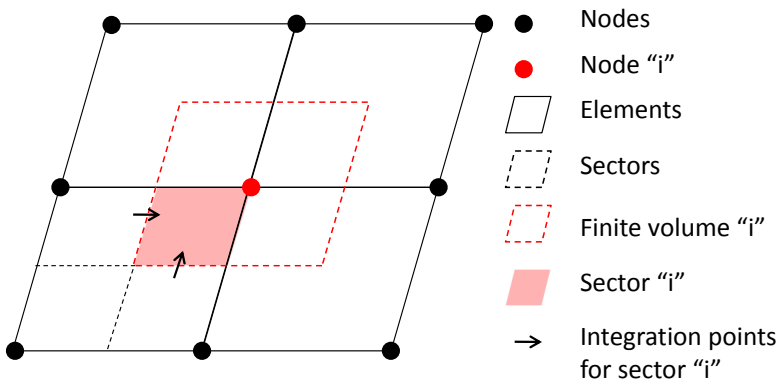


Figure A-1: CONSERVATION OF FLUX THOUGH FINITE VOLUME SURFACES IN 2 DIMENSIONS.

conservative (note that CFX solves equations for mass, momentum and energy, so only these quantities are strictly conserved).

For hexahedral elements in three dimensions, there are eight nodes (and hence eight sectors) and six faces per element. The numbering of these nodes and faces in the local (s,t,u) coordinates of a given element are presented in Fig. A-2.

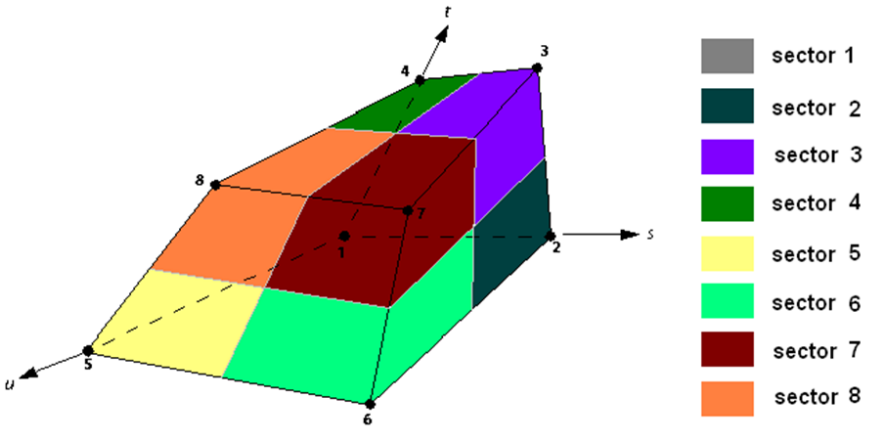


(a) Node and sector numbering

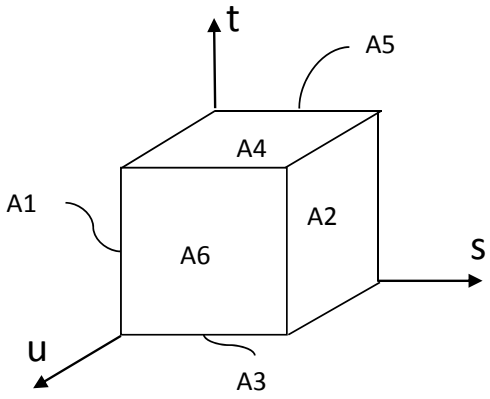


(b) Element and sector face numbering

Figure A-2: NODE, SECTOR AND FACE NUMBERING FOR HEXEHEDRAL ELEMENT.

Interpolation of solution variables from nodes to integration points is accomplished following the procedure of CFX. Finite-element shape functions describe the variation of a variable $\phi$ within an element as follows:

$$\phi = \sum_{i=1}^{n} N_i \phi_i \tag{A.1}$$

where $N_i$ is the shaper function for node $i$, and $\phi_i$ is the value of $\phi$ at node $i$. The tri-linear shape functions for a hexahedral element are given in Eqn (A.2)

$$N_1(s,t,u) = (1-s)(1-t)(1-u) \tag{A.2a}$$

$$N_2(s,t,u) = s(1-t)(1-u) \tag{A.2b}$$

$$N_3(s,t,u) = st(1-u) \tag{A.2c}$$

$$N_4(s,t,u) = (1-s)t(1-u) \tag{A.2d}$$

$$N_5(s,t,u) = (1-s)(1-t)u \tag{A.2e}$$

$$N_6(s,t,u) = s(1-t)u \tag{A.2f}$$

$$N_7(s,t,u) = stu \tag{A.2g}$$

$$N_8(s,t,u) = (1-s)tu \tag{A.2h}$$

Spatial derivatives, for the diffusion term in Eqn. (3.15), are also calculated at integration points following the standard finite element approach

$$\frac{\partial \phi}{\partial x} = \sum_{i=1}^{n} \frac{\partial N_i}{\partial x} \phi_i \tag{A.3}$$

where the Cartesian derivatives of the shape functions can be expressed in terms of their local derivatives via the Jacobian transformation matrix, as shown in Eqn. (A.4)

$$\begin{bmatrix} \frac{\partial N}{\partial x} \\ \frac{\partial N}{\partial y} \\ \frac{\partial N}{\partial z} \end{bmatrix} = \begin{bmatrix} \frac{\partial x}{\partial s} & \frac{\partial y}{\partial s} & \frac{\partial z}{\partial s} \\ \frac{\partial x}{\partial t} & \frac{\partial y}{\partial t} & \frac{\partial z}{\partial t} \\ \frac{\partial x}{\partial u} & \frac{\partial y}{\partial u} & \frac{\partial z}{\partial u} \end{bmatrix}^{-1} \begin{bmatrix} \frac{\partial N}{\partial s} \\ \frac{\partial N}{\partial t} \\ \frac{\partial N}{\partial u} \end{bmatrix} \tag{A.4}$$

Unfortunately, CFX does not document the functions used by developers to access raw solution data, and it was necessary to implement the routines for evaluating Eqn. (3.15) in Tecplot. An Add-On for Tecplot was written in C for this purpose. The high level structure of the code is summarized by the flow chart in Fig. A-3

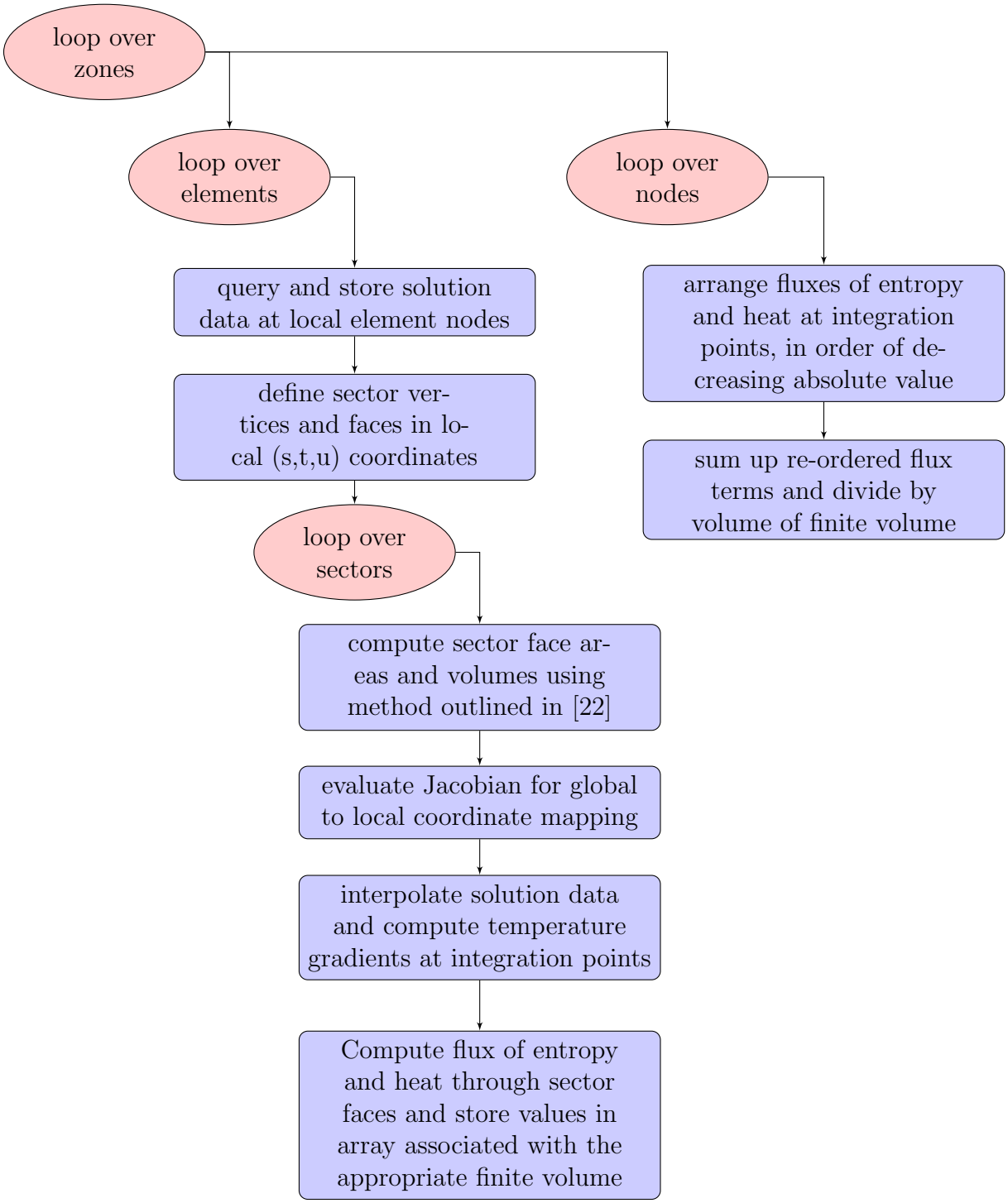


Figure A-3: FLOWCHART

# Appendix B

# Modifications to Young and Wilcock's Analysis

## B.1 Extension to Swirling Flow

In this appendix, Young and Wilcock's two dimensional control volume mixed-out analysis[10] is extended to an axisymmetric swirling flow configuration, result in Eqn. (5.1). We begin by writing the conservation equations for axial momentum, angular momentum and energy, for the control volume in Fig. 2-1(a),

$$\dot{m}_a \Delta V_{a,x} + \dot{m}_b \Delta V_{b,x} = -\frac{\dot{m}_a}{\rho V_{a,x}} \Delta P_a \tag{B.1}$$

$$\dot{m}_a \Delta V_{a,\theta} + \dot{m}_b \Delta V_{b,\theta} = 0 \tag{B.2}$$

$$\dot{m}_a \left( \Delta h_a + \frac{(V_a + \Delta V_a)^2}{2} - \frac{(V_a)^2}{2} \right) + \dot{m}_b \left( \Delta h_b + \frac{(V_b + \Delta V_b)^2}{2} - \frac{(V_b)^2}{2} \right) \tag{B.3}$$

The Second Law of Thermodynamics is

$$\Delta S = \dot{m}_a \Delta s_a + \dot{m}_b \Delta s_b \tag{B.4}$$

We assume that $\dot{m}_b \ll \dot{m}_a$, hence the bulk velocity, static temperature and pressure after the mixing, are not much different from $V_a$, $T_a$ and $P_a$. With this assumption, the following approximations can be made

$$\Delta V_b \approx V_a - V_b \tag{B.5}$$

$$\Delta V_{b,x} \approx V_{a,x} - V_{b,x} \tag{B.6}$$

$$\Delta V_{b,\theta} \approx V_{a,\theta} - V_{b,\theta} \tag{B.7}$$

$$\Delta V_a^2 \approx 0 \tag{B.8}$$

$$\Delta s_b \approx s_b(T_a, P_a) - s_b(T_b, P_b) \tag{B.9}$$

As in Young and Wilcock's analysis, we combine these equations (now including angular momentum) and make use of $T_a \Delta s_a = \Delta h_a - \Delta P_a/\rho_a$, resulting in an expression for the change in entropy (extensive) for the system

$$\begin{aligned} \Delta S =& \dot{m}_b \left[ s_b(T_a, P_a) - s_b(T_b, P_b) - \frac{h_b(T_a, P_a) - h_b(T_b, P_b)}{T_a} \right] \\ &+ \dot{m}_b \left[ \frac{(V_{x,a} - V_{x,b})^2 + (V_{r,a} - V_{r,b})^2 + (V_{\theta,a} - V_{\theta,b})^2}{2T_a} \right] \end{aligned} \tag{B.10}$$

By inspection, the first bracket in the Eqn. (B.10) is the lost work associated with heating up the secondary air stream to the mainstream static temperature without the use of a heat engine. The second term gives the dissipation of mechanical energy presented in Eqn. (5.1)

## B.2 Extension to Incomplete Mixing

For better agreement between the analytical model and CFD results, the mixed-out condition can be relaxed. One way to do this is to employ a mixing layer approximation, in which purge flow is divided into discrete layers, each layer mixing with a decreasing fraction of the mainstream, as illustrated in Fig. B-1(a). After the mixing of the top layer at constant area, the mixed-out velocity is used as the new mainstream

for the mixing of the subsequent layer.

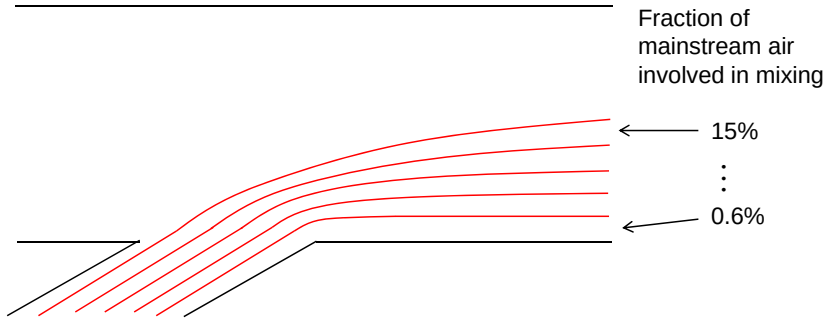


(a) Partial mixing model

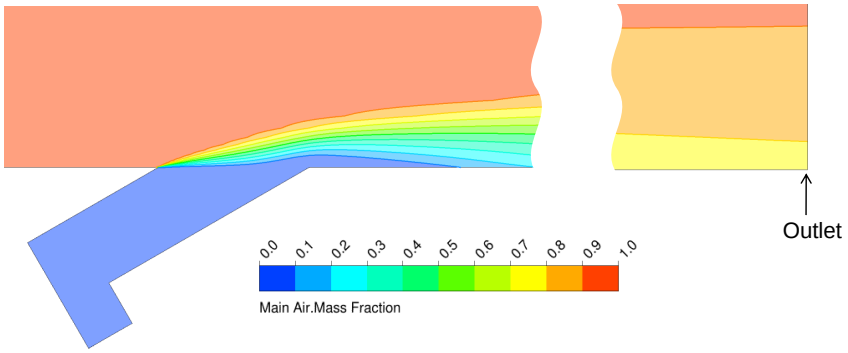


(b) Main air mass fraction

Figure B-1: MIXING LAYER APPROXIMATION FOR INCOMPLETE MIXING

This approach, and the specific fractions of mainstream air used for each mixing layer, were motivated by the CFD results of the axisymmetric case. For example, for a purge flow of $mf = 1.5\%$, it was found that that at the outlet of the axisymmetric configuration, 98% of the purge flow resides in the lower 15% span. Therfore, the top mixing layer mixes at most with 15% of the mainstream. Figure B-1(b) shows that at the exit of the domain, this fluid layer consists of about four times as much mainstream air as purge air. If we divide the purge flow into 10 equal mixing layers, for a total purge flow mass fraction of 1.5%, this leads to 0.6% of the mainstream gases participating in the final mixing layer (the one closest to the hub).

# Appendix C

# Evaluating $\dot{S}'''_{visc}$ in $(x, y, z)$ and $(s', c', r')$ Coordinates

## C.1 Expanding Tensor Notation for $\dot{S}'''_{visc}$

To write out the terms contributing to $\dot{S}'''_{visc}$, we must expand the tensor notation in Eqn. (3.11). We begin with the expression for the stress tensor, $\tau_{ij}$. This is given in Eqn. (C.1), where $e_{ij}$ is the shear rate tensor and $\delta_{ij}$ is the the Kronecker delta, or identity matrix.

$$\tau_{ij} = 2\mu_{eff} e_{ij} - \frac{2}{3}\mu_{eff}\left(\nabla \cdot \vec{V}\right)\delta_{ij} \tag{C.1}$$

The shear rate tensor written in Cartesian coordinates is

$$\begin{aligned} e_{ij} &= \frac{1}{2}\left(\frac{\partial V_i}{\partial x_j} + \frac{\partial V_j}{\partial x_i}\right) \\ &= \frac{1}{2}\begin{bmatrix} 2\frac{\partial V_x}{\partial x} & \left(\frac{\partial V_x}{\partial y} + \frac{\partial V_y}{\partial x}\right) & \left(\frac{\partial V_x}{\partial z} + \frac{\partial V_z}{\partial x}\right) \\ \left(\frac{\partial V_y}{\partial x} + \frac{\partial V_x}{\partial y}\right) & 2\frac{\partial V_y}{\partial y} & \left(\frac{\partial V_y}{\partial z} + \frac{\partial V_z}{\partial y}\right) \\ \left(\frac{\partial V_z}{\partial x} + \frac{\partial V_x}{\partial z}\right) & \left(\frac{\partial V_y}{\partial z} + \frac{\partial V_z}{\partial y}\right) & 2\frac{\partial V_z}{\partial z} \end{bmatrix} \end{aligned} \tag{C.2}$$

Plugging $\tau_{ij}$ into Eqn. (3.11) and simplifying yields Eqn. (C.3)

$$\begin{aligned}\dot{S}'''_{visc} =& \frac{1}{T}\tau_{ij}\frac{\partial V_i}{\partial x_j} \\ =& \frac{\mu_{eff}}{T}\left\{2\left[\left(\frac{\partial V_x}{\partial x}\right)^2+\left(\frac{\partial V_y}{\partial y}\right)^2+\left(\frac{\partial V_z}{\partial z}\right)^2\right]\right. \\ &+\left(\frac{\partial V_x}{\partial y}+\frac{\partial V_y}{\partial x}\right)^2+\left(\frac{\partial V_x}{\partial z}+\frac{\partial V_z}{\partial x}\right)^2+\left(\frac{\partial V_y}{\partial z}+\frac{\partial V_z}{\partial y}\right)^2 \\ &\left.-\frac{2}{3}\left(\frac{\partial V_x}{\partial x}+\frac{\partial V_y}{\partial y}+\frac{\partial V_z}{\partial z}\right)^2\right\}\end{aligned} \tag{C.3}$$

The last term in Eqn. (C.3) is identically zero for incompressible flow, and is often neglected. This term was confirmed to be negligible for all cases presented in this thesis. In the alternate Cartesian coordinate system, $(s', c', r')$, the expression for $\dot{S}'''_{visc}$ takes the form given in Eqn. (5.2)

## C.2 Velocity Gradients in $(s', c', r')$-Coordinates

Equation. (5.2) requires gradients of $V_{s'}$, $V_{c'}$ and $V_{r'}$ in the $s', c'$ and $r'$ directions. However, CFX outputs only velocity gradients in standard $(x, y, z)$ coordinates. To obtain the desired gradients, one can make use of the linear transformation defined by the rotation matrix $B$, which was also presented in Fig. 5-6(b).

$$B = \begin{bmatrix} cos\beta & -sin\beta & 0 \\ sin\beta & cos\beta & 0 \\ 0 & 0 & 1 \end{bmatrix} \tag{C.4}$$

where $\beta$ is the angle between the local streamwise direction and the axial. This transformation can be used to map any vector from $(x, y, z)$-space to $(s', c', r')$-space, including both velocity and gradients of velocity components. In Fig. 5-6(b) of chapter 5, this mapping was applied to velocity; here we express the transpose of that

result

$$\begin{bmatrix} V'_s & V'_c & V'_r \end{bmatrix} = \begin{bmatrix} V_x & V_y & V_z \end{bmatrix} B^T \tag{C.5}$$

The transformation can also be applied to the gradient operator

$$\begin{bmatrix} \frac{\partial}{\partial s'} \\ \frac{\partial}{\partial c'} \\ \frac{\partial}{\partial r'} \end{bmatrix} = B \begin{bmatrix} \frac{\partial}{\partial x} \\ \frac{\partial}{\partial y} \\ \frac{\partial}{\partial z} \end{bmatrix} \tag{C.6}$$

Combining Eqn. (C.5) and Eqn. (C.6) yields a relationship between the desired gradients of velocity in $(s', c', r')$-space and the available gradients of velocity in $(x, y, z)$-space

$$\begin{bmatrix} \frac{\partial V'_s}{\partial s'} & \frac{\partial V'_c}{\partial s'} & \frac{\partial V'_r}{\partial s'} \\ \frac{\partial V'_s}{\partial c'} & \frac{\partial V'_c}{\partial c'} & \frac{\partial V'_r}{\partial c'} \\ \frac{\partial V'_s}{\partial r'} & \frac{\partial V'_c}{\partial r'} & \frac{\partial V'_r}{\partial r'} \end{bmatrix} = B \begin{bmatrix} \frac{\partial V_x}{\partial x} & \frac{\partial V_y}{\partial x} & \frac{\partial V_z}{\partial x} \\ \frac{\partial V_x}{\partial y} & \frac{\partial V_y}{\partial y} & \frac{\partial V_z}{\partial y} \\ \frac{\partial V_x}{\partial z} & \frac{\partial V_y}{\partial z} & \frac{\partial V_z}{\partial z} \end{bmatrix} B^T \tag{C.7}$$

# Appendix D

# Averaging of Unsteady Non-uniform Flow in Turbomachines

Consider an unsteady, non-uniform flow through an axial plane. Such a flow is characterized by stagnation quantities, $Tt$ and $P_t$ that are functions of space and time. This flow is expanded to an arbitrary downstream pressure, $P_{t2}$, and its power output is averaged over the time period, $\Delta t$. Given this unsteady, non-uniform flow, we seek an equivalent steady, uniform flow that conserves mass and energy, and produces the same amount of work over the interval $\Delta t$. The concept of such a substitution is an extension of Cumpsty and Horlock's[15] averaging procedure to unsteady flow.

To begin, we obtain the mass flux of the substitute uniform flow, by time-averaging mass flux through a the axial plane, using Eqn. (D.1)

$$\dot{m}^{ta} = \frac{1}{\Delta t} \int_{\Delta t} \int_{\mathcal{A}} \rho V_x \; d\mathcal{A} dt \tag{D.1}$$

To obtain the stagnation temperature for the uniform flow, we make sure that the enthalpy flux, $\dot{H}$, is the same as that of the unsteady flow, averaged over the interval $\Delta t$. As discussed in [15], because temperature is proportional to enthalpy - a convected quantity - in steady flow, non-uniform stagnation temperature is mass-

averaged. For unsteady flow, Eqn. (D.2) uses the same thought process to simultaneously accomplish mass and time-averaging.

$$\dot{T}^{ma,ta} = \frac{\dot{H}^{ta}}{c_p \dot{m}^{ta}} = \frac{1}{\dot{m}^{ta}} \frac{1}{\Delta t} \int_{\Delta t} \int_{\mathcal{A}} T_t \rho V_x \; d\mathcal{A} dt \tag{D.2}$$

To fix the state of the substitute flow, we can obtain an appropriate average for stagnation pressure, by following the derivation for work-averaged pressure in steady flow[15] as a guideline. The flow at at each time instant can be expanded to the some uniform downstream pressure, which would result in instantaneous power output amounting to $\dot{W} = \dot{H}_{t2} - \dot{H}_t$. Using the isentropic flow relation, given in Eqn. (3.1) of chapter 3, and time-averaging over the instantaneous power values, results in Eqn. (D.3)

$$\begin{aligned} \dot{W}^{ta} &= \frac{1}{\Delta t} \int_{\Delta t} \left( \dot{H}_{t2} - \dot{H}_t \right) dt \\ &= \frac{1}{\Delta t} \int_{\Delta t} \int_{\mathcal{A}} c_p T_t \left[ \left( \frac{P_{t2}}{P_t} \right)^{\frac{\gamma}{\gamma - 1}} - 1 \right] \rho V_x \; d\mathcal{A} dt \end{aligned} \tag{D.3}$$

The time-averaged power can also be expressed in terms of the equivalent steady, uniform flow that we seek as a substitute. Using the expressions for $\dot{m}^{ta}$ and $\dot{T}^{ma,ta}$ already derived, we arrive at Eqn. (D.4)

$$\begin{aligned} \dot{W}^{ta} &= \dot{m}^{ta} c_p T_t^{ma,ta} \left[ \left( \frac{P_{t2}}{P_t^{wa,ta}} \right)^{\frac{\gamma}{\gamma - 1}} - 1 \right] \\ &= c_p \frac{1}{\Delta t} \int_{\Delta t} \int_{\mathcal{A}} T_t \rho V_x \; d\mathcal{A} dt \; \left[ \left( \frac{P_{t2}}{P_t^{wa,ta}} \right)^{\frac{\gamma}{\gamma - 1}} - 1 \right] \end{aligned} \tag{D.4}$$

Equating the two expressions for $\dot{W}^{ta}$, given in Eqn. (D.3) and Eqn. (D.4), ensures that the power output of the substitute steady, uniform flow, is equivalent to that of the unsteady, non-uniform flow, on a time-averaged basis. Some brief algebra results an expression for the only unknown, $P_t^{wa,ta}$, which is given in Eqn. (D.5)

$$P_t^{wa,ta} = \left[ \frac{\int_{\Delta t}\int_{\mathcal{A}} T_t \rho V_x \; d\mathcal{A}dt}{\int_{\Delta t}\int_{\mathcal{A}} T_t / P_t^{\frac{\gamma-1}{\gamma}} \rho V_x \; d\mathcal{A}dt} \right]^{\frac{\gamma}{\gamma-1}} \tag{D.5}$$

Note that the order in which the integrations are done is interchangeable. Depending on the post-processing software used, it may be convenient to do the time-averaging step first, as in Eqn. D.6

$$\begin{aligned} P_t^{wa,ta} &= \left[ \frac{\int_{\mathcal{A}} \frac{\int_{\Delta t} T_t \rho V_x \; dt}{\Delta t} d\mathcal{A}}{\int_{\mathcal{A}} \frac{\int_{\Delta t} T_t / P_t^{\frac{\gamma-1}{\gamma}} \rho V_x \; dt}{\Delta t} d\mathcal{A}} \right]^{\frac{\gamma}{\gamma-1}} \\ &= \left[ \frac{\int_{\mathcal{A}} \left(T_t \rho V_x\right)^{ta} d\mathcal{A}}{\int_{\mathcal{A}} \left( T_t / P_t^{\frac{\gamma-1}{\gamma}} \rho V_x \right)^{ta} d\mathcal{A}} \right]^{\frac{\gamma}{\gamma-1}} \end{aligned} \tag{D.6}$$

# Bibliography


[1] Kevin Reid, John Denton, Graham Pullan, Eric Curtis, and John Longley. The effect of stator-rotor hub sealing flow on the mainstream aerodynamics of a turbine. In *2006 ASME 51st Turbo Expo, May 6, 2006 - May 11*, volume 6 PART A, pages 789–798, Barcelona, Spain, 2006. American Society of Mechanical Engineers.

[2] M. Pau, G. Paniagua, D. Delhaye, la Loma de, and P. Ginibre. Aerothermal impact of stator-rim purge flow and rotor-platform film cooling on a transonic turbine stage. *ASME Journal of Turbomachinery*, 132(2):021006 (12 pp.), 04 2010.

[3] F. Kost and M. Nicklas. Film-cooled turbine endwall in a transonic flow field: Part i - aerodynamic measurements. *ASME Journal of Turbomachinery*, 123(4):709–719, 2001.

[4] Jonathan H. P. Ong, Robert J. Miller, and Sumiu Uchida. The effect of coolant injection on the endwall flow of a high pressure turbine. In *2006 ASME Turbo Expo*, volume 6, pages 915–924, GT2006–91060, Barcelona, Spain, 2006. American Society of Mechanical Engineers.

[5] I. Popovi and H. P. Hodson. Aerothermal impact of the interaction between hub leakage and mainstream flows in highly-loaded hp turbine blades. *Proceedings of ASME Turbo Expo 2010: Power for Land, Sea and Air*, June 14-18, 2010 2010.

[6] E. de la Rosa Blanco, H. P. Hodson, and R. Vazquez. Effect of the leakage flows and the upstream platform geometry on the endwall flows of a turbine cascade. In *2006 ASME 51st Turbo Expo, May 6, 2006 - May 11*, volume 6 PART A, pages 733–744, Barcelona, Spain, 2006. American Society of Mechanical Engineers.

[7] S. E. Vlasic, J. P Lavoie, and S. H. Moustapha. The effect of secondary air injection on the performance of a transonic turbine stage. In *Proceedings of the ASME TURBO EXPO 2002: Turbomachinery, June 3, 2002 - June 6*, volume 5 A, pages 147–157, Amsterdam, Netherlands, 2002. American Society of Mechanical Engineers.

[8] C. McLean, C. Camci, and B. Glezer. Mainstream aerodynamic effects due to wheelspace coolant injection in a high-pressure turbine stage: Part i - aerody-

namic measurements in the stationary frame. *ASME Journal of Turbomachinery*, 123(4):687–696, 2001.

[9] U. P. Phadke and J. M. Owen. Aerodynamic aspects of the sealing of gas-turbine rotor-stator systems: Part 1: The behavior of simple shrouded rotating-disk systems in a quiescent environment. *International Journal of Heat and Fluid Flow*, 9(2):98–105, 6 1988.

[10] J. B. Young and R. C. Wilcock. Modeling the air-cooled gas turbine: Part 2-coolant flows and losses. *ASME Journal of Turbomachinery*, 124(2):214–221, 2002.

[11] Arthur J. Glassman. *Turbine design and application, edited by Arthur J. Glassman.* Scientific and Technical Information Office, National Aeronautics and and Space Administration: [For sale by the Supt. of Docs., U.S. Govt. Print. Off.] Washington,, 1972.

[12] J. B. Young and J. H. Horlock. Defining the efficiency of a cooled turbine. *Transactions of the ASME.The Journal of Turbomachinery*, 128(4):658–67, 10 2006.

[13] J. H. Horlock. The basic thermodynamics of turbine cooling. *ASME Journal of Turbomachinery*, 123(3):583–592, 2001.

[14] J. B. Young and R. C. Wilcock. Modeling the air-cooled gas turbine: Part 1-general thermodynamics. *ASME Journal of Turbomachinery*, 124(2):207–213, 2002.

[15] N. A. Cumpsty and J. H. Horlock. Averaging nonuniform flow for a purpose. *ASME Journal of Turbomachinery*, 128(1):120–129, 2006.

[16] E. M. Greitzer, C. S. Tan, and M. B. Graf. *Internal Flow.* Cambridge University Press., New York, NY, 2004.

[17] J. D. Denton. Loss mechanisms in turbomachines. *Journal of Turbomachinery*, 115(4):621–656, 1993.

[18] G. Paniagua, R. Denos, and S. Almeida. Effect of the hub endwall cavity flow on the flow-field of a transonic high-pressure turbine. *ASME Journal of Turbomachinery*, 126(4):578–586, 2004.

[19] P. Schuler, W. Kurz, K. Dullenkopf, and H. J. Bauer. The influence of different rim seal geometries on hot-gas ingestion and total pressure loss in a low-pressure turbine. *Proceedings of ASME Turbo Expo 2010: Power for Land, Sea and Air*, June 14-18, 2010, 2010.

[20] O. P. Sharma and T. L. Butler. Predictions of endwall losses and secondary flows in axial flow turbine cascades. *ASME Journal of Turbomachinery*, 109(2):229–236, 1987.

[21] Hai-Ping Wang, Steven J. Olson, Richard J. Goldstein, and Ernst R. G. Eckert. Flow visualization in a linear turbine cascade of high performance turbine blades. In *Proceedings of the International Gas Turbine and Aeroengine Congress and Exposition, June 5, 1995 - June 8*, pages 11–11pp. ASME, 1995.

[22] D. E. Davies and D. J. Salmond. Calculation of the volume of a general hexahedron for flow predictions. *AIAA Journal*, 23:954–956, 1985.